6-1-2007

Modeling and design of high force RFMEMS contact switches

Joseph Zekry

The American University in Cairo

Modeling and Design of High Force RFMEMS Contact Switches

by

Joseph Eid Estafanous Zekry

A Thesis Submitted to Department of Physics

May 2007

in partial fulfillment of the requirements for

The degree of Master of Science

has been approved by

Dr. Amr Shaarawi
Thesis Committee Chair / Adviser _____
Affiliation: The American University in Cairo

Dr. Harrie Tilmans
External Adviser _____
Affiliation: IMEC, Belgium

Dr. Hosny Omar
Thesis Committee Reader / Examiner _____
Affiliation: The American University in Cairo

Dr. Hani Ragai
Thesis Committee Reader / Examiner _____
Affiliation: Ain Shams University

Dr. Sherif Sedky
Thesis Committee Reader / Examiner _____
Affiliation: The American University in Cairo

H. Omar 30/5/07 _____ _____

Department Chair Date Dean Date

Program Director

The American University in Cairo

SCHOOL OF SCIENCES AND ENGINEERING

MODELING AND DESIGN OF HIGH FORCE RFMEMS CONTACT SWITCHES

A Thesis Submitted to

Department of Physics

in partial fulfillment of the requirements for

THE DEGREE OF MASTER OF SCIENCE

BY

JOSEPH EID ESTAFANOUS ZEKRY

BACHELOR OF SCIENCE 2005, ELECTRICAL ENGINEERING

(Under the Supervision of Professor Amr M. Shaarawi)

MAY 2007

Modeling and Design of High Force RFMEMS Contact Switches

by

Joseph Eid Estafanous Zekry

A THESIS SUBMITTED TO DEPARTMENT OF PHYSICS

May 2007

ABSTRACT

This thesis describes the modeling and design issues of high force electrostatically actuated RFMEMS contact switches. Various reliability issues and challenges are associated with the design of RFMEMS contact switches. The reliability of microcontacts is of major importance in increasing the lifetime of such devices. A semi-analytical model based on the beam deflection theory is developed to calculate the contact force delivered by parallel-plate electrostatically actuated switch structures. The model is capable of fast and accurate static solution for complicated switch structures which are normally analyzed using finite element analysis techniques. High force designs are presented together with finite element simulations confirming the model results and reflecting on the reliability of these switch structures. The RF performance is expected to be comparable to recently announced commercial counterpart specifications. A simple all-metal surface micromachining technology providing thick electroplated nickel beams will be used to implement high force switch structures.

ACKNOWLEDGEMENTS

This work has been technically and financially supported by the Physics Department (AUC, Egypt), the Yousef Jameel Science and Technology Research Center, STRC, (AUC, Egypt), and IMEC vzw (Belgium). The AUC Physics Department granted me the Laboratory Instructor Graduate Fellowship during fall ‘05, spring ‘06 and fall ‘06 including tuition for my M.Sc. program and financial support. The STRC granted me technical and financial support for four semesters starting fall ‘05 within a research project to experimentally investigate Rh as contact metal for RFMEMS switches. The STRC also provided my M.Sc. tuition during spring ‘07. IMEC supported the Design of High Force RFMEMS Contact Switch project with AUC through Research Grant SC06 during fall ‘06 and spring ‘07. IMEC also provided me with all necessary financial and technical support during my two visits, for 10 weeks each, to their facilities in Belgium during summer ‘06 and winter ’07.

I am much thankful for the help and encouragement of my family, my professors, and all my friends and colleagues in Egypt and Belgium. I thank Dr. Amr Shaarawi (AUC) for supervising my work at AUC during fall ’06 and spring ’07. I thank Dr. Moustafa Ghannam (Kuwait University) for supervising my work at AUC during fall ’05 and spring ’06 and for facilitating my later collaboration with IMEC. I thank Dr. Harrie Tilmans (IMEC) for supervising my work at IMEC during winter ’07. I thank Philippe Soussan (IMEC) for supervising my work at IMEC during summer ’06.

I thank my project partner, Phillip Ekkels (RFMEMS group, IMEC), for his helpful feedback on my work and for the useful discussions we had about the design and the fabrication technology for this work. I thank Dr. Sherif Sedky (AUC) for training me to use the PLD system at STRC. I thank Ahmed Nagy (AUC) for taking the SEM

photos for many of my samples. I thank Xavier Rottenberg (Analog and RF group, IMEC) for his advice on the RF design issues, and Stanislaw Kalicinski (Reliability group, IMEC) for training me on the contact force/resistance setup at IMEC. I thank Noha Farghal for providing me with her paper on PLD of AuNi and her useful comments. Finally, many thanks to the members of my thesis committee for their efforts to enhance the quality of this work.

This thesis is dedicated to my parents and my two sisters.

LIST OF ABBREVIATIONS

1D	One dimension(al)
2D	Two dimensions/dimensional
3D	Three dimensions/dimensional
AUC	American University in Cairo (Egypt)
BC	Boundary condition(s)
CMOS	Complementary metal-oxide-semiconductor (technology)
CPW	Coplanar waveguide
DC	Direct current
FET	Field effect transistor
IMEC	Inter-university Microelectronics Center (Belgium)
MEMS	Micro-electro-mechanical systems
ODE	Ordinary differential equation
PC	Personal computer
PLD	Pulsed Laser deposition
RF	Radio frequency
RFMEMS	Radio frequency micro-electro-mechanical systems
SEM	Scanning electron microscope/micrograph
STRC	Science and Technology Research Center (at AUC, Egypt)
WTC	Wicht Technologie Consulting (Germany)

TABLE OF CONTENTS

1. INTRODUCTION p.1

1.1. RFMEMS SWITCHES p.1

1.1.1. A Commercial Apprehension p.2

1.1.2. Types of RFMEMS Switches p.3

1.1.3. Actuation Techniques p.3

1.2. HIGH FORCE RFMEMS CONTACT SWITCH ACHIEVEMENTS p.4

1.3. ORGANIZATION OF THIS WORK p.6

2. RELIABILITY AND DESIGN CHALLENGES OF RFMEMS CONTACT SWITCHES p.11

2.1 RELIABILITY OF MICROCONTACTS p.11

2.1.1. Contact Materials p.12

2.1.2. Rhodium as a Contact Material p.14

2.2. AIR GAP BREAKDOWN p.16

2.3. MECHANICAL STABILITY p.17

2.4. PACKAGING p.19

3. SEMI-ANALYTICAL MODEL FOR ELECTROSTATICALLY ACTUATED BEAMS p.28

3.1. SIMPLIFIED ANALYTICAL MODEL p.29

3.2. A 2.5D SEMI-ANALYTICAL MODEL p.31

3.2.1. Before Pull-in p.32

3.2.2. After First Pull-in p.35

3.2.3. After Second Pull-in p.37

3.3. APPLYING THE SEMI-ANALYTICAL MODEL TO BRIDGE PROBLEMS p.40

4. DESIGN AND TECHNOLOGY OF HIGH FORCE RFMEMS CONTACT SWITCHES p.64

4.1. DESIGN CONSIDERATIONS p.64

4.2. COVENTORWARE SIMULATIONS p.68

4.2.1. Contact Switch Simulation Procedure p.68

4.2.2. High Force Contact Switch Structures p.70

4.2.3. Stress Gradient Deflections p.71

4.2.4. Mechanical Resonant Frequency p.71

4.3. RF PERFORMANCE p.72

4.4. TECHNOLOGY CHARACTERIZATION p.74

4.4.1. Technology Features p.74

4.4.2. Characterization Test Structures p.75

4.5. SAMPLE DEVICE DESIGNS p.77

5. CONCLUSIONS AND FUTURE WORK p.94

5.1. CONCLUSIONS p.94

5.2. FUTURE WORK p.95

REFERENCES p.98

FIGURES

1.1	RFMEMS market 2004-2009 [6]	p.8
1.2	Omron high contact force switch [1]	p.8
1.3	Radant MEMS switch [5]	p.9
1.4	TeraVicta high force disk actuator [18]	p.9
2.1	SEMs of sample gold contact surfaces after failure [19]	p.20
2.2	Lifetime for different contact materials combinations [19]	p.20
2.3	Contact characteristics of Au, AuNi and Rh [23]	p.21
2.4	Schematic diagram of the PLD setup at AUC	p.21
2.5	SEM of two different rhodium thin film samples	p.22
2.6	Test structures for Rh contact characterization	p.23
2.7	Electrical setup and current flow for resistance measurement	p.23
2.8	Measuring the resistive contribution of the top sample	p.24
2.9	Measuring the resistive contribution of the bottom sample	p.24
2.10	Contact resistance versus contact force for Rh-Au interface	p.25
2.11	Contact resistance versus contact force for Rh-Pt interface	p.25
2.12	Modified Paschen curve [27]	p.26
2.13	Release holes	p.26
3.1	Structure of fixed-fixed flexures contact switch	p.44
3.2	Pull-in of electrostatic actuators	p.45
3.3	Cantilever beam structure for the semi-analytical model	p.45
3.4	Free body diagram of the cantilever beam before pull-in	p.46
3.5	Bending moment calculation diagrams for a cantilever before pull-in and after first pull-in	p.46
3.6	CoventorWare and the semi-analytical model results for sample structure number (2) at 10V	p.47

3.7	Flowcharts of the main program and the subroutine for solving a cantilever problem before pull-in	p.48
3.8	Pull-in detected for sample structure number (2) at 30V	p.49
3.9	Free body diagram of the cantilever beam after first pull-in	p.49
3.10	CoventorWare and the semi-analytical model results for sample structure number (2) at 30V	p.50
3.11	Flowchart to implement the model solution after first pull-in	p.51
3.12	Initial deflection curve for the cantilever beam model after first pull-in	p.52
3.13	Second pull-in of sample structure number (2) observed at 70V	p.52
3.14	Maximum contact force of 0.328mN obtained for sample structure number (3) at 34V	p.53
3.15	Modified sample structure number (3)	p.54
3.16	The modified cantilever structure with stopper	p.54
3.17	Free body diagram of cantilever beam after second pull-in	p.55
3.18	Bending moment calculation diagrams for a cantilever after second pull-in	p.55
3.19	Model and CoventorWare results for sample structure number (3) at 40V	p.56
3.20	A flowchart to implement the semi-analytical model solution after second pull-in	p.58
3.21	Free body diagrams for the bridge problem	p.59
3.22	Free body diagram of cantilever beam after second pull-in	p.60
4.1	Contact force for different stopper bump heights/positions	p.79
4.2	Effect of the passive section length and width on the contact force	p.80
4.3	Effect of the spring stiffness on the contact force	p.81
4.4	Effect of the beam material elasticity on the contact force	p.81
4.5	A 3D CoventorWare model for a cantilever switch with folded springs	p.82

4.6	Meshed 3D model for cantilever switch with folded springs	p.82
4.7	Deflected beam shape after simulation	p.83
4.8	Folded-spring bridge-type switch	p.83
4.9	Introducing stress gradients to folded-spring bridge switch	p.84
4.10	HFSS parametric 3D model for bridge switches	p.85
4.11	HFSS model reconfigured for small area device	p.85
4.12	Modeling On and Off states in HFSS	p.86
4.13	Simulated isolation and insertion loss for high force bridge	p.86
4.14	HFSS model for a cantilever inline series switch	p.87
4.15	Simulated isolation and insertion loss for inline switch	p.88
4.16	RFMEMS contact switch technology cross-section	p.89
4.17	Layout of contact resistance/force characterization structure	p.89
4.18	2/4μm air gap breakdown detection structure	p.90
4.19	1μm air gap breakdown detection structure	p.90
4.20	Design tree	p.91
4.21	A high force bridge design	p.91
4.22	A low force cantilever design	p.92
4.23	Sample cantilever switch layout	p.92
5.1	A proposed all-metal capacitive switch structure	p.97

TABLES

1.1	Performance comparison of different actuation techniques [1]	p.10
1.2	RFMEMS contact switches reported worldwide by the industry before September 2002 [1]	p.10
2.1	Comparing the properties of rhodium, platinum and gold [30]	p.27
2.2	Experimental results in the literature on the electrostatic breakdown field of small air gaps [27, 29, 31]	p.27
3.1	Parameters of sample structure number (1)	p.61
3.2	Parameters of sample structure number (2)	p.61
3.3	Parameters of sample structure number (3)	p.62
3.4	Comparing the semi-analytical model results to CoventorWare results for sample structure number (3) at 40V	p.62
3.5	Comparing the 3 modeling techniques for the bridge version of sample structure number (3)	p.63
4.1	Comparing the RF performance of the high force bridge with the TeraVicta commercial switch measurements	p.93

CHAPTER 1

INTRODUCTION

1.1. RFMEMS SWITCHES

RFMEMS switches are revolutionary miniature devices fabricated using special MEMS technologies, and employed to switch RF signals. RFMEMS switches present substantial performance challenges to their mature counterparts: conventional electromagnetic relays and solid state transistors.

An RFMEMS switch is superior to a conventional electromagnetic relay in terms of power consumption, switching speed, device size, and frequency band of operation. An electrostatically actuated RFMEMS switch theoretically consumes zero power as no steady state current is allowed to flow in the actuator. It operates with switching time in the range of 1-200μs [1]. Comparing these values to more than 0.2W power consumption and 6ms switching time for a modern high frequency relay [2], the significant differences become unambiguous. The miniature size and technology compatibility of these MEMS devices open the possibility for on-chip integration with other integrated RF systems and CMOS circuits. The only limitation on RFMEMS devices compared to conventional relays is the amount of RF signal power that can be reliably handled by a single device.

Compared to semiconductor devices, like FETs, RFMEMS switches provide much higher signal isolation in the Off state and much higher conduction in the On state, as well as excellent linearity and wider frequency-band of operation [3, 4]. However, solid state devices are typically much smaller in size and exhibit much less switching delay [1].

A wide range of applications can make use of RFMEMS switches, including: transmit/receive switching in mobile phones and base stations, reconfigurable RF systems such as filters, phase shifters and antennas, as well as automated RF testing and data acquisition systems [5].

1.1.1. A Commercial Apprehension

The worldwide market value of RFMEMS components in 2004 was $126 million and is forecasted to grow to $1.1 billion in 2009 as shown in Fig. (1.1) [6]. The chart in Fig. (1.1) illustrates the actual RFMEMS market turnover in 2004, and the forecast for the following 5 years, as reported by Wicht Technologie Consulting, Germany, in December 2005. The RFMEMS market in 2004 was mainly stimulated by bulk acoustic wave filters used for mobile phones, with very little contribution from the other major RFMEMS components like RFMEMS switches and tunable capacitors which, according to the same report, still had problems with reliability, packaging, and CMOS integration [6]. This reveals that until 2005, RFMEMS switches have been locked in university labs and very small scale commercial products, despite their early introduction by K. Petersen at IBM in a neat report in 1979 [7].

On the other hand, the revolution in wireless communication systems capabilities in the past few years is creating a heavy demand for the commercialization of these devices [8]. The predicted substantial growth of RFMEMS components market for consumer electronics, base stations and RF automated test equipment, as shown in Fig. (1.1), emphasizes this breakthrough in the commercialization of RFMEMS switches during the present few years.

1.1.2. Types of RFMEMS Switches

RFMEMS switches include two major types of devices: capacitive switches and contact switches. A capacitive switch makes use of the fact that a large capacitance represents very small impedance at very high frequencies. The device conducts high frequency RF signals when it is actuated to a high capacitance state, and isolates the same signal when released to another low capacitance state. The advantage of such devices is that they encounter no direct contact between two metallic surfaces, with the price of losing their functionality at DC and low frequencies. On the other hand, a contact switch is capable of conducting DC signals and a wide band of RF signals. A contact switch involves a direct ohmic contact between two metallic surfaces. This feature represents a major reliability challenge for such devices and is the main motivation to present this work.

Contact devices can be subdivided into two categories: microrelays and switches. A microrelay provides full electrical isolation between the DC control circuit and the controlled RF signal. On the other hand, a switch configuration normally involves one or more common points between the control and RF circuits. An intermediate device is presented within this work which provides full isolation only in the Off state, but a common electrical point is established between the DC control circuit and the RF signal in the On state. This intermediate device can be called a semi-relay. Such semi-relay can be easily upgraded to a full microrelay as will be illustrated in the last chapter of this work.

1.1.3. Actuation Techniques

Four main actuation techniques can be used to provide the mechanical motion required for an RFMEMS switch operation; these are electrostatic, electrothermal,

piezoelectric and electromagnetic actuation [9]. A performance comparison among these four actuation techniques is given in Table (1.1).

Piezoelectric and electromagnetic actuation techniques basically require complicated fabrication technologies and provide a low contact force. For these reasons, they are not widely used to implement RFMEMS switches. Electrothermal actuation provides very high contact force, with two major drawbacks of consuming much power and exhibiting long switching delays. The remaining and most widely used actuation technique for RFMEMS switches is electrostatic actuation. Electrostatic actuation offers the least possible power consumption, least complicated technology, least switching delay, a wide range of contact forces, and best die area utilization [1].

The main purpose of this thesis is to provide a design methodology to maximize the contact force that can be achieved by the simple parallel-plate electrostatic actuation technique.

1.2. HIGH FORCE RFMEMS CONTACT SWITCH ACHIEVEMENTS

Table (1.2) summarizes the performance of all substantially reported RFMEMS contact switches developed by the industrial sector before September 2002 [1]. Only two of the devices in this table provide a high contact force above 0.2mN. The many low force devices reported to date by industrial and academic organizations are not discussed in detail here to maintain the focus on high contact force devices, with the exception of the Radant MEMS switch because of its relatively high lifetime and successful commercial profile.

The first high force switch is the Cronos Integrated Microsystems (USA) switch which is based on a lateral high force, high power consumption, electrothermal

actuator [1]. Despite the obtained high contact force, this approach is not very interesting because of the drawbacks of electrothermal actuation.

The second high force device is the Omron (Japan) switch. This device is interesting as it provides high contact force and still uses electrostatic actuation. The reason is using a very large-area actuator of 1.6x1.6mm^2. The actuator membrane is made of 18-24μm thick silicon layer, suspended 3μm above the fixed electrode. The achieved high contact force makes it a very reliable switch, despite its large size and relatively low frequency operation [1]. The structure of the Omron switch is shown in Fig. (1.2).

One popular RFMEMS contact switch is the Radant MEMS (USA) electrostatically actuated switch. Its commercial success is stimulated by its high reported lifetime [5]. The device is based on a cantilever beam made of 7-9μm thick gold. The device occupies a small area of 30x75μm^2, and produces a low contact force of 100μN resulting in a high contact resistance of 2-3Ω [1]. The small area of the device allows reducing the contact resistance by using two or more switches in parallel. The structure of the Radant switch is shown in Fig. (1.3).

In 2003, E. Thielicke et al. from Berlin University of Technology reported a high force electrostatically actuated switch producing 0.5mN contact force. The device area is 700x700μm^2. It is based on a polysilicon membrane, fabricated using a 16-masks process. The contact resistance is low, but the device lifetime is degraded because of using pure gold as contact material [10]. Another report in 2003 described a relatively mature technology from wiSpry Inc. (USA), but low contact force was reported [11].

In 2004, several low voltage electrostatically actuated switches were reported, but most of them produced low contact forces below 0.3mN per contact [12-14].

In 2005, a very high contact force design was reported by J. Qiu et al., reaching 4mN using a lateral bistable electrothermally actuated silicon structure [15]. During the same year, more interest in low voltage electrostatically actuated switches could be observed [16].

Recently in 2006, the structure of the commercially available contact switch from TeraVicta (USA) was reported. The device is based on a high force electrostatically actuated disk as shown in Fig. (1.4). This device is the next major commercially available RFMEMS switch after the Radant switch with a long lifetime reaching one billion switching cycles [17]. The high contact force provides a low contact resistance, which is opposite to the case of the Radant switch. The device is actuated at 68V, and exhibits a switching time of 70μs. The switch RF performance is acceptable up to 7GHz which is a higher band compared to the high force Omron switch discussed earlier [18].

1.3. ORGANIZATION OF THIS WORK

The next chapter of this thesis discusses the basic design and reliability challenges of RFMEMS contact switches, with emphasis on the major reliability issue which is the metal-to-metal direct contact. Different options for the contact material are introduced. An experimental investigation of the potential of rhodium as a contact material is described. Other challenges including air gap breakdown, mechanical stability and packaging are also discussed.

In Chapter 3, a relatively fast and accurate semi-analytical model for electrostatically actuated beams is developed. In the beginning, a simplified analytical model for the problem is presented for the sake of problem illustration and for later comparison with the results of the advanced model. And then, the semi-analytical model is developed

based on the basic differential equation for beam deflections. The free body diagrams for the switch structure in different situations are presented, and the final arrangements of the beam deflection equation are concluded. Numerical solution algorithms are also introduced to illustrate the method of solving the obtained nonlinear beam deflection differential equations. The model is later modified to handle bridge-type structures in addition to the originally handled cantilever-type structures. Comparisons between the semi-analytical model results and 3D finite element simulations are provided in each step of the model development to validate the accuracy of the model.

In Chapter 4, the design considerations for high force RFMEMS contact switch structures are discussed based on the basic characteristics of parallel-plate electrostatic actuators, in addition to the results of the semi-analytical model developed in Chapter 3. Subsequently, the procedure used to simulate RFMEMS contact switch static behavior using CoventorWare^{TM} is discussed. CoventorWare 3D finite element simulation results for high force devices are presented, together with a discussion on the simulation results for the mechanical stability and the effect of stress gradients. Furthermore, the RF performance of the achieved designs is presented with a comparison to recently reported performance characteristics of commercially available devices. The fabrication technology proposed to implement the presented designs is described, together with test structures designed to measure the technology-dependent performance parameters. Sample RFMEMS contact switch designs are later presented for implementation using the proposed technology.

Finally, the last chapter of this thesis summarizes the major achieved results and presents a vision for the future work expected to be performed based on the results of this work.

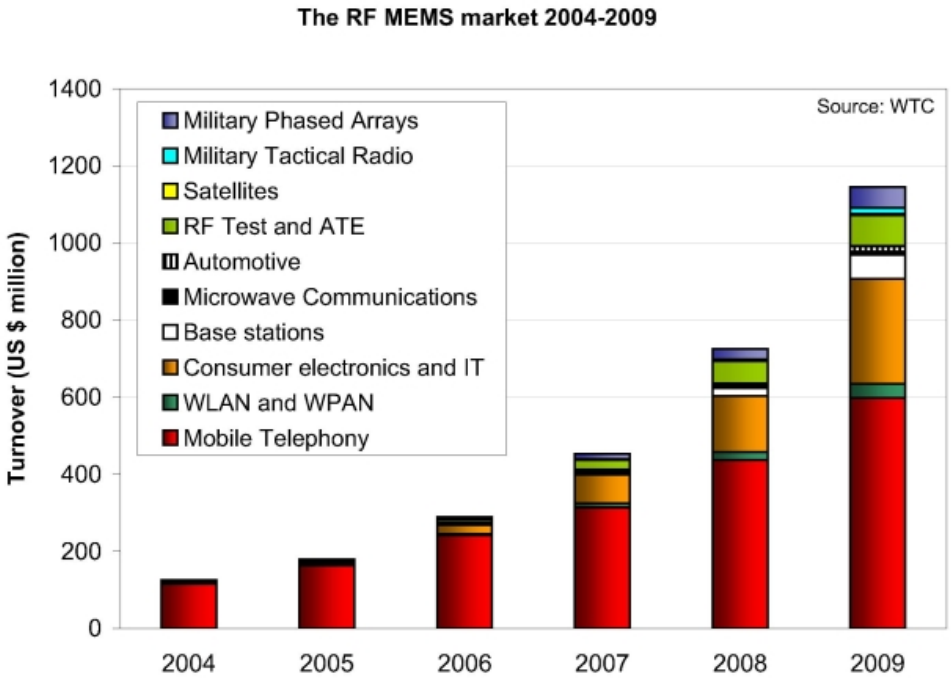

Figure 1.1. Actual turnover of RFMEMS market in 2004 and forecasts until 2009, as reported by Wicht Technologie Consulting in December 2005 (after [6]).

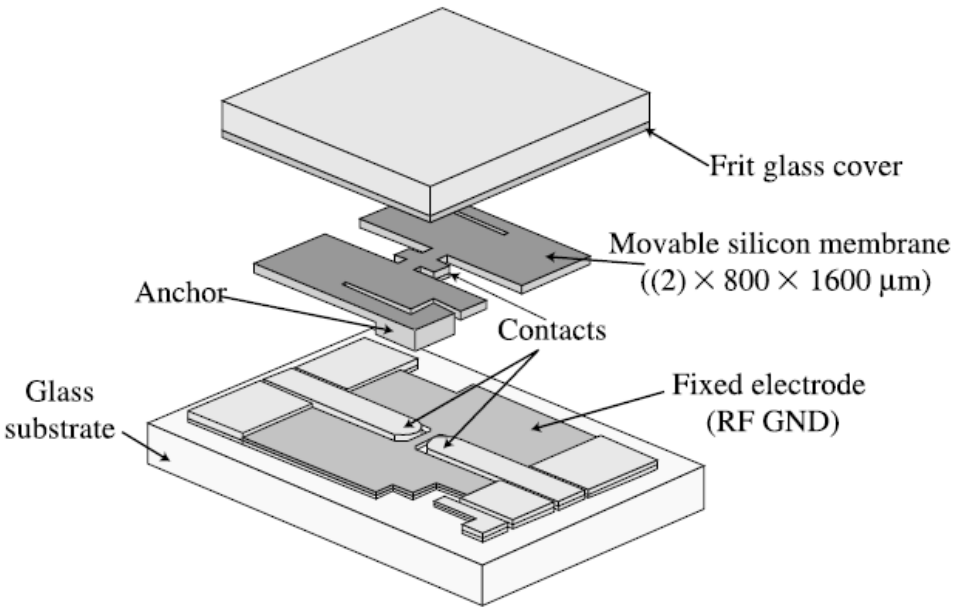

Figure 1.2. The Omron high contact force switch (after [1], Copyright IEEE).

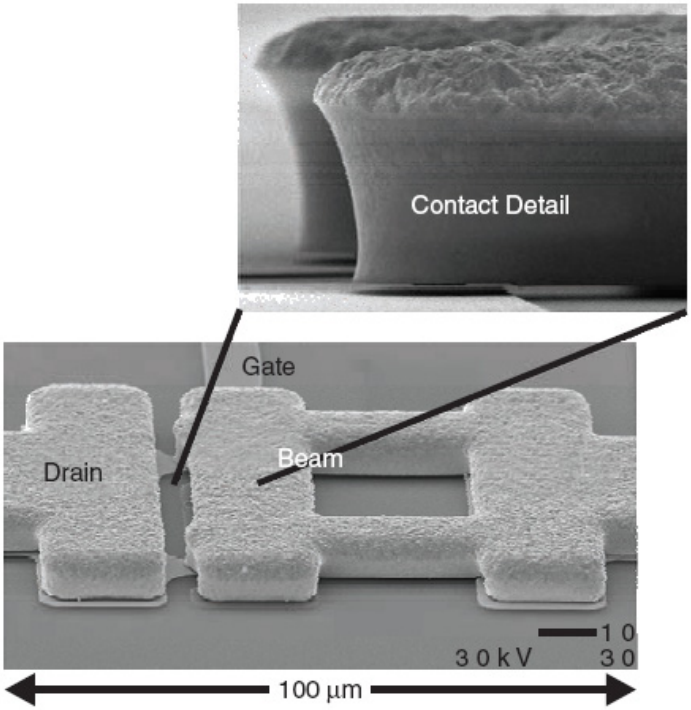

Figure 1.3. The Radant MEMS switch (after [5]).

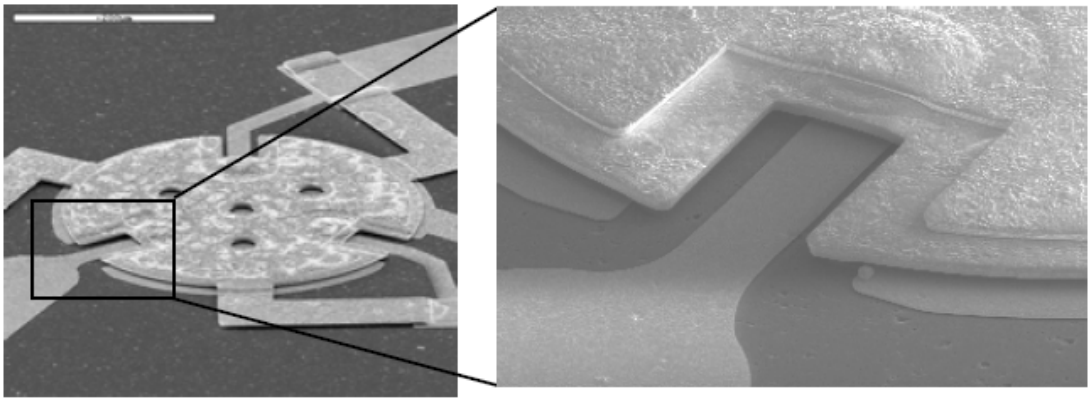

Figure 1.4. The TeraVicta high force disk actuator (after [18]).

Actuation technique	Power consumed (mW)	Size	Switching time (μs)	Contact force (μN)
Electrostatic	0	Small	1-200	50-1000
Electrothermal	<200	Large	300-10,000	500-4000
Piezoelectric	0	Medium	50-500	50-200
Electromagnetic	<100	Medium	300-1000	50-200

Table 1.1. Overall performance comparison of the different RFMEMS switch actuation techniques [1].

Company	Actuation	Power (mW)	Switching time (μs)	Contact force (μN)
Cronos	Electrothermal	200	10,000	2000-3000
Omron	Electrostatic	0	300	1000
Motorola	Electrostatic	0	4-6	100
Radant	Electrostatic	0	3-6	100
Microlab	Electromagnetic	0	500	50-150
Rockwell Sci.	Electrostatic	0	8-10	50-100
Samsung	Electrostatic	0	100	50-100
HRL	Electrostatic	0	30-40	50-100
Lincoln Labs	Electrostatic	0	<1	50-100
ST-Microelectronics	Electrostatic /thermal	0	300	50-100
NEC	Electrostatic	0	30-40	50-100

Table 1.2. Comparing the performance of RFMEMS contact switches reported worldwide by the industry before September 2002 [1].

CHAPTER 2

RELIABILITY AND DESIGN CHALLENGES OF RFMEMS CONTACT SWITCHES

One of the major obstacles facing the commercialization of RFMEMS contact switches is the reliability of such devices [18]. Reliability of an RFMEMS contact switch can be achieved if the device performs its desired function in a stable manner for a convenient lifetime. The desired function is isolating the electrical signal in the Off state, and conducting the same signal with a low contact resistance in the On state when a certain actuation bias is applied. The stability of operation is achieved when the contact resistance remains below a certain value and the required actuation bias remains unchanged with the aging of the device. The lifetime of an RFMEMS contact switch is usually defined by the number of switching cycles in which the contact resistance remains below a certain limit. One of the highest lifetimes reported to date is that of the Radant switch which achieved 10 billion switching cycles [1]. Some design constraints and challenges arise and have to be considered throughout the process of developing a high-reliability RFMEMS contact switch. In this chapter, some of the major reliability and design challenges of RFMEMS contact switches will be discussed together with proposed solutions to cope with these challenges in the design presented in this work.

2.1. RELIABILITY OF MICROCONTACTS

The most dominant failure mechanisms of RFMEMS contact switches are related to the presence of a direct metal-to-metal contact situation in these devices [1]. The choice of the metallic elements or alloys to be used is a critical decision and requires

knowledge of the contact characteristics of such materials. In addition, the technological processes used to deposit the contact layers determine the quality of the metallic surfaces and hence influence the microcontacts reliability. The contact materials, the technological processes and the environmental conditions determine the obtained contact resistance and the required contact force. The source of the contact force is the switch actuator which has to be designed to deliver a suitable contact force. When the data about the contact characteristics of the available materials and technology is limited, it becomes useful to prepare several designs for the actuator covering a relatively wide force range to mitigate this lack of information and allow for practical contact characterization using the fabricated devices.

2.1.1. Contact Materials

During more than a decade, several materials have been investigated by many researchers worldwide to implement the microcontacts of RFMEMS contact switches [19-24]. Pure gold has been conventionally used for this purpose because of its relative softness which provides a low contact resistance at a relatively low contact force. The low contact force requirement for gold has been very attractive as it reduces the size and design effort needed for the electrostatic actuator. A contact force of 0.1mN is typically sufficient to establish a stable contact between two clean gold surfaces giving a contact resistance around 0.1Ω [22]. While another report claims an even lower contact resistance of 0.01Ω by employing advanced contact cleaning techniques [23]. This difference in reported values illustrates the sensitivity of contact characteristics to many factors including the preparation of test samples, the cleanness of the contact surfaces, and the electrical loading conditions. The required contact

force for gold is very low if compared to the 20mN contact force needed for a conventional relay [25].

On the other hand, gold suffers from a severe reliability problem as a microcontact metal; that is its high adhesion force, causing it to be “no appropriate contact metal” according to J. Schimkat [23]. The high adhesion force of pure gold causes a pure gold-based device to fail after a short lifetime due to material transfer during switching as well as surface erosion and wear as shown in Fig. (2.1).

Two typical alternatives to pure gold have been recently proposed in several reports: hardened gold alloys and the elements of the platinum metal group. Proposed gold alloys include gold-nickel [23] and gold-platinum [19, 20] alloys. Platinum metal group member such as platinum, iridium [19], and rhodium [23] have also been suggested as suitable contact materials. A comparison of the lifetime of Au-to-Au, Au-to-Pt, Pt-to-Pt, Au-to-Ir, AuPt-to-AuPt, and Ir-to-Ir contact combinations has been reported recently by H. Kwon et al. and is shown in Fig. (2.2) [19]. It is clear from Fig. (2.2) that a platinum-platinum contact gives the best results, because of its high lifetime and relatively low contact resistance.

All the suggested alternatives to pure gold give higher contact resistance values and require higher contact force values to establish a contact. The reason for this is that they are all harder materials, and higher in bulk resistivity [19]. The exact force needed to establish a contact between two certain metallic surfaces is, again, dependent on many factors such as the materials of the two surfaces, the quality and cleanness of the surfaces, the environment of the experiments, the setup used, and the shape of the samples. Fig. (2.3) shows the contact resistance versus force characteristics for pure gold and two other contact materials. The required minimum contact force for a $gold_{(95\%)}$-$nickel_{(5\%)}$ alloy is 0.3mN and for rhodium is 0.6mN,

compared to less than 0.1mN for pure gold [23]. These specific facts motivated the need for the high force actuator design that will be presented in the following chapters of this work.

2.1.2. Rhodium as a Contact Material

Rhodium belongs to the platinum metal group together with ruthenium, palladium, osmium, iridium, and platinum. Rhodium is a hard silvery metal, inert in air and most acids. Table (2.1) presents the main physical, mechanical and electrical properties of rhodium compared to platinum and gold. The hardness and nobility of rhodium recommend it as a reliable contact material. It is logically preferred to platinum due to its higher bulk conductivity and hardness.

To practically investigate the potential of rhodium as a contact metal for RFMEMS switches, thin films of rhodium have been deposited on silicon and silicon dioxide substrates using pulsed Laser ablation of a solid rhodium target. A schematic of the setup used in the deposition process is shown in Fig. (2.4). Sample scanning electron micrographs of the surfaces of the obtained rhodium thin films are shown in Fig. (2.5). The thickness of the layers prepared ranged between 25nm and 150nm. The thickness of the layers has been visually estimated from cross-sectional SEM analysis for three of the samples performed at IMEC vzw, Belgium.

Few of the pulsed Laser deposited rhodium samples have been used to determine the contact properties of rhodium thin films while in contact with gold and platinum surfaces using a special setup that has been assembled by the reliability and modeling team at IMEC vzw, Belgium. The setup employs a stepper motor-driven needle attached to a piezoelectric force sensor of 0.3mN precision. The stepper motor and the sensor are controlled using a standard computer port. During a measurement, the

stepper motor drives the needle slowly downwards causing increasing force on the top side of the top triangular sample shown in Fig. (2.6). The force sensor reads out the applied force and a Kelvin setup is used to measure the resistance at each motor step. The resistance and force values at each step are recorded.

The electrical setup and current flow in the test structures are illustrated in Fig. (2.7). A current is forced to flow between probe 1 and probe 3, and the voltage between probe 2 and probe 3 is measured, and hence the resistance between the symmetry line AA' and probe 3 is determined. However, the contact resistance is only a part of the measured resistance due to the series-resistive contribution of the metal layers on the top and bottom samples. To determine the value of the top sample resistance (R_{F1}), the setup in Fig. (2.8) is used, and to determine the value of the bottom sample resistance (R_{F2}), the setup in Fig. (2.9) is used. The obtained results for contact resistance/force characteristics for rhodium with both gold and platinum are shown in Fig. (2.10) and (2.11). The results indicate a minimum contact force less than the sensor least readable value, 0.3mN, between rhodium and gold. A minimum contact force of around 2.6mN could be observed between rhodium and platinum.

To ensure the cleanness of the test, the triangular gold and platinum top samples were coated with a protective photoresist layer which was removed directly before the test to ensure the freshness of the contact bumps. However, a similar procedure could not be followed with the bottom rhodium samples. This affected the reproducibility of the measurements. Furthermore, the top triangular samples were free to travel laterally under the influence of the force needle which affected the stability of the setup during each measurement. A microfabricated test structure will be presented later for on-wafer characterization of contact resistance/force of the available contact materials.

The presence of small droplets on the rhodium samples can be observed in Fig. (2.5) and is a typical drawback of pulsed Laser deposition. This is believed to affect the reliability of such PLD prepared thin films as microcontact surfaces, unless the density and sizes of the droplets are well controlled [26].

2.2. AIR GAP BREAKDOWN

The electrostatic attraction force of a parallel-plate electrostatic actuator is given by [1]

$$F_e = \frac{1}{2}\frac{\varepsilon_0 A V^2}{d^2} = \frac{1}{2}\varepsilon_0 A \varepsilon^2 \tag{2.1}$$

where A is the actuator area, V is the applied voltage, d is the gap spacing between the electrodes, and ε is the present electric field which equals V/d. It becomes clear from Eq. (2.1) that the force delivered by any parallel-plate electrostatic actuator is linearly proportional to the area of the electrodes, and proportional to the square of the present electric field. This indicates the significance of the electrostatic breakdown of the medium between the actuator electrodes. Increasing the applied electric field clearly boosts the obtained contact force, but a critical electric field value must not be exceeded to avoid the breakdown of the medium between the two electrodes and the failure of the device. A typical testing environment employs atmospheric-pressure air as a host medium for the actuator.

The main cause of electrostatic breakdown in a MEMS actuator with gap spacing between 2nm and 5μm is field emission of electrons [27]. In this breakdown mechanism, free electrons inside the metal lattice are detached when they are near the surface due to high attraction, and plasma is formed near the metal surface. When this plasma expands and reaches the anode, a spark is formed [28]. This phenomenon is

sensitive to the metal type and its surface properties. The modified Paschen curve shown in Fig. (2.12) takes field emission into account, and estimates the breakdown field for air at 1atm as 75V/μm for gaps below 5μm. Few experimental results have been reported on the breakdown of air in very small gaps between two metallic surfaces, as illustrated in Table (2.2). The minimum reported breakdown field is 50V/μm between an aluminum cathode and a nickel anode for 0.25-1.5μm gaps [29]. This value will be considered as a recommended upper limit for the electric field present in the actuator gap throughout this work. Test structures will be presented in the following chapters to help measuring the actual on-wafer breakdown field for the available materials and technology.

It is worth mentioning that the polarity of the applied voltage to the electrostatic actuator has no effect on the obtained force, thus exchanging the cathode and anode will not affect the obtained force but may alter the breakdown field which is sensitive to the cathode material properties and surface quality. This should be considered for experimental validation.

2.3. MECHANICAL STABILITY

Several mechanical design challenges have to be considered while developing a reliable RFMEMS contact switch design [1]. The mechanical design seeks the satisfaction of the main actuator design goal; that is the high contact force in our case. Nevertheless, some mechanical reliability constraints and challenges have to be concerned about.

A static mechanical analysis of the electrostatic actuator determines the upper electrode deflection profile and the contact force obtained for a certain applied voltage as will be explained in Chapter 3. The initial electrode profile is conventionally

assumed horizontally planar in such analysis. However, the technological processes employed to fabricate the actuator result in a vertical stress gradient in the structure, causing a permanent deflection of the released beam prior to applying the actuation bias. This stress gradient-induced deflection has to be within the allowed limits estimated from the properties of the final design reached. A problem-aware design should employ a large initial separation between the fixed and free electrodes to lessen the effect of such initial deflections as will be explained in later chapters.

From a dynamical point of view, the top electrode of an electrostatic actuator represents a high order spring-mass system which possesses fundamental and harmonic mechanical resonance frequencies; the values of which depend on the mass of the beam, the stiffness of its suspension spring, and the shape of the overall structure. An acceptable range for the fundamental resonant frequency of electrostatic RFMEMS switches is 10-200KHz [1]. This range ensures the isolation of the system from any external mechanical vibrations.

Another mechanical design challenge is the presence of the release holes in the beam as shown in Fig. (2.13). These holes are necessary to successfully etch away the sacrificial layer under the top electrode to release the structure. They are also useful for reducing the squeeze film damping, allowing for smaller switching time. This simply means they represent uniformly distributed exits for the air molecules under the beam, thus lowering the pressure of these air molecules which resists the downward motion of the beam. On the other hand, these holes reduce the overall rigidity of the beam causing a lower effective Young's modulus than predicted from material properties. This deviation in the beam rigidity has to be considered during the design process. A technological solution to this issue is a slight increase in the beam

thickness while fabricating the device to increase the beam rigidity and effectively return to the expected rigidity.

2.4. PACKAGING

Packaging of RFMEMS contact switches is vital for their reliability. These devices are very sensitive to humidity and environmental contaminants as explained before in the discussion on microcontacts reliability. Hermetic packaging in nitrogen or dry air environments is recommended [1]. Though very critical for the performance of RFMEMS contact switches, this challenge is mainly a technological and cost challenge rather than a design issue.

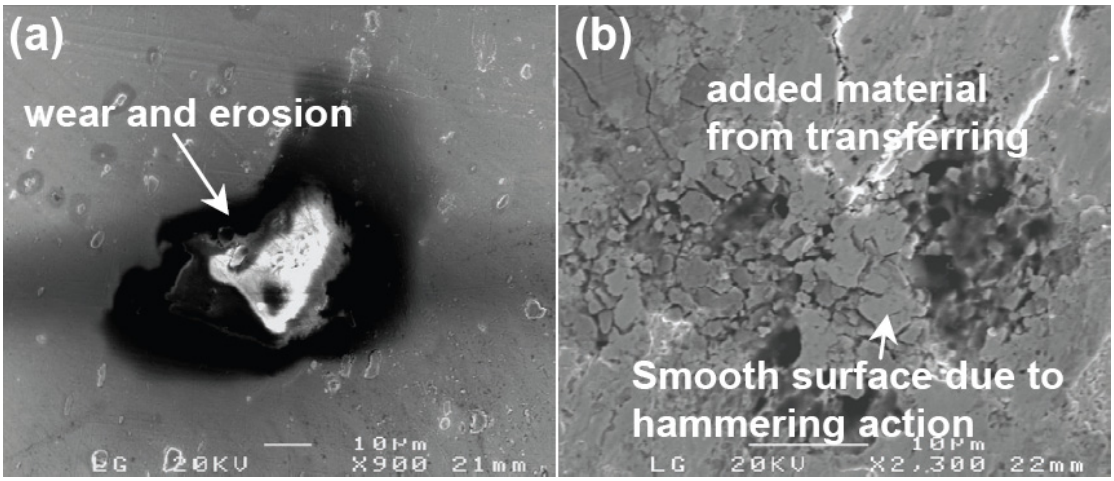

Figure 2.1. SEMs of sample gold contact surfaces after failure due to wear, erosion (a), and material transfer (b) (after [19]).

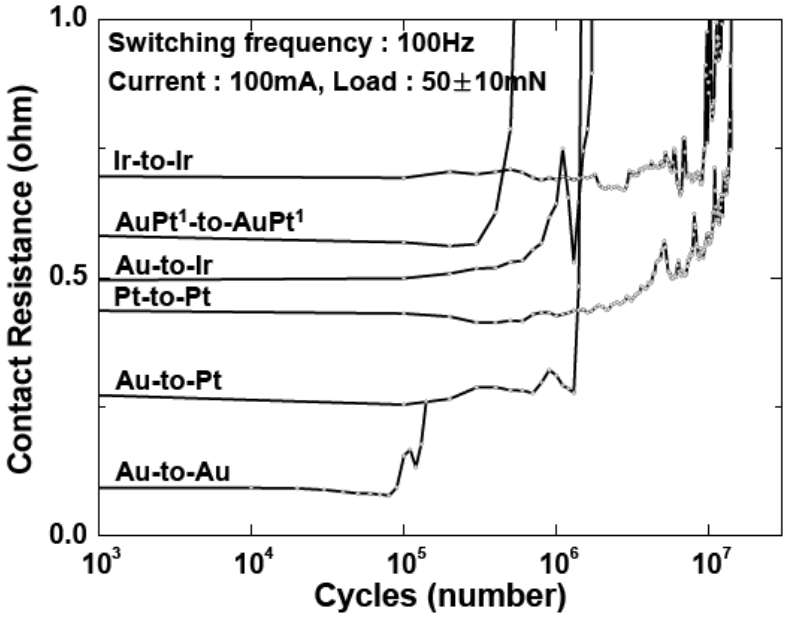

Figure 2.2. Lifetime comparison for different contact materials combinations. The sharp rise in contact resistance represents the failure of the contact and the end of its lifetime (after [19]).

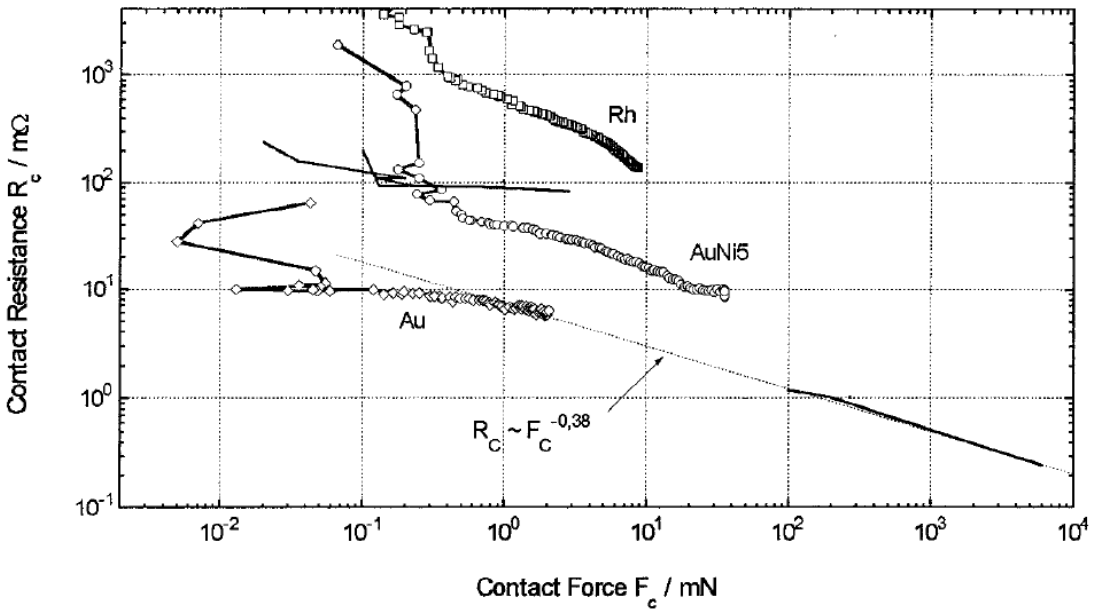

Figure 2.3. Contact resistance/force characteristics of pure gold, a gold-nickel alloy, and rhodium (after [23]).

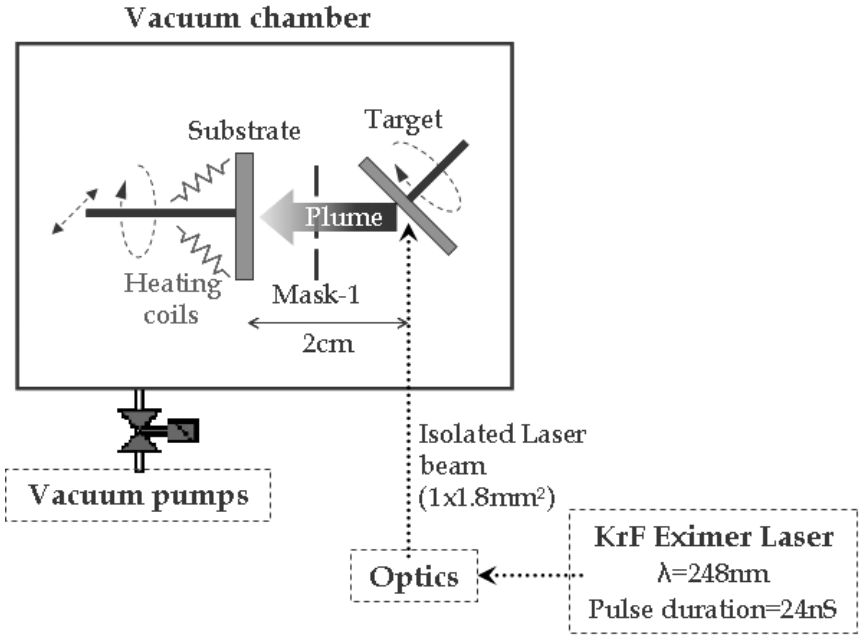

Figure 2.4. A schematic diagram of the PLD setup at STRC, AUC, Egypt.

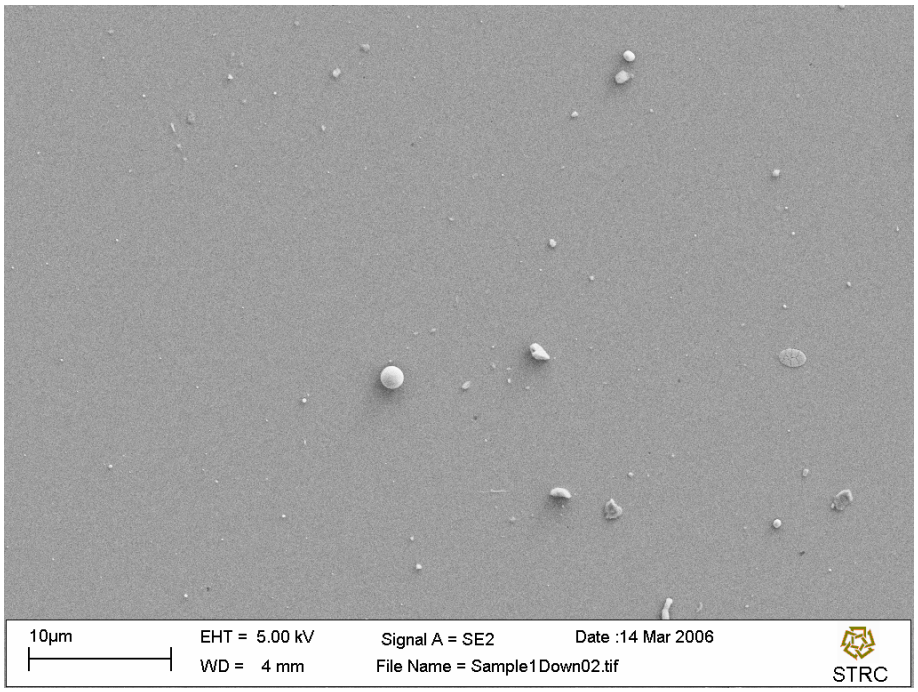

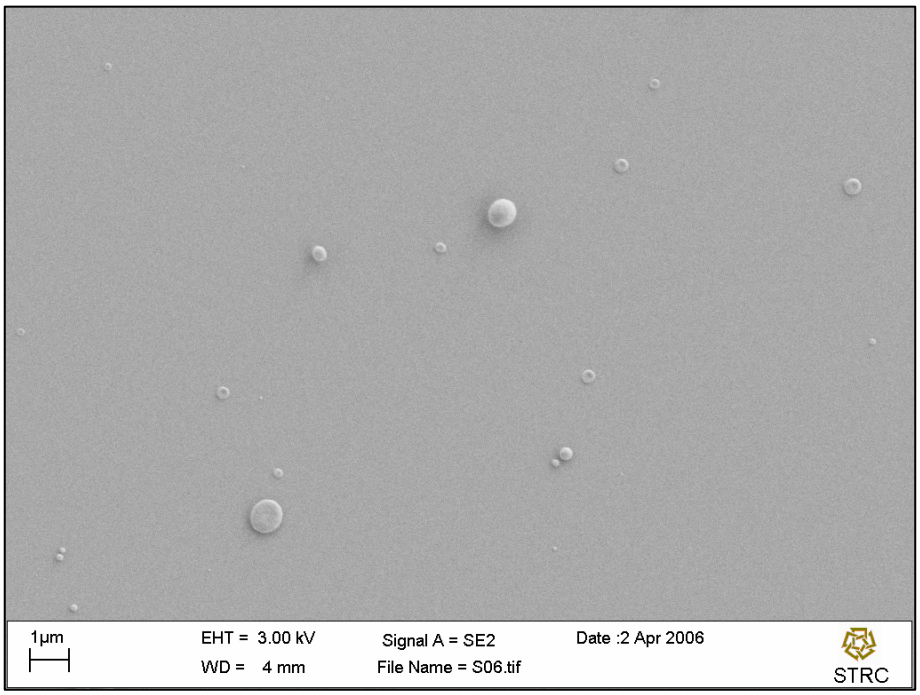

Figure 2.5. SEM of two different rhodium thin film samples prepared using the PLD setup at STRC, AUC, Egypt.

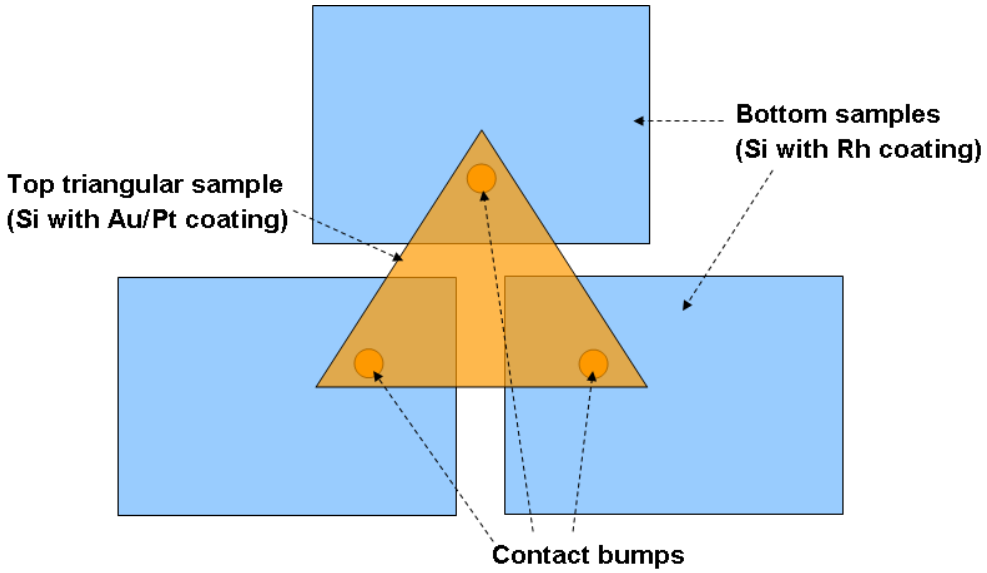

Figure 2.6. Diagram of the test structures used to characterize the contact resistance/force behavior of rhodium with gold and platinum.

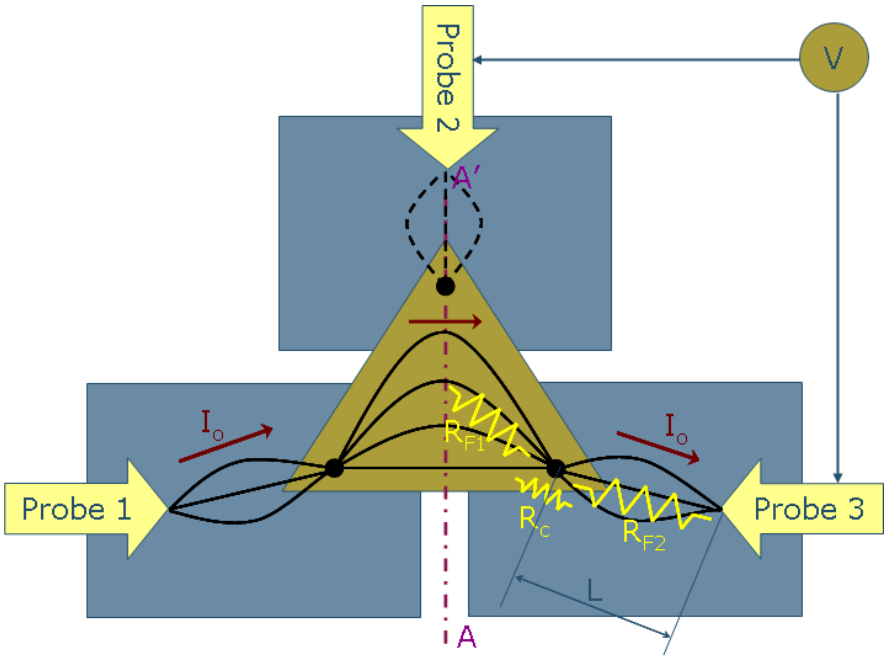

Figure 2.7. Diagram of the electrical setup and current flow for the resistance measurement.

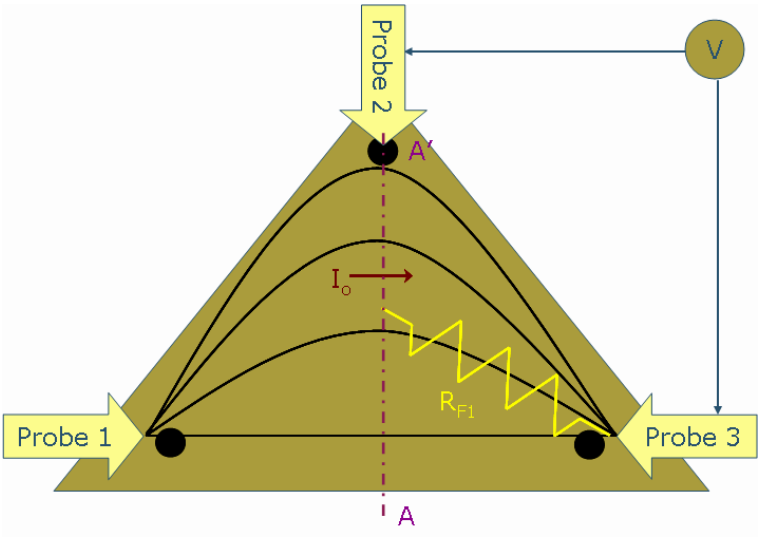

Figure 2.8. The technique of measuring the resistive contribution of the top sample.

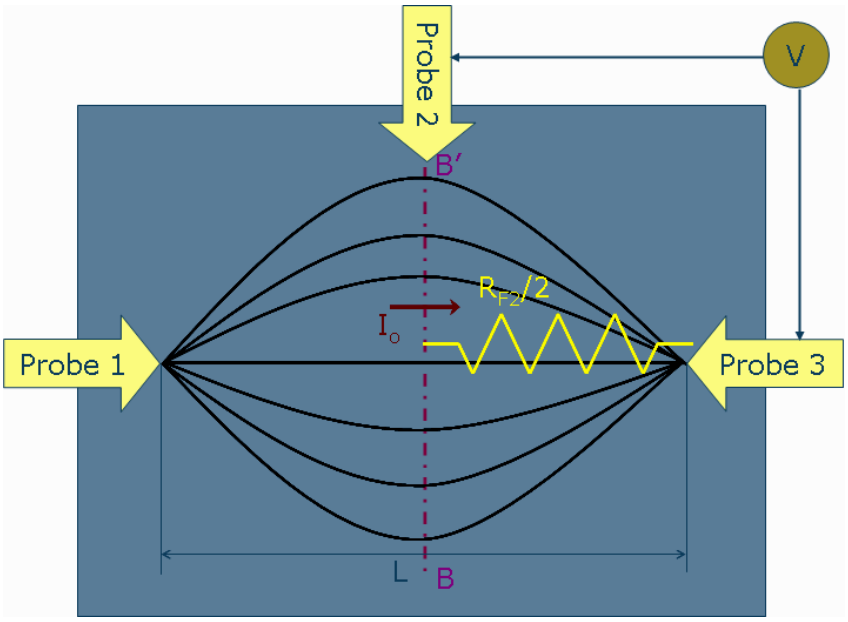

Figure 2.9. The technique of measuring the resistive contribution of the bottom sample. The length (L) is the same as shown in Fig. (2.7).

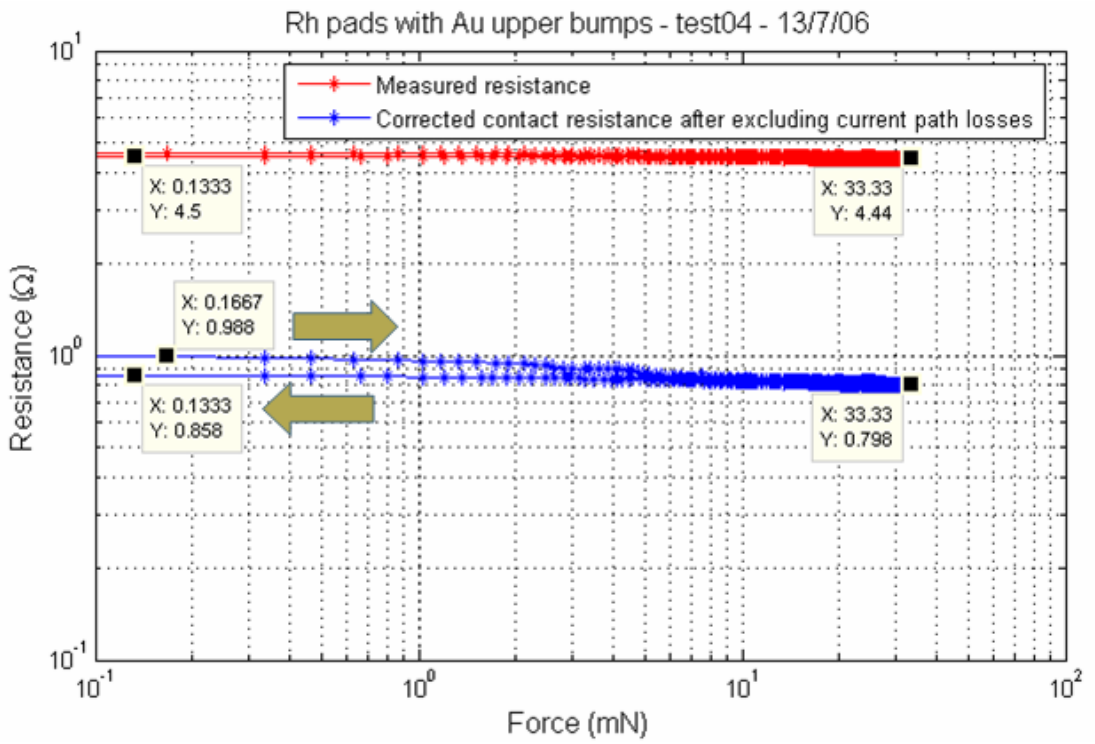

Figure 2.10. Contact resistance versus contact force for rhodium/gold interface. The resistance of Probe 3 is not excluded in the corrected curve.

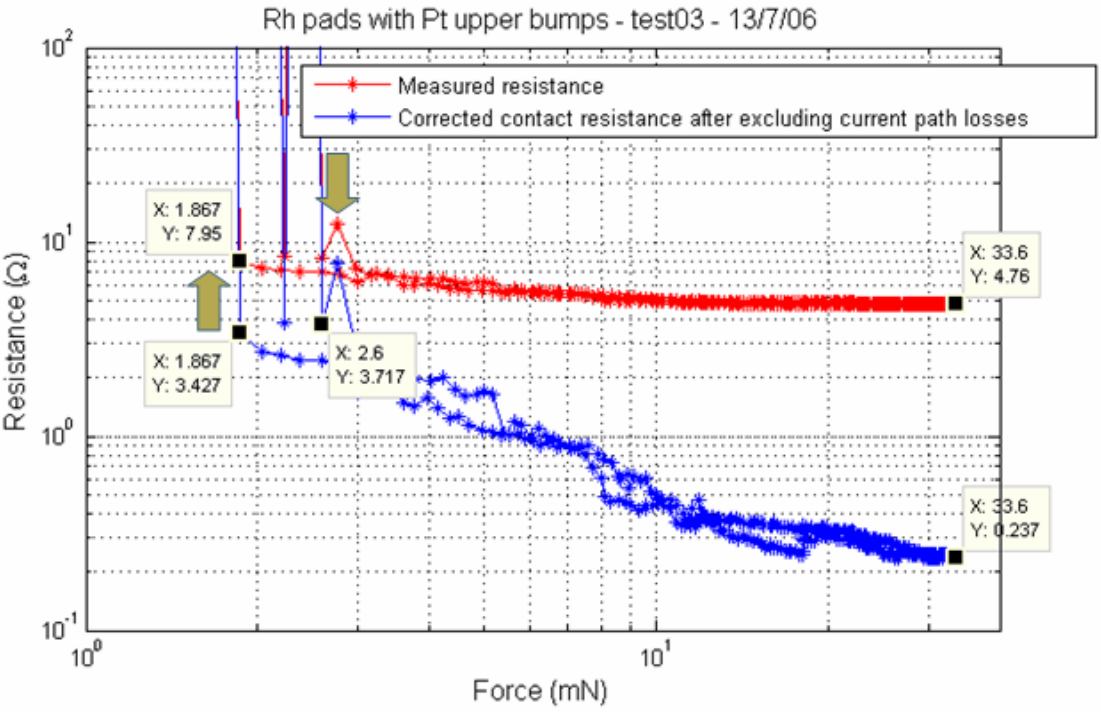

Figure 2.11. Contact resistance versus contact force for rhodium/platinum interface. The resistance of Probe 3 is not excluded in the corrected curve.

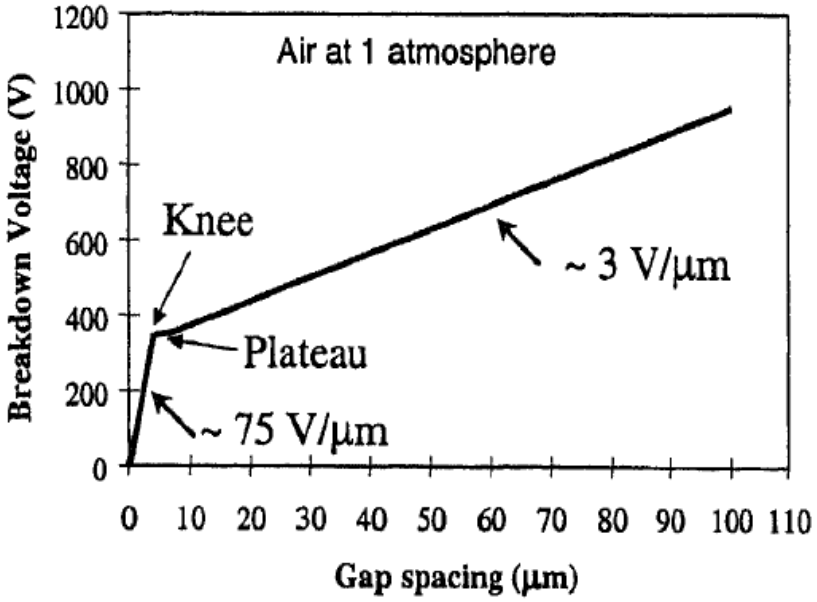

Figure 2.12. Modified Paschen curve, indicating a breakdown field of around 75V/µm for gaps smaller than 5µm (after [27]).

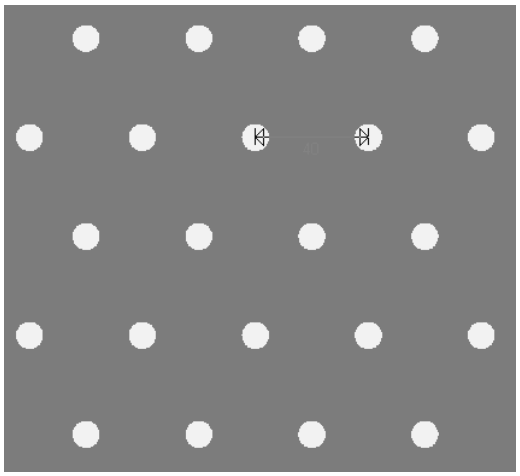

Figure 2.13. Top view of part of an actuator beam indicating the presence of release holes. The holes are 10µm in diameter, with a horizontal pitch of 40µm.

Property	Unit	Rhodium	Platinum	Gold
Density	g/cm^3	12.4	21.45	19.32
Melting point	°C	1960	1769	1063
Elasticity modulus	GPa	359	152	80
Bulk resistivity	μΩ.cm	4.3	9.8	2.2

Table 2.1. Comparing the main physical, mechanical and electrical properties of rhodium, platinum and gold [30].

Gap spacing (μm)	Cathode material	Anode material	Breakdown field (V/μm)	Reference
0.9	chrome	chrome	156	[27]
<2.5	iron	silver	70	[31]
0.25-1.5	aluminum	nickel	50	[29]

Table 2.2. Experimental results reported in the literature on the electrostatic breakdown field of small air gaps.

CHAPTER 3

SEMI-ANALYTICAL MODEL FOR ELECTROSTATICALLY ACTUATED BEAMS

In order to achieve the goal of designing a high force RFMEMS contact switch and to be able to handle all the challenges described in Chapter 2, an accurate and fast model for the problem has to be developed. The speed of the solution normally contradicts with its accuracy. The most accurate known solution for an electrostatically actuated beam problem is a full 3D finite element analysis of the complete structure of the device. A typical solution time on an up-to-date desktop PC using a commercial finite element analysis tool optimized for MEMS analysis ranges between few minutes and few hours for an electrostatically actuated beam problem at given actuation voltage, in addition to the time consumed in modeling the problem geometry and describing the materials properties and boundary conditions. The exact time depends on the details of the structure and number of the mesh finite elements. The accuracy and solution time increase with increasing the number of mesh elements. If the designer needs to sweep any of the design parameters of a certain structure or even sweep the actuation voltage, then the solution time range jumps up between few hours and few days.

On the other hand, the fastest solution to the same problem is achieved by simplifying the problem to a parallel-plate capacitor with the top plate suspended by a spring of certain stiffness as explained in the following section. The oversimplification of the problem and neglecting details like the deflection profile of the top plate and the nonuniformity of the attraction force are the main causes of the inaccuracy of such solution. The numerical evaluation of the simple equations governing this simplified

model can take a fraction of a second using a general-purpose mathematical tool like MATLAB®.

The third approach to the problem in hand is to use the beam deflection theory [32], together with the fundamental electrostatic attraction equations. This is the intermediate custom solution of the problem. Section 3.2 describes the development of this model, and the results it gives are compared to both the simplified analytical solution and the 3D finite element analysis.

3.1. SIMPLIFIED ANALYTICAL MODEL

For the switch structure shown in Fig. (3.1), Eq. (2.1) describes the electrostatic attraction force and can be rewritten as

$$F_{e-\max} = \frac{1}{2}\frac{\varepsilon_0 A V_{\max}^2}{d_{\min}^2} = \frac{1}{2}\varepsilon_0 A \varepsilon_{\max}^2 \tag{3.1}$$

where $F_{e-\max}$ is the maximum obtained electrostatic force, $d_{\min}$ is the minimum spacing between the plates in the On state, and $\varepsilon_{\max}$ is the maximum allowed electric field in the structure which has been previously estimated as 50V/μm.

The spring constant of the fixed-fixed flexures of the structure is given by [1]

$$k_s = 4Ew_s\left(\frac{t}{L_s}\right)^3 \tag{3.2}$$

where E is Young's modulus of the flexures material, t is the thickness, w_s is the width, and L_s is the length of each of the flexures.

Now the mechanical restoring force due to the travel of the top beam to any lower position is given by

$$F_r = k_s\left(d_0 - d\right) \tag{3.3}$$

where d is the final gap height.

Solving Eq. (2.1) and (3.3) to obtain the a relationship between the gap height and the applied voltage, we get

$$V = \sqrt{\frac{2k_s d^2 \left(d_0 - d\right)}{\varepsilon_0 A}} \tag{3.4}$$

Eq. (3.4) can be rearranged as follows

$$\frac{V}{\alpha} = \frac{d}{d_0}\sqrt{1 - \frac{d}{d_0}} \quad ;\alpha = \sqrt{\frac{2k_s d_0^3}{\varepsilon_0 A}} \tag{3.5}$$

where α is a constant. Fig. (3.2) plots the relation between V/α and d/d_0. The plot shows that there are two equilibrium solutions for the equation, with a critical solution point at the maximum voltage on the curve where the gap height is 2/3 its initial value. If the applied voltage reaches or exceeds this maximum voltage, or pull-in voltage, the forces on the beam are no more in equilibrium and it collapses to its lowest allowed position. The pull-in voltage is given by

$$V_{PI} = V\big|_{d=\frac{2}{3}d_0} = \sqrt{\frac{8k_s d_0^3}{27\varepsilon_0 A}} \tag{3.6}$$

At this point, a design constraint is observed which necessitates that the pull-in voltage is lower than the breakdown voltage of air when the beam is in the down state. The applied voltage has to exceed the pull-in voltage to pull the beam down to the contact situation, assuming that $d_{\min} < 2d_0/3$.

In the down state, the electrostatic attraction is higher than the restoring force of the springs. The difference between these two forces appears as a pressing force at the three pairs of bumps shown in Fig. (3.1). The contact force is the pressing force at the middle pair of bumps. Using Eq. (3.1-3.3), the contact force can be given by

$$F_C = \frac{F_e - F_r}{3}$$
$$= \frac{1}{6}\varepsilon_0 A\varepsilon_{\max}^2 - \frac{k_s}{3}\left(d_0 - d_{\min}\right) \tag{3.7}$$
$$= \frac{1}{6}\varepsilon_0 A\varepsilon_{\max}^2 - \frac{4}{3}Ew_s\left(\frac{t}{L_s}\right)^3\left(d_0 - d_{\min}\right)$$

assuming a uniform distribution of the force among the three pairs of bumps.

Considering a typical structure with the parameters shown in Table (3.1), the obtained contact force at the middle pair of contact bumps is around 1.2mN at 50V applied bias. The pull-in voltage has been calculated using Eq. (3.6) as 38.8V for this specific structure. At 42V, the model predicts a contact force of 0.76mN.

It may be argued that losing 2/3 of the useful force at the two pairs of bumps at the sides of the actuator is not justified. They have been presented to enhance the stability of the beam in the contact mode as they prevent further collapse of the beam at the corners due to electrostatic attraction. This argument uncovers a drawback of this simplified model which does not give any information about the stiffness of the beam against possible collapse at the corners, and does not tell where are the optimum positions for those supporting bumps to prevent the beam collapse and preserve the highest portion of the usable force for the contact bumps.

3.2. A 2.5D SEMI-ANALYTICAL MODEL

A different approach is now considered for a similar problem as in the previous section. The new approach is more general and capable of solving both cantilever and bridge, or fixed-fixed, type beams. The cantilever problem is presented first and then a modification is described to handle the bridge problem. The solution of either the cantilever or the bridge problem is subdivided into three stages; each with different loading conditions. The fact that the solution is performed in a 2D manner with

consideration of some of the parameters in the third dimension is the reason why it is termed a 2.5D model.

3.2.1. Before Pull-in

The cantilever beam problem shown in Fig. (3.3) can be represented by the 2D free body diagram in Fig. (3.4) in case of no contact at the end tip, or before pull-in. This free body diagram represents a statically determinate problem, as the number of reactions, which are P and M_0, is equal to the number of independent equations of equilibrium, which are the moment and vertical force equilibrium equations. The only external load in this problem is the nonuniform distributed electrostatic attraction force, $q(u(x))$. To determine the equilibrium beam profile, we have to solve the basic differential equation of the deflection curve. A derivation from first principles for the deflection curve equation can be found in [32], yielding the relation

$$M_{(x)} = EI_{(x)} \frac{d^2 u_{(x)}}{dx^2} \tag{3.8}$$

where E is the modulus of elasticity of the beam material, and $I_{(x)}$ is the area moment of inertia of the beam around the beam axis. The product $EI_{(x)}$ is the flexural rigidity, and is a function of position because of the dependence of the area moment of inertia on the width and thickness of the beam which can vary from one section to the other as shown in Fig. (3.3). It can be easily shown that the area moment of inertia of a beam of rectangular cross-section is given by [32]

$$I = \frac{wt^3}{12} \tag{3.9}$$

where w is the beam width and t is its thickness.

The next step is trying to find the bending moment as a function of position. Using the diagrams in Fig. (3.5), it can be shown that

$$M_{(x)} = \begin{cases} -M_0 + Px & ; 0 < x < x_{e1} \\ -M_0 + Px - \int_{x_{e1}}^{x} q_{\left(u_{(\hat{x})}\right)} \left(x - \hat{x}\right) d\hat{x} & ; x_{e1} < x < x_{e2} \\ -M_0 + Px - \int_{x_{e1}}^{x_{e2}} q_{\left(u_{(\hat{x})}\right)} \left(x - \hat{x}\right) d\hat{x} & ; x_{e2} < x < l \end{cases} \tag{3.10}$$

The reactions at the anchor can be obtained by applying the moment and vertical force equilibrium equations for the external load and reactions on the free body diagram in Fig. (3.4) as follows

$$\begin{aligned} M_0 &= \int_{x_{e1}}^{x_{e2}} \hat{x} q_{\left(u_{(\hat{x})}\right)} d\hat{x} \\ P &= \int_{x_{e1}}^{x_{e2}} q_{\left(u_{(\hat{x})}\right)} d\hat{x} \end{aligned} \tag{3.11}$$

The electrostatic attraction distributed load is obtained by differentiating Eq. (2.1) with respect to the beam length, given that the area is the product of the width and length. This yields

$$q_{\left(u_{(\hat{x})}\right)} = \frac{d}{dL}\left(\frac{1}{2}\frac{\varepsilon_0 \left(w_2 \cdot L\right) V^2}{d^2}\right) = \frac{1}{2}\frac{\varepsilon_0 V^2 w_2}{\left[d_0 + u_{(x)}\right]^2} \tag{3.12}$$

where w_2 is the width of the actuated section of the beam as in Fig. (3.3).

At this point, the nonlinearity of the problem is noticeable. The unknown deflection function in Eq. (3.8), $u_{(x)}$, is present to the second degree in the denominator of the electrostatic distributed force which is part of the several integrals used to obtain the bending moment on other side of Eq. (3.8). This nonlinearity does not allow for an analytical solution to Eq. (3.8), and a numerical solution is needed [33].

Substituting from Eq. (3.9-3.12) into Eq. (3.8), and taking into account the substitution with the appropriate beam width into the area moment of inertia of each of the three beam sections, we get

$$\frac{d^2u_{(x)}}{dx^2}=\begin{cases}\dfrac{6\varepsilon_0 V^2 w_2}{Ew_1t_1^3}\left(\displaystyle\int_{x_{e1}}^{x_{e2}}\frac{d\hat{x}}{\left[d_0+u_{(\hat{x})}\right]^2}-\int_{x_{e1}}^{x_{e2}}\frac{\hat{x}d\hat{x}}{\left[d_0+u_{(\hat{x})}\right]^2}\right) & ;0<x<x_{e1}\\ \dfrac{6\varepsilon_0 V^2}{Et_2^3}\left(\displaystyle\int_{x_{e1}}^{x_{e2}}\frac{d\hat{x}}{\left[d_0+u_{(\hat{x})}\right]^2}-\int_{x_{e1}}^{x_{e2}}\frac{\hat{x}d\hat{x}}{\left[d_0+u_{(\hat{x})}\right]^2}-\int_{x_{e1}}^{x}\frac{(x-\hat{x})d\hat{x}}{\left[d_0+u_{(\hat{x})}\right]^2}\right) & ;x_{e1}<x<x_{e2}\\ 0 & ;x_{e2}<x<l\end{cases} \tag{3.13}$$

Eq. (3.13) can be numerically evaluated using an iterative approach. An initial deflection profile has to be assumed and used to evaluate the integrals on the right hand side, and then the ordinary differential equation is solved for the new deflection curve $u_{(x)}$. This new deflection curve is iterated back to evaluate the integrals, and so on. This procedure is repeated until convergence is observed for the deflection curve.

The model developed so far is capable of performing two useful functions, which are the prediction of the deflection curve of any cantilever beam structure at any applied voltage as well as detecting the pull-in of the beam. The exact calculation of the deflection curve is significant for the design of capacitive switch structures. Pull-in is detected by the divergence of the iterative solution of the differential equation and the quick collapse of the cantilever free end to the minimum gap height. Further increase in the applied voltage above the pull-in voltage always yields a divergent solution.

The structural parameters of a sample structure are illustrated in Table (3.2), and the results of the semi-analytical model are shown in Fig. (3.6), together with the results of simulating the same problem with CoventorWare. The error in calculating the tip

deflection is less than 0.3%, and the time needed for the semi-analytical model solution is in the order of 0.5sec for 6 iterations, against 10-20 minutes for the CoventorWare simulation. A detailed discussion of the procedure of simulating such beam structures using CoventorWare is presented in Chapter 4. The iterative solution of the semi-analytical model is performed using MATLAB®, employing its built-in numerical ordinary differential equation solver. Fig. (3.7) shows a flowchart which describes the algorithm developed to solve model equation, additionally allowing for a sweep for any of the design parameters or the voltage.

3.2.2. After First Pull-in

Further increase of the applied voltage to the sample structure number (2) causes the beam tip to pass across the contact bump as shown in Fig. (3.8). After pull-in occurs, the cantilever beam tip deflection is restricted to a certain value, h_t. Thus a new reaction appears in the free body diagram as shown in Fig. (3.9). The new reaction is the contact force.

The problem is statically indeterminate because of the presence of three reactions against only two equilibrium equations. The missing equation is the boundary condition restricting the beam deflection at the end point according to the bump height. In an analytical fashion, one would solve for the deflection curve using an unknown contact force which is later obtained by applying the boundary condition to the obtained deflection curve. However, this is not possible in a numerical solution. The numerical value of the contact force has to be known prior to attempting to numerically obtain the deflection curve. The approach in this situation is a numerical search for the value of the contact force which satisfies the boundary condition.

In order to find the bending moment function, the diagrams in Fig. (3.5) describe the current situation, thus Eq. (3.10) still expresses the bending moment function. However, the equilibrium equations are different from the previous case because of the introduction of the contact force. The reactions at the anchor become

$$M_0 = \int_{x_{e1}}^{x_{e2}} \hat{x} q_{\left(u_{(\hat{x})}\right)} d\hat{x} - F_C l$$
$$P = \int_{x_{e1}}^{x_{e2}} q_{\left(u_{(\hat{x})}\right)} d\hat{x} - F_C \tag{3.14}$$

Substituting as before from Eq. (3.9, 3.10, 3.12, 3.14) into Eq. (3.8), we get

$$\frac{d^2 u_{(x)}}{dx^2} = \begin{cases} \dfrac{6\varepsilon_0 V^2 w_2}{E w_1 t_1^3}\left(x\int_{x_{e1}}^{x_{e2}} \dfrac{d\hat{x}}{\left[d_0 + u_{(\hat{x})}\right]^2} - \int_{x_{e1}}^{x_{e2}} \dfrac{\hat{x} d\hat{x}}{\left[d_0 + u_{(\hat{x})}\right]^2} \right) + \dfrac{12 F_C}{E w_1 t_1^3}(l - x) & ; 0 < x < x_{e1} \\ \dfrac{6\varepsilon_0 V^2}{E t_2^3}\left(x\int_{x_{e1}}^{x_{e2}} \dfrac{d\hat{x}}{\left[d_0 + u_{(\hat{x})}\right]^2} - \int_{x_{e1}}^{x_{e2}} \dfrac{\hat{x} d\hat{x}}{\left[d_0 + u_{(\hat{x})}\right]^2} - \int_{x_{e1}}^{x} \dfrac{(x - \hat{x}) d\hat{x}}{\left[d_0 + u_{(\hat{x})}\right]^2} \right) + \dfrac{12 F_C}{E w_2 t_2^3}(l - x) & ; x_{e1} < x < x_{e2} \\ \dfrac{12 F_C}{E w_3 t_2^3}(l - x) & ; x_{e2} < x < l \end{cases} \tag{3.15}$$

Eq. (3.15) is only different from Eq. (3.13) by the introduction of the contact force terms.

Using sample structure number (2) as before, a comparison between the results of the semi-analytical model and CoventorWare simulation at 30V is shown in Fig. (3.10). The contact force of the device has been calculated with less than 0.4% error compared to the finite element simulation. The time needed to perform the semi-analytical model iterations is in the order of 10 seconds, against 40-60 minutes for the finite element simulation.

The algorithm used to implement the model after first pull-in is similar to the iterative algorithm used before pull-in, with additional steps to find the value of the contact force which satisfies the problem boundary condition for each iteration. The flowchart in Fig. (3.11) explains the algorithm developed for this part of the model.

In brief terms, the algorithm keeps iterating the deflection curve until convergence in the obtained contact force value is observed. The contact force is given a zero initial value, and the deflection curve is given the profile shown in Fig. (3.12). Other assumptions for the initial deflection curve yield approximately the same results, but may affect the number of iterations needed to reach the converged solution. More realistic assumptions yield lower number of iterations. Within each iteration, the contact force value is incremented and the solution is repeated until the boundary condition at the contact tip is satisfied. The steps of incrementing or decrementing the contact force are not constant. The increments are initially coarse, but as the boundary condition is approached, successive bisections of the incrementing or decrementing step yield a very fine resolution for the obtained contact force which satisfies the boundary condition.

3.2.3. After Second Pull-in

Further increase of the electrostatic attraction on the beam of sample structure number (2), causes the beam to collapse near its middle because it is now supported from both ends by the anchor and contact bump. This second pull-in is considered a failure mode for the device as it causes the two electrostatic actuator electrodes to be short-circuited. No isolation dielectric layer is introduced between the electrodes in the proposed structure to simplify the switch fabrication technology and avoid any dielectric charging problems [1].

A third sample structure is described in Table (3.3) for further illustration. Fig. (3.14) shows that this structure gives a maximum contact force of 0.328mN at 34V before the device fails due to second pull-in at 35V. The semi-analytical model is always capable of detecting the maximum electric field present in the structure by dividing the applied voltage value by the spacing between the bottom electrode and the nearest point on the beam curve. The maximum field in this case is 31.6V/μm as shown in Fig. (3.14). It is still below the recommended upper limit which is 50V/μm. To enhance the structure performance, we can shorten the structure springs to 250μm. The result of this modification is having 0.697mN contact force at maximum electric field of 50.6V/μm. This is almost the optimum operation point for the given actuator size and beam thickness.

Further improvement of the contact force requires modifying the proposed geometry in Fig. (3.3). A suggested improvement to the situation is adding another bump, or a stopper, to the beam within the range of the bottom electrode to provide a third suspension point for the beam as shown in Fig. (3.16).

This new situation involves a new reaction at the stopper as shown in the free body diagram in Fig. (3.17). The new problem is also statically indeterminate because of the presence of four reactions against two equilibrium equations. The two remaining equations are the boundary conditions at the contact and stopper bumps restricting the deflection curve to certain values at these two points.

The diagrams in Fig. (3.18) allow for the calculation of the bending moment as follows

$$M_{(x)} = \begin{cases} -M_0 + Px & ; 0 < x < x_{e1} \\ -M_0 + Px - \int_{x_{e1}}^{x} q_{\left(u_{(\hat{x})}\right)} \left(x - \hat{x}\right) d\hat{x} & ; x_{e1} < x < x_s \\ -M_0 + Px - \int_{x_{e1}}^{x} q_{\left(u_{(\hat{x})}\right)} \left(x - \hat{x}\right) d\hat{x} + R\left(x - x_s\right) & ; x_s < x < x_{e2} \\ -M_0 + Px - \int_{x_{e1}}^{x_{e2}} q_{\left(u_{(\hat{x})}\right)} \left(x - \hat{x}\right) d\hat{x} + R\left(x - x_s\right) & ; x_{e2} < x < l \end{cases} \tag{3.16}$$

Referring to Fig. (3.17), the equilibrium equations can be written as

$$\begin{aligned} M_0 &= \int_{x_{e1}}^{x_{e2}} \hat{x} q_{\left(u_{(\hat{x})}\right)} d\hat{x} - F_C l - R x_s \\ P &= \int_{x_{e1}}^{x_{e2}} q_{\left(u_{(\hat{x})}\right)} d\hat{x} - F_C - R \end{aligned} \tag{3.17}$$

Substituting as before from Eq. (3.9, 3.12, 3.16, 3.17) into Eq. (3.8), we get

$$\frac{d^2 u_{(x)}}{dx^2} = \begin{cases} \dfrac{6\varepsilon_0 V^2 w_2}{E w_1 t_1^3} \left(x \int_{x_{e1}}^{x_{e2}} \dfrac{d\hat{x}}{\left[d_0 + u_{(\hat{x})}\right]^2} - \int_{x_{e1}}^{x_{e2}} \dfrac{\hat{x} d\hat{x}}{\left[d_0 + u_{(\hat{x})}\right]^2} \right) & \\ \qquad + \dfrac{12}{E w_1 t_1^3} \left[F_C \left(l - x\right) + R\left(x_s - x\right) \right] & ; 0 < x < x_{e1} \\ \dfrac{6\varepsilon_0 V^2}{E t_2^3} \left(x \int_{x_{e1}}^{x_{e2}} \dfrac{d\hat{x}}{\left[d_0 + u_{(\hat{x})}\right]^2} - \int_{x_{e1}}^{x_{e2}} \dfrac{\hat{x} d\hat{x}}{\left[d_0 + u_{(\hat{x})}\right]^2} - \int_{x_{e1}}^{x} \dfrac{\left(x - \hat{x}\right) d\hat{x}}{\left[d_0 + u_{(\hat{x})}\right]^2} \right) & \\ \qquad + \dfrac{12}{E w_2 t_2^3} \left[F_C \left(l - x\right) + R\left(x_s - x\right) \right] & ; x_{e1} < x < x_s \\ \dfrac{6\varepsilon_0 V^2}{E t_2^3} \left(x \int_{x_{e1}}^{x_{e2}} \dfrac{d\hat{x}}{\left[d_0 + u_{(\hat{x})}\right]^2} - \int_{x_{e1}}^{x_{e2}} \dfrac{\hat{x} d\hat{x}}{\left[d_0 + u_{(\hat{x})}\right]^2} - \int_{x_{e1}}^{x} \dfrac{\left(x - \hat{x}\right) d\hat{x}}{\left[d_0 + u_{(\hat{x})}\right]^2} \right) & \\ \qquad + \dfrac{12}{E w_2 t_2^3} F_C \left(l - x\right) & ; x_s < x < x_{e2} \\ \dfrac{12 F_C}{E w_3 t_2^3} \left(l - x\right) & ; x_{e2} < x < l \end{cases} \tag{3.18}$$

The results of solving Eq. (3.18) numerically for sample structure number (3) at 40V are compared to CoventorWare simulation of the same structure are shown in Fig. (3.19). The stopper in this case has the same height as the contact bump and is placed 100μm from the left end of the bottom electrode. Table (3.4) summarizes the comparison between the model and CoventorWare results. The obtained contact force is around 0.85mN which is more than 20% higher than the maximum value obtained at the same peak electric field before introducing the stopper to the structure.

In this case, the numerical solution algorithm has to find the values of the contact force and stopper reaction which simultaneously satisfy the two boundary conditions at the contact and stopper bumps. The algorithm developed to handle this situation is presented in Fig. (3.20). BC1 represents the boundary condition at the contact bump and BC2 represents the boundary condition at the stopper bump. The initial beam deflection curve can be taken as a null array or as the profile in Fig. (3.12).

3.3. APPLYING THE SEMI-ANALYTICAL MODEL TO BRIDGE PROBLEMS

Considering fixed-fixed type beams, or bridges, which are symmetrically double the structures in Fig. (3.3, 3.16), mirrored at the free ends. The analysis of the problem is made simpler by its symmetry. Only the half-structures shown in Fig. (3.3, 3.16) need to be analyzed with an additional symmetry boundary condition at the free ends.

For deeper understanding of the problem, it is noticeable in the bridge case that there are four anchor reactions, two moments and two forces, against only one moment and one force in the cantilever problem. Due to symmetry, the two force reactions are equal, and each of them is equal to half the net external load on the beam according to the vertical force equilibrium equation. The two moment reactions are also equal, but

the value of each is not determinate from the moment equilibrium equation. The reason is that if we try to apply the moment equilibrium equation at any point, we find that the two moment reactions are acting equally in magnitude and oppositely in direction, and thus cancel each other from the equation.

In conclusion, the bridge problem involves one higher degree of indeterminacy than the cantilever problem. This higher indeterminacy is substituted by adding an unknown moment which substitutes for the unknown anchor moment reactions. The resulting free body diagrams of the half-bridge structures are shown in Fig. (3.21). The additional boundary condition to be satisfied is the symmetry boundary condition implying a null slope for the deflection curve at the symmetry plane, i.e. at $x = l$ [32]. The procedure to analyze the bridge problem is similar to the cantilever problem, given that the only difference in the free body diagrams of both cases is the presence of the additional unknown moment M_C in the bridge case. Applying the same procedures as before, the beam deflection differential equation for the bridge problem before pull-in becomes

$$\frac{d^2u_{(x)}}{dx^2} = \begin{cases} \dfrac{6\varepsilon_0 V^2 w_2}{E w_1 t_1^3}\left(x\int_{x_{e1}}^{x_{e2}} \dfrac{d\hat{x}}{\left[d_0 + u_{(\hat{x})}\right]^2} - \int_{x_{e1}}^{x_{e2}} \dfrac{\hat{x}d\hat{x}}{\left[d_0 + u_{(\hat{x})}\right]^2} \right) - \dfrac{12M_C}{E w_1 t_1^3} & ; 0 < x < x_{e1} \\ \dfrac{6\varepsilon_0 V^2}{E t_2^3}\left(x\int_{x_{e1}}^{x_{e2}} \dfrac{d\hat{x}}{\left[d_0 + u_{(\hat{x})}\right]^2} - \int_{x_{e1}}^{x_{e2}} \dfrac{\hat{x}d\hat{x}}{\left[d_0 + u_{(\hat{x})}\right]^2} - \int_{x_{e1}}^{x} \dfrac{(x-\hat{x})d\hat{x}}{\left[d_0 + u_{(\hat{x})}\right]^2} \right) & ; x_{e1} < x < x_{e2} \\ \qquad\qquad - \dfrac{12M_C}{E w_2 t_2^3} & \\ -\dfrac{12M_C}{E w_3 t_2^3} & ; x_{e2} < x < l \end{cases} \tag{3.19}$$

The numerical algorithm to solve Eq. (3.19) is much similar to the algorithm presented in Fig. (3.11) by exchanging the contact force with M_C as the parameter under numerical search, and exchanging the contact tip boundary condition with a zero slope for the deflection curve at $x = l$.

After first pull-in, the beam deflection equation becomes

$$\frac{d^2 u_{(x)}}{dx^2} = \begin{cases} \dfrac{6\varepsilon_0 V^2 w_2}{E w_1 t_1^3}\left(x\int_{x_{e1}}^{x_{e2}} \dfrac{d\hat{x}}{\left[d_0 + u_{(\hat{x})}\right]^2} - \int_{x_{e1}}^{x_{e2}} \dfrac{\hat{x} d\hat{x}}{\left[d_0 + u_{(\hat{x})}\right]^2} \right) & \\ \qquad + \dfrac{12}{E w_1 t_1^3}\left[F_C (l - x) - M_C \right] & ; 0 < x < x_{e1} \\ \dfrac{6\varepsilon_0 V^2}{E t_2^3}\left(x\int_{x_{e1}}^{x_{e2}} \dfrac{d\hat{x}}{\left[d_0 + u_{(\hat{x})}\right]^2} - \int_{x_{e1}}^{x_{e2}} \dfrac{\hat{x} d\hat{x}}{\left[d_0 + u_{(\hat{x})}\right]^2} - \int_{x_{e1}}^{x} \dfrac{(x - \hat{x}) d\hat{x}}{\left[d_0 + u_{(\hat{x})}\right]^2} \right) & \\ \qquad + \dfrac{12}{E w_2 t_2^3}\left[F_C (l - x) - M_C \right] & ; x_{e1} < x < x_{e2} \\ \dfrac{12}{E w_3 t_2^3}\left[F_C (l - x) - M_C \right] & ; x_{e2} < x < l \end{cases} \tag{3.20}$$

Similarly, after second pull-in the beam deflection equation becomes

$$\frac{d^2u_{(x)}}{dx^2}=\begin{cases}\dfrac{6\varepsilon_0V^2w_2}{Ew_1t_1^3}\left(x\displaystyle\int_{x_{e1}}^{x_{e2}}\frac{d\hat{x}}{\left[d_0+u_{(\hat{x})}\right]^2}-\int_{x_{e1}}^{x_{e2}}\frac{\hat{x}d\hat{x}}{\left[d_0+u_{(\hat{x})}\right]^2}\right) & ;0<x<x_{e1}\\ \qquad+\dfrac{12}{Ew_1t_1^3}\left[F_C\left(l-x\right)+R\left(x_s-x\right)-M_C\right] & \\ \dfrac{6\varepsilon_0V^2}{Et_2^3}\left(x\displaystyle\int_{x_{e1}}^{x_{e2}}\frac{d\hat{x}}{\left[d_0+u_{(\hat{x})}\right]^2}-\int_{x_{e1}}^{x_{e2}}\frac{\hat{x}d\hat{x}}{\left[d_0+u_{(\hat{x})}\right]^2}-\int_{x_{e1}}^{x}\frac{\left(x-\hat{x}\right)d\hat{x}}{\left[d_0+u_{(\hat{x})}\right]^2}\right) & ;x_{e1}<x<x_s\\ \qquad+\dfrac{12}{Ew_2t_2^3}\left[F_C\left(l-x\right)+R\left(x_s-x\right)-M_C\right] & \\ \dfrac{6\varepsilon_0V^2}{Et_2^3}\left(x\displaystyle\int_{x_{e1}}^{x_{e2}}\frac{d\hat{x}}{\left[d_0+u_{(\hat{x})}\right]^2}-\int_{x_{e1}}^{x_{e2}}\frac{\hat{x}d\hat{x}}{\left[d_0+u_{(\hat{x})}\right]^2}-\int_{x_{e1}}^{x}\frac{\left(x-\hat{x}\right)d\hat{x}}{\left[d_0+u_{(\hat{x})}\right]^2}\right) & ;x_s<x<x_{e2}\\ \qquad+\dfrac{12}{Ew_2t_2^3}\left[F_C\left(l-x\right)-M_C\right] & \\ \dfrac{12}{Ew_3t_2^3}\left[F_C\left(l-x\right)-M_C\right] & ;x_{e2}<x<l\end{cases} \tag{3.21}$$

Considering the bridge version of sample structure number (3) which is illustrated in Table (3.3), the bridge model results are compared to CoventorWare simulation in Fig. (3.22). Both the semi-analytical and finite element solutions are performed using a symmetry boundary condition at the cantilever free end to represent the bridge.

The structure analyzed in Fig. (3.22) has almost the same geometry as sample structure number (1) which has been analyzed using the simplified analytical model in Section (3.1). Table (3.5) summarizes a comparison between the results obtained using the three techniques and the respective errors considering the finite element simulation as a reference.

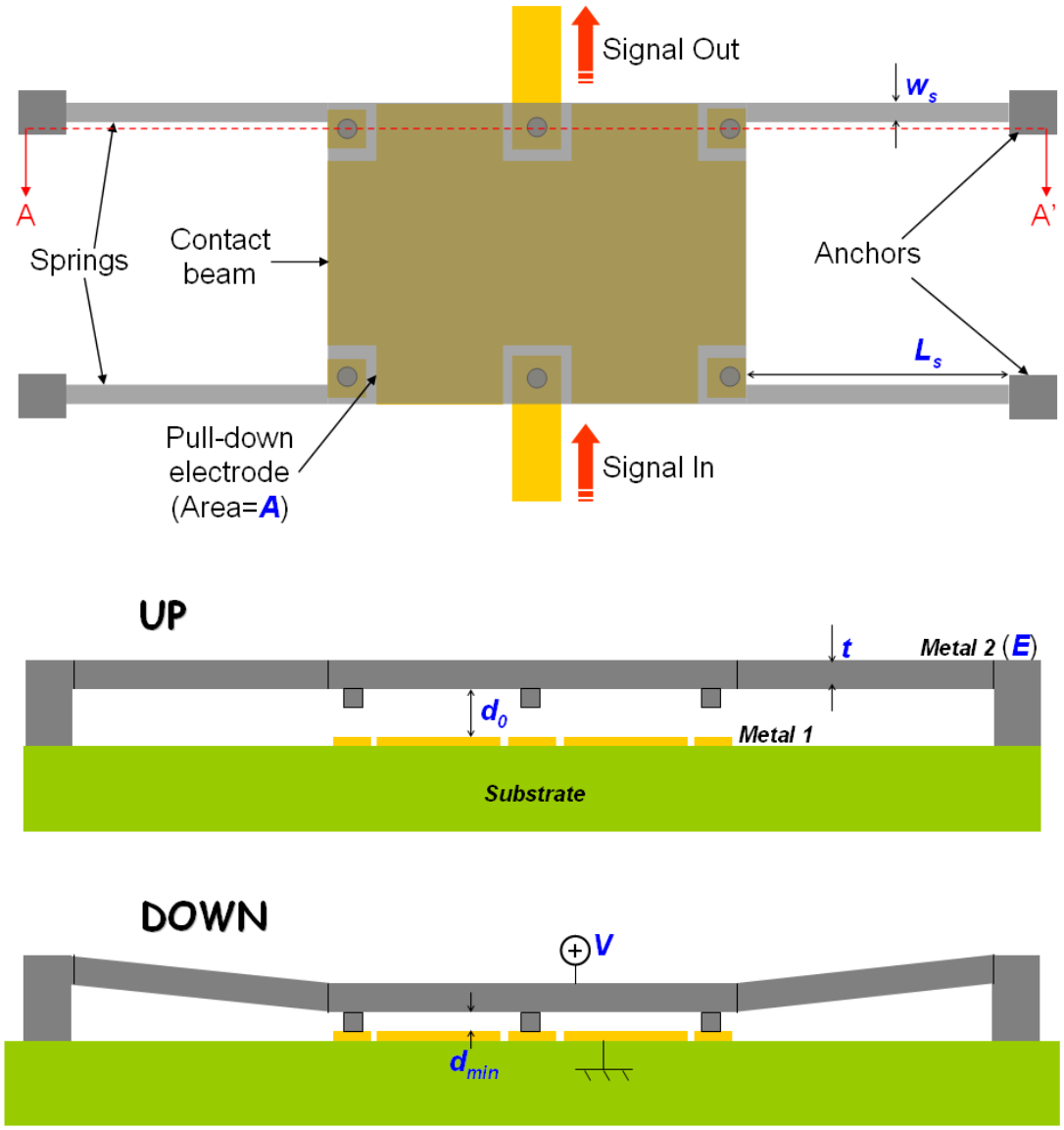

Figure 3.1. Structure of fixed-fixed flexures contact switch. A top view and two cross-sectional views are shown

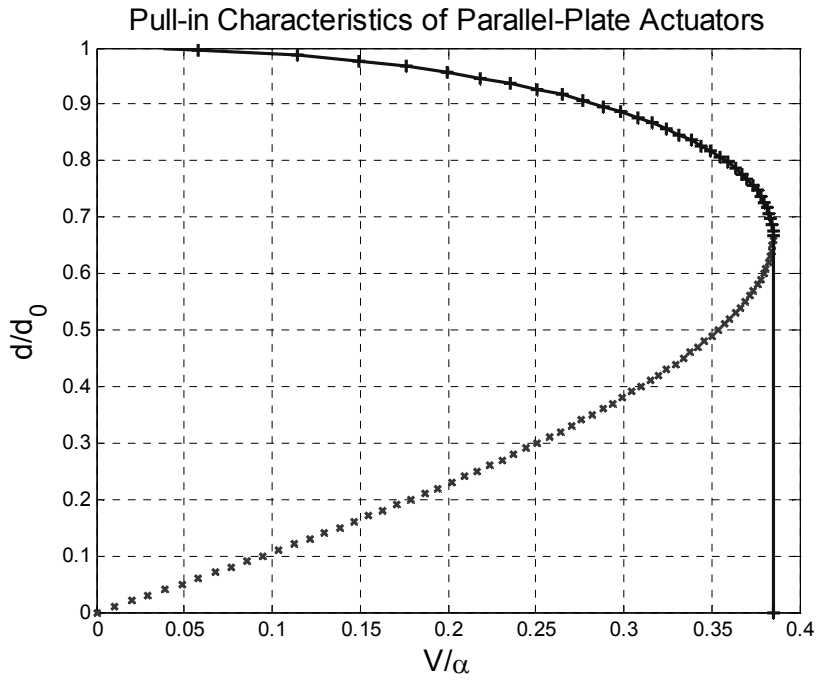

Figure 3.2. Pull-in of electrostatic actuators. A plot of the dimensionless relationship between actuation voltage and gap height indicating the occurrence of pull-in at 2/3 of the initial gap height.

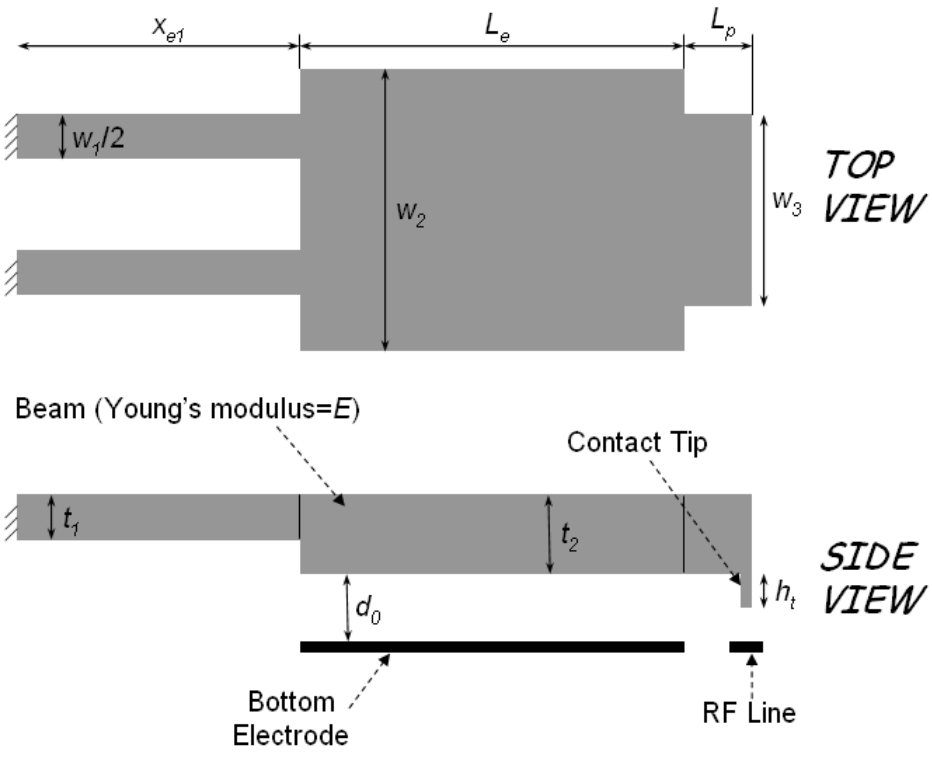

Figure 3.3. The general cantilever beam structure for the semi-analytical model.

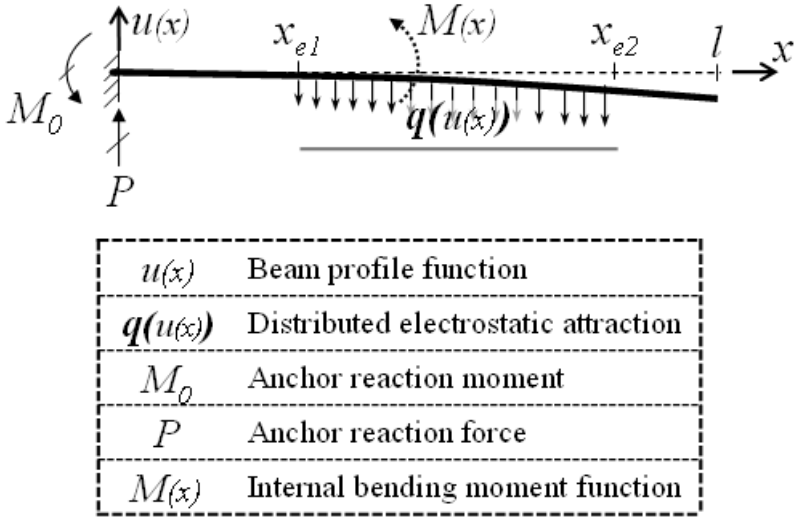

Figure 3.4. Free body diagram of the cantilever beam structure before pull-in.

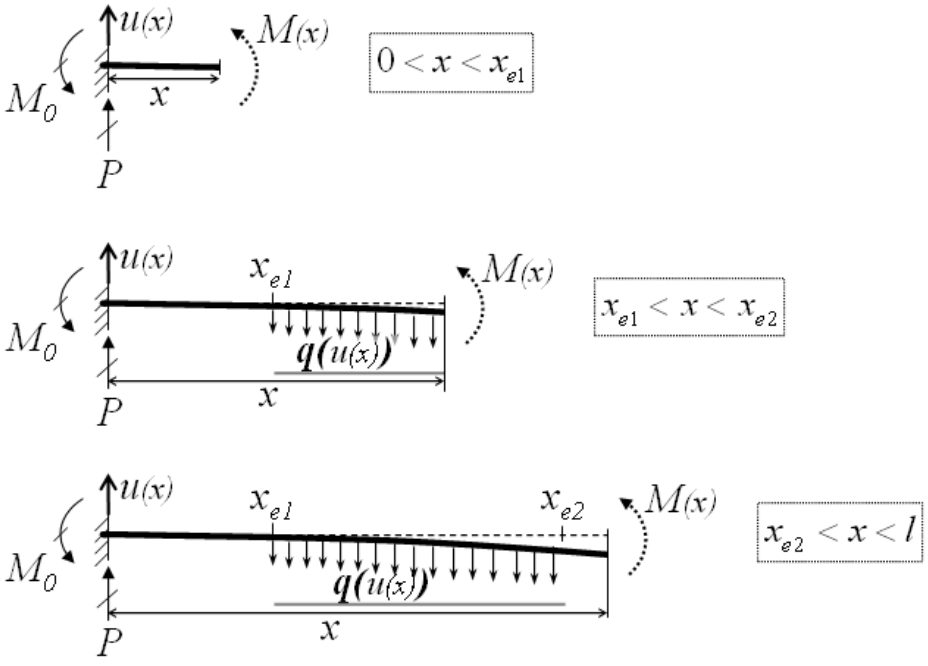

Figure 3.5. Bending moment calculation diagrams for a cantilever before pull-in and after first pull-in.

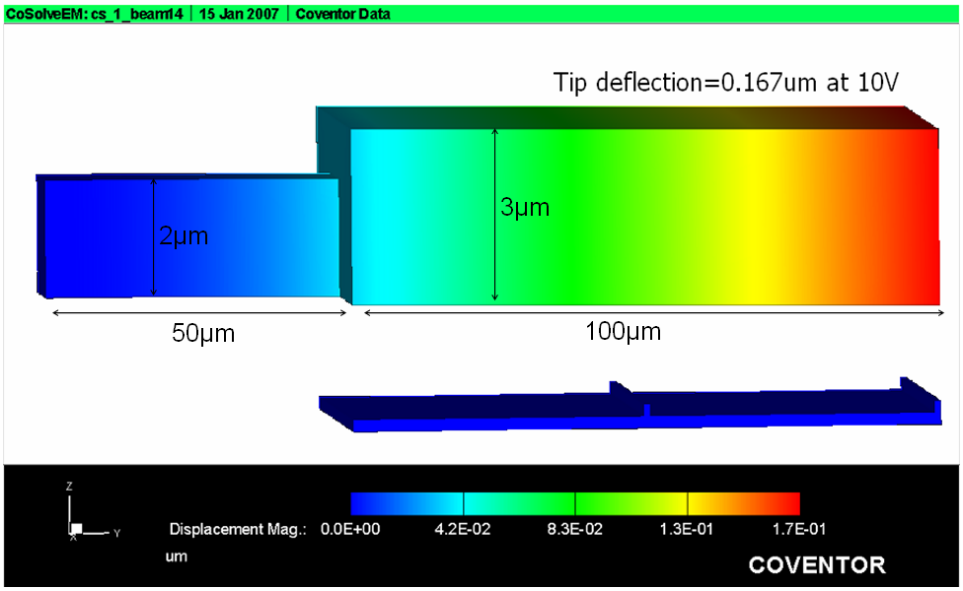

(a)

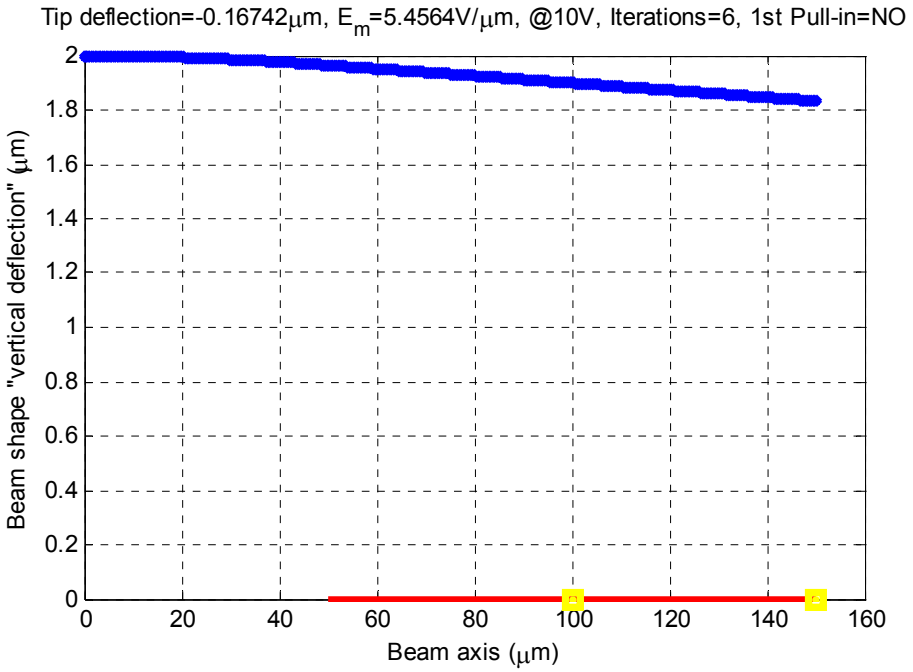

(b)

Figure 3.6. Comparing the results of CoventorWare simulation (a) and the semi-analytical model (b) for sample structure number (2) at 10V. An error of less than 0.3% in the tip deflection is observed.

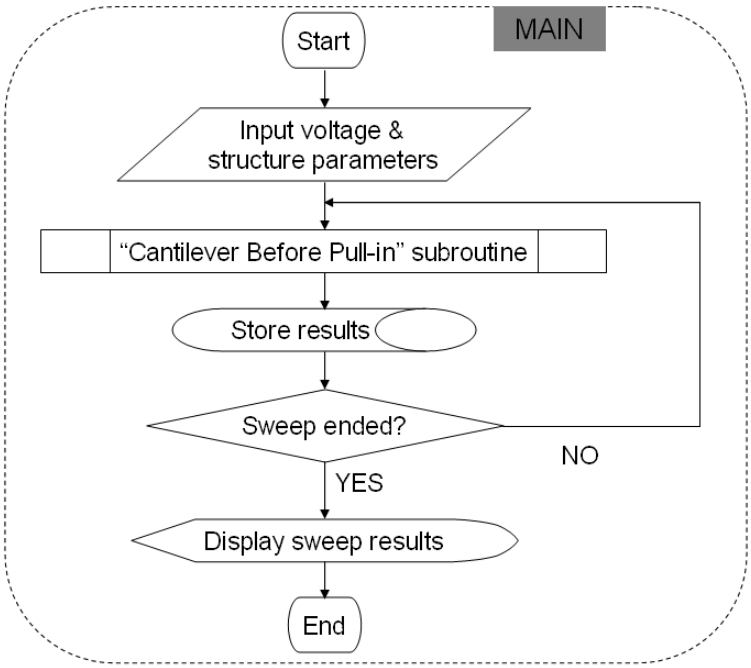

(a)

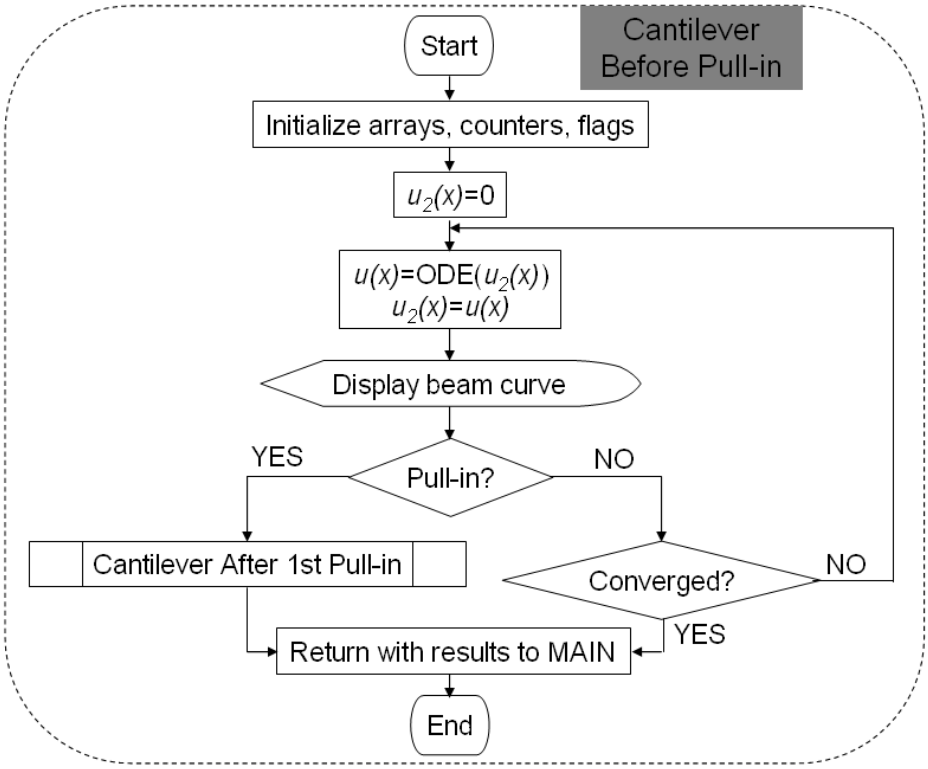

(b)

Figure 3.7. Flowcharts of the main program (a) and the subroutine for solving a cantilever problem before pull-in (b).

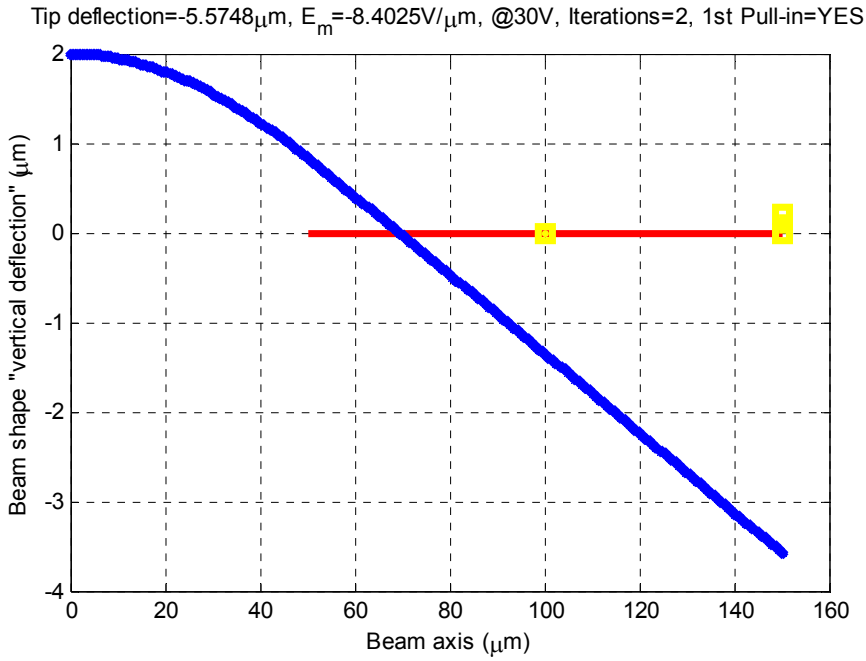

Figure 3.8. Pull-in detected for sample structure number (2) at 30V. The solution diverges and the beam passes through the bottom electrode shown as a red line.

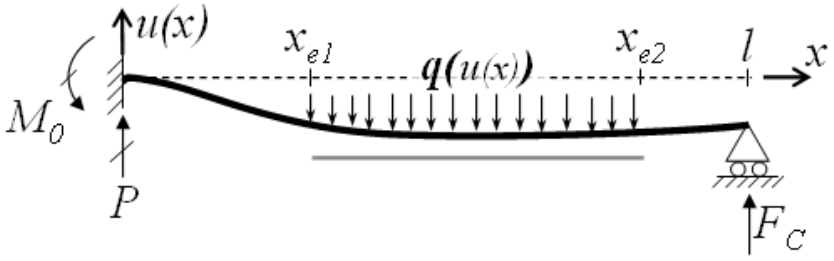

Figure 3.9. Free body diagram of the cantilever beam after first pull-in.

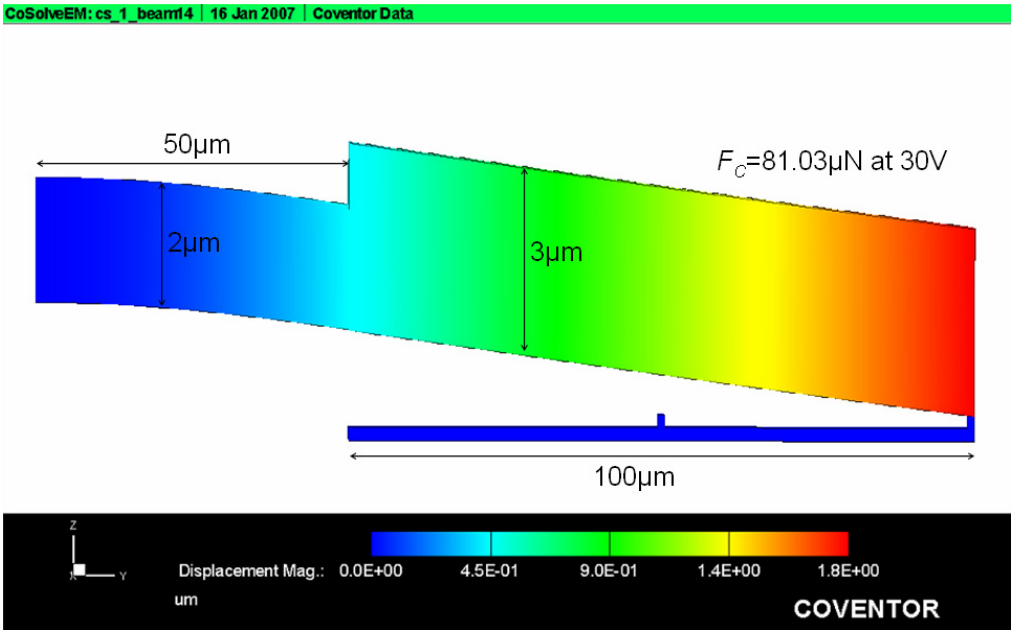

(a)

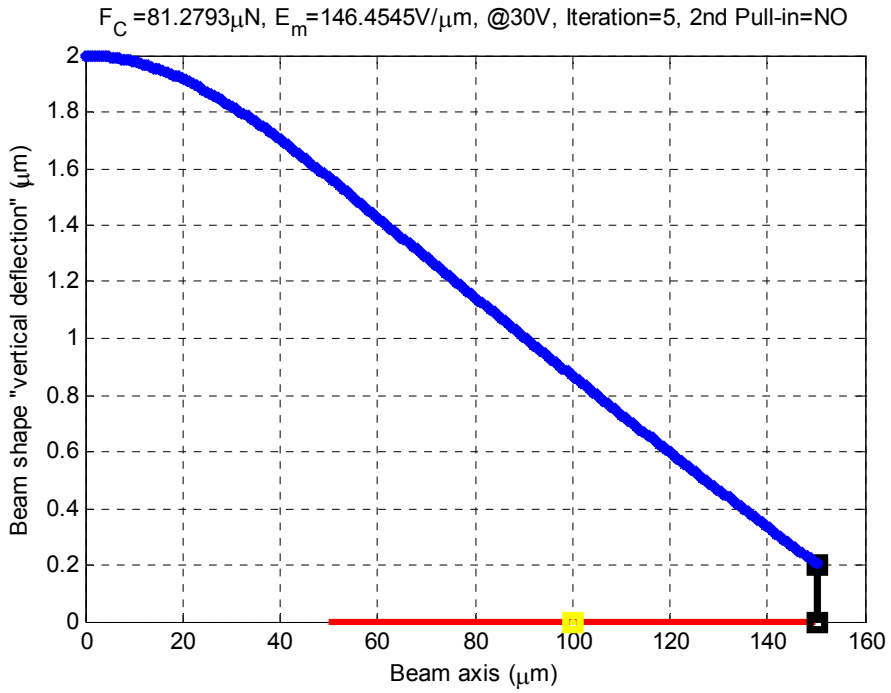

(b)

Figure 3.10. Comparing the results of CoventorWare simulation (a) and the semi-analytical model (b) for sample structure number (2) at 30V. An error of less than 0.4% in calculating the contact force is observed.

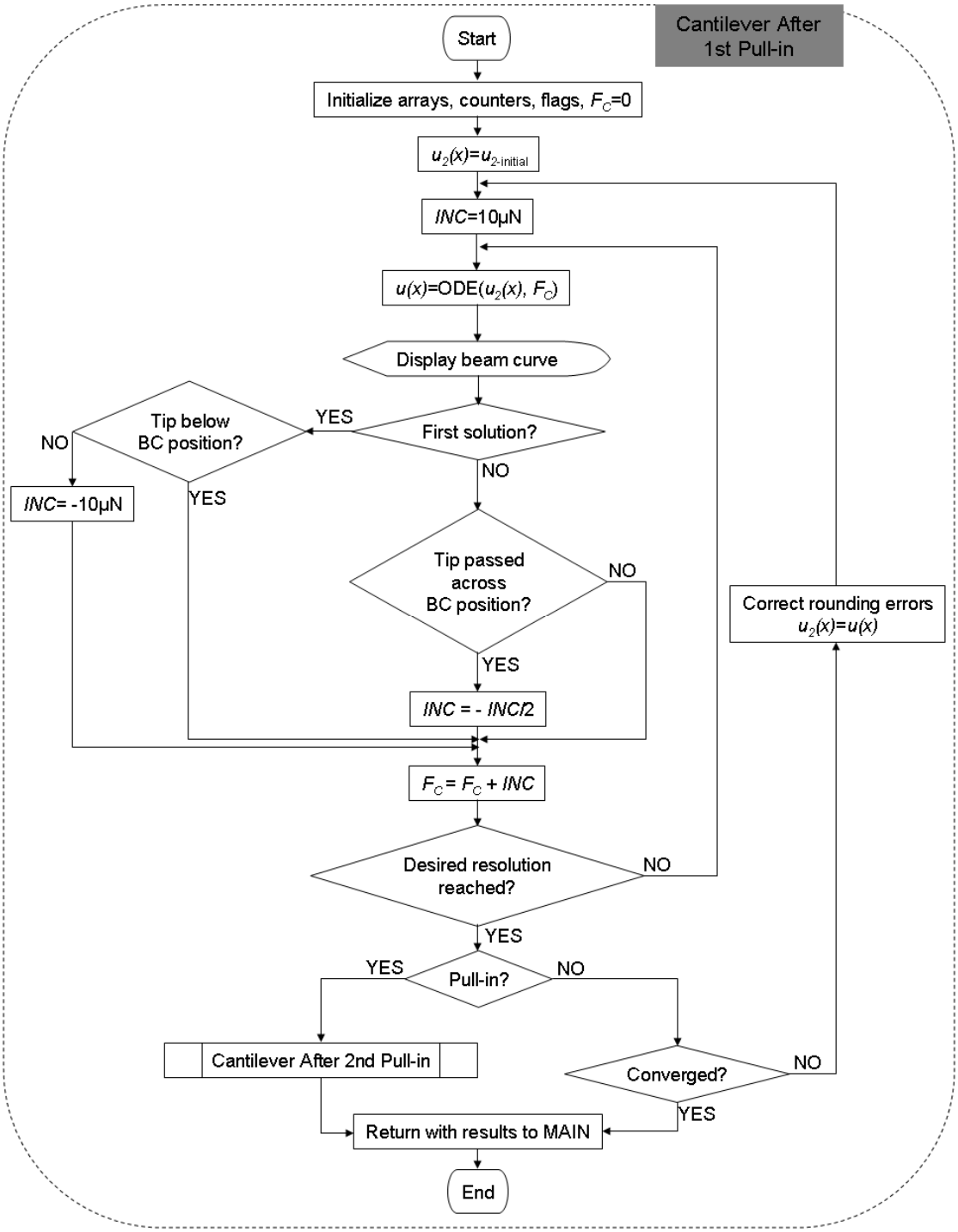

Figure 3.11. A flowchart developed to implement the semi-analytical model solution after first pull-in.

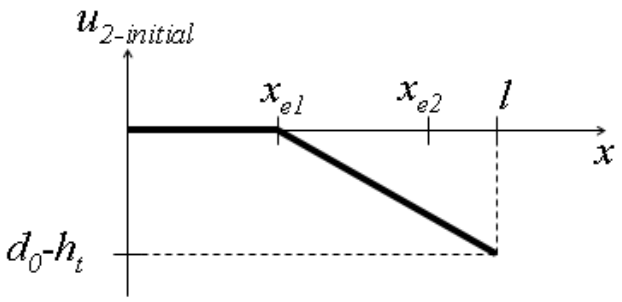

Figure 3.12. Initial deflection curve used for cantilever beam model after first pull-in.

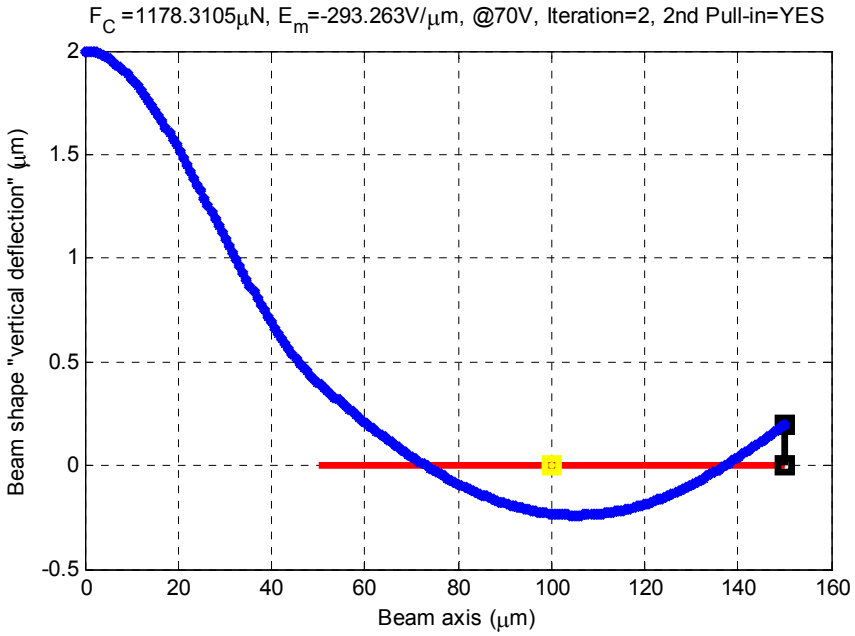

Figure 3.13. Second pull-in of sample structure number (2) observed at 70V.

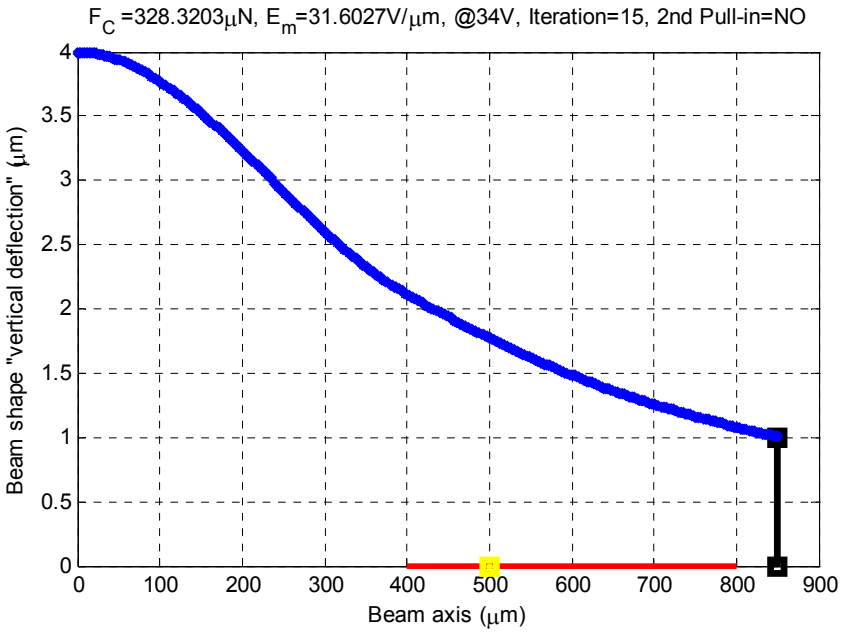

(a)

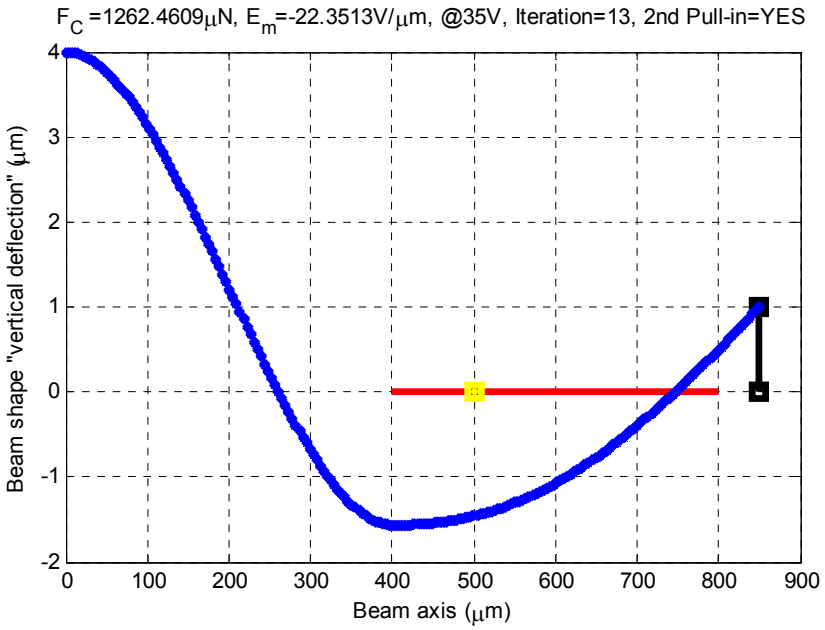

(b)

Figure 3.14. Maximum contact force of 0.328mN obtained for sample structure number (3) at 34V (a) before second pull-in occurs at 35V (b).

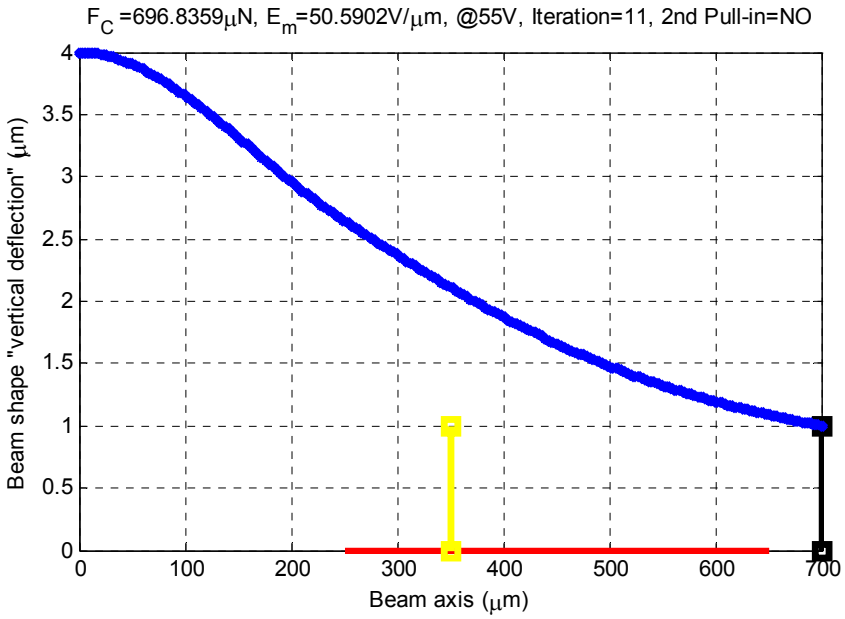

Figure 3.15. Modified sample structure number (3), giving 0.697mN contact force at 55V.

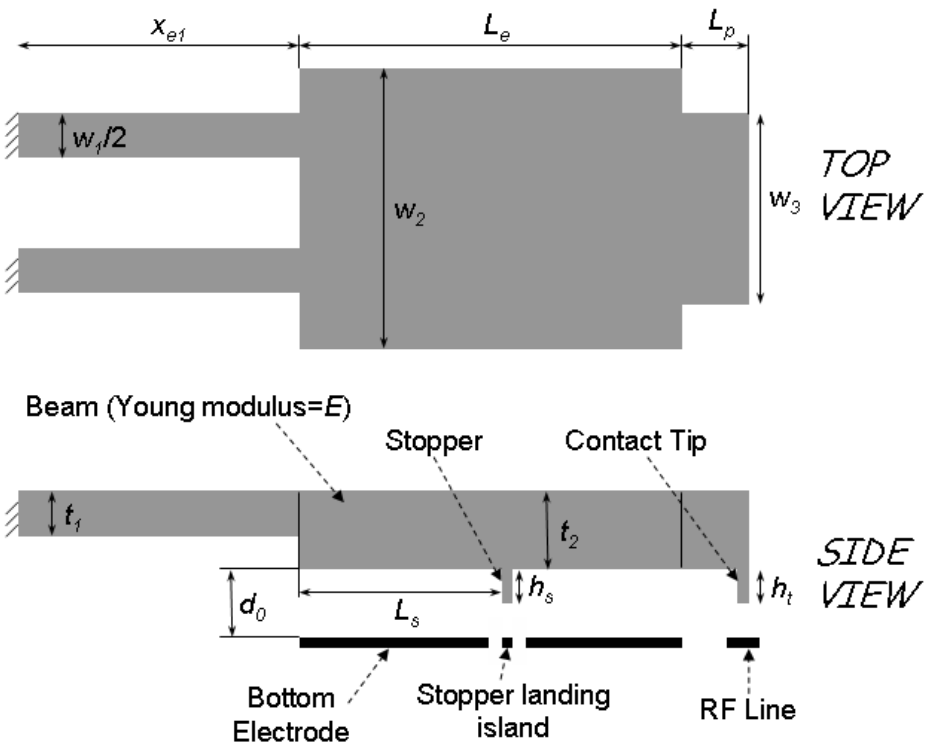

Figure 3.16. The modified cantilever structure, including a stopper to enhance the stability of the beam.

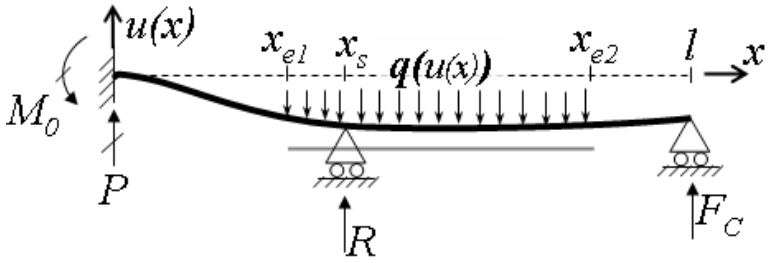

Figure 3.17. Free body diagram of the cantilever beam structure after second pull-in.

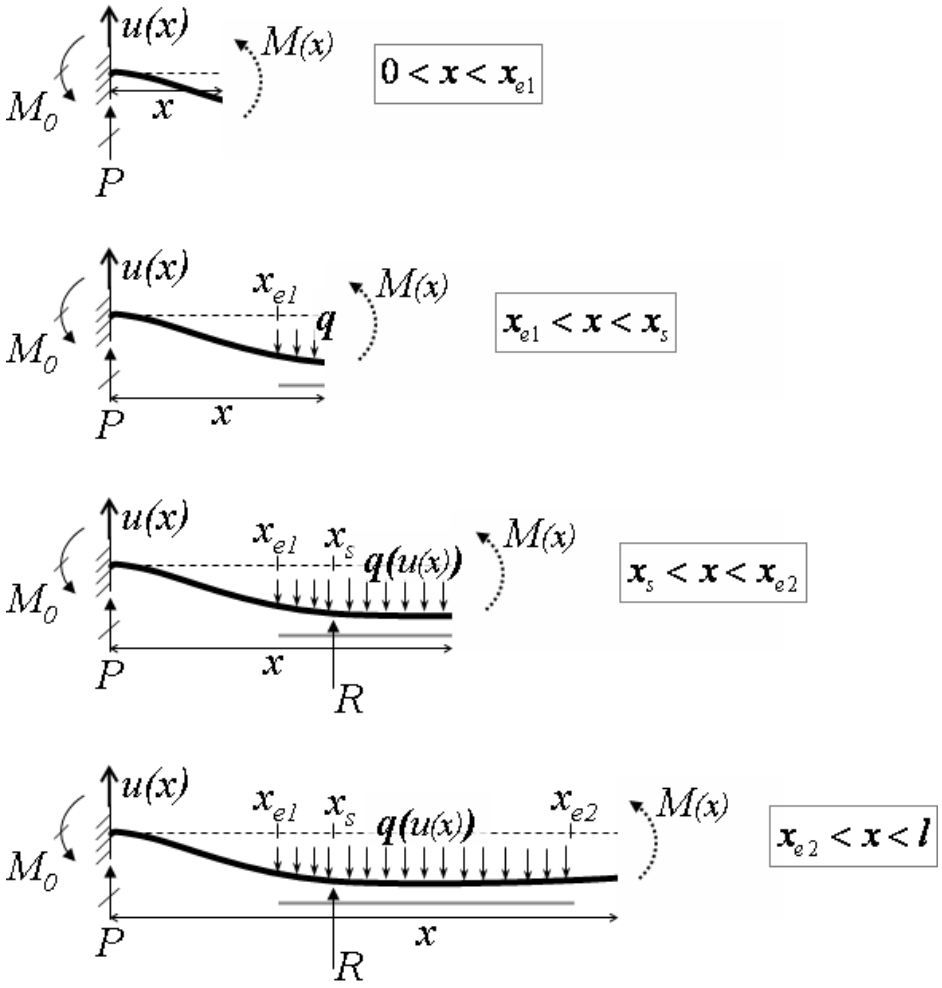

Figure 3.18. Bending moment calculation diagrams for a cantilever after second pull-in.

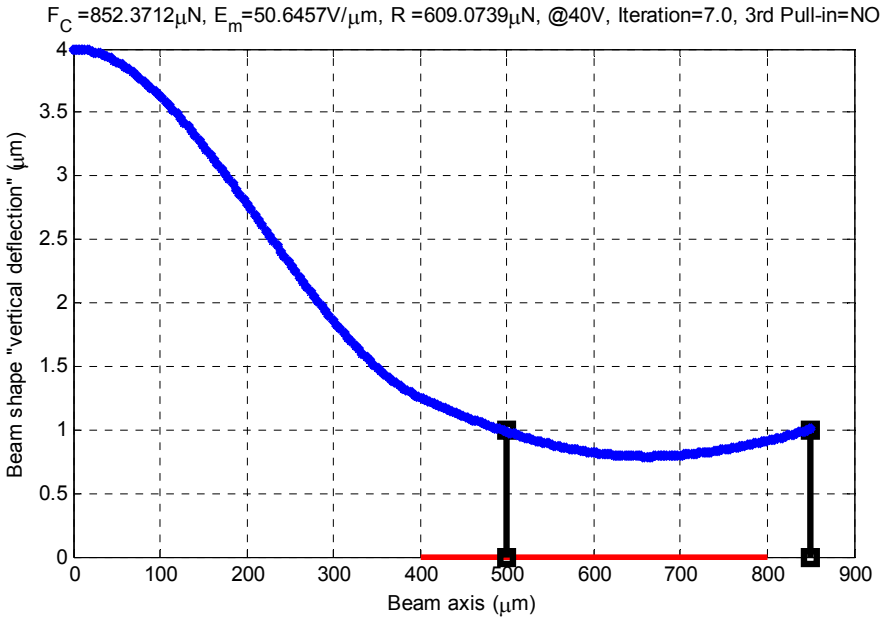

(a)

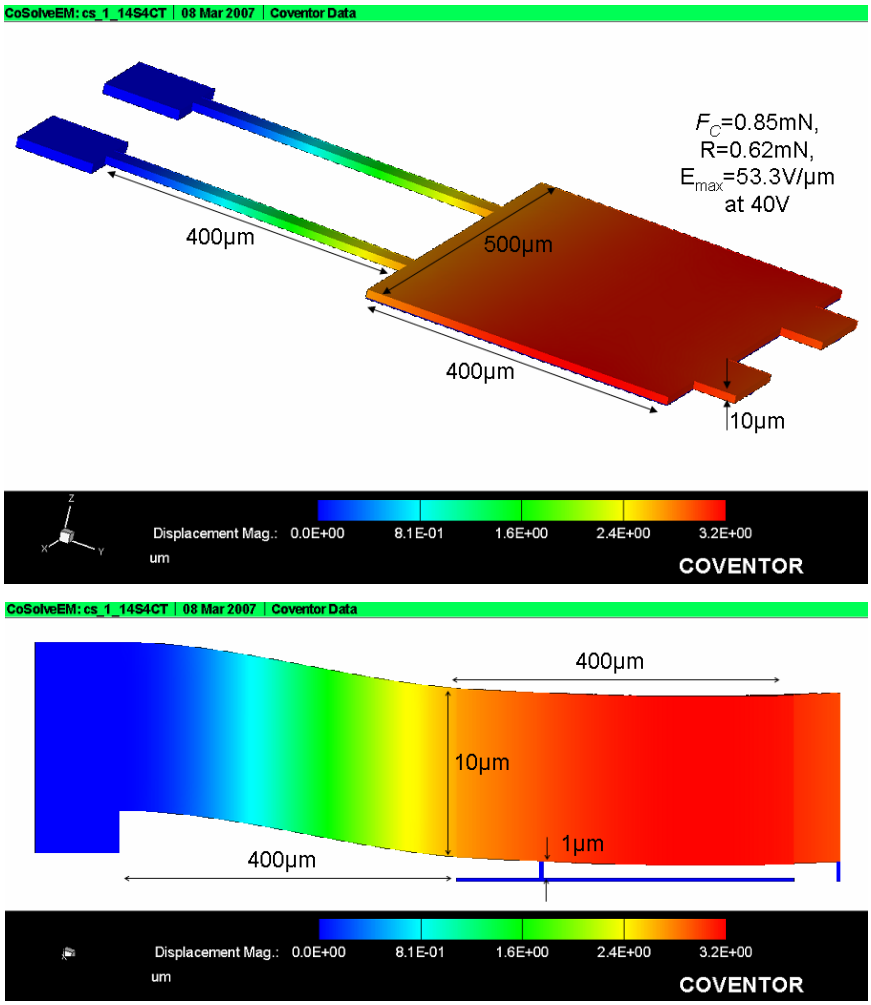

(b)

Figure 3.19. The model (a) and CoventorWare (b) results for sample structure number (3) at 40V.

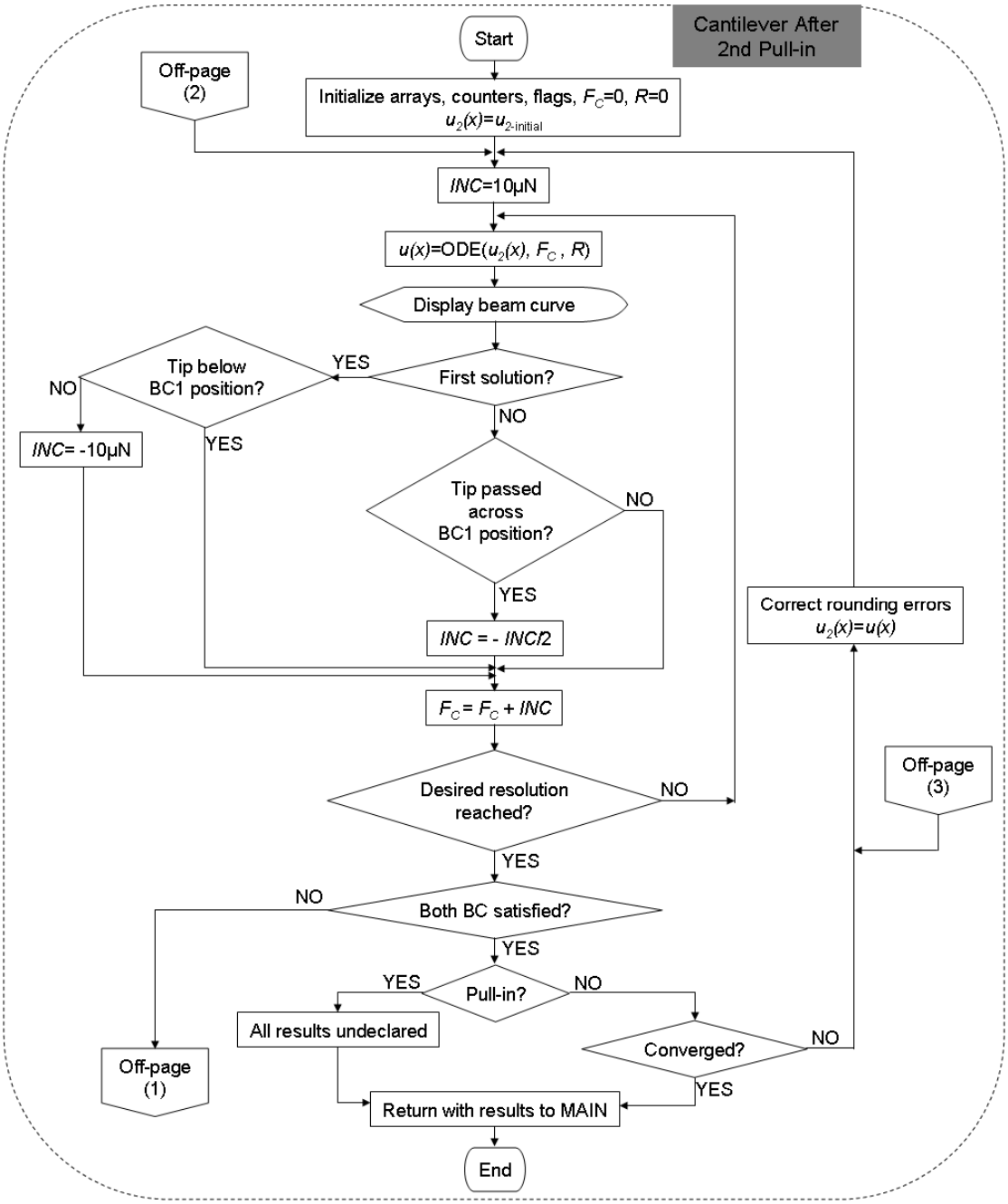
Cantilever After 2nd Pull-in
Start
Off-page (2)
Initialize arrays, counters, flags, F_C=0, R=0
$u_2(x)=u_{2\text{-initial}}$
INC=10μN
$u(x)$=ODE($u_2(x)$, F_C , R)
Display beam curve
First solution?
YES
NO
Tip below BC1 position?
NO
YES
INC= -10μN
Tip passed across BC1 position?
NO
YES
INC = - INC/2
$F_C = F_C + INC$
Desired resolution reached?
NO
YES
Correct rounding errors
$u_2(x)=u(x)$
Off-page (3)
Both BC satisfied?
NO
YES
Pull-in?
YES
NO
All results undeclared
Converged?
NO
YES
Off-page (1)
Return with results to MAIN
End

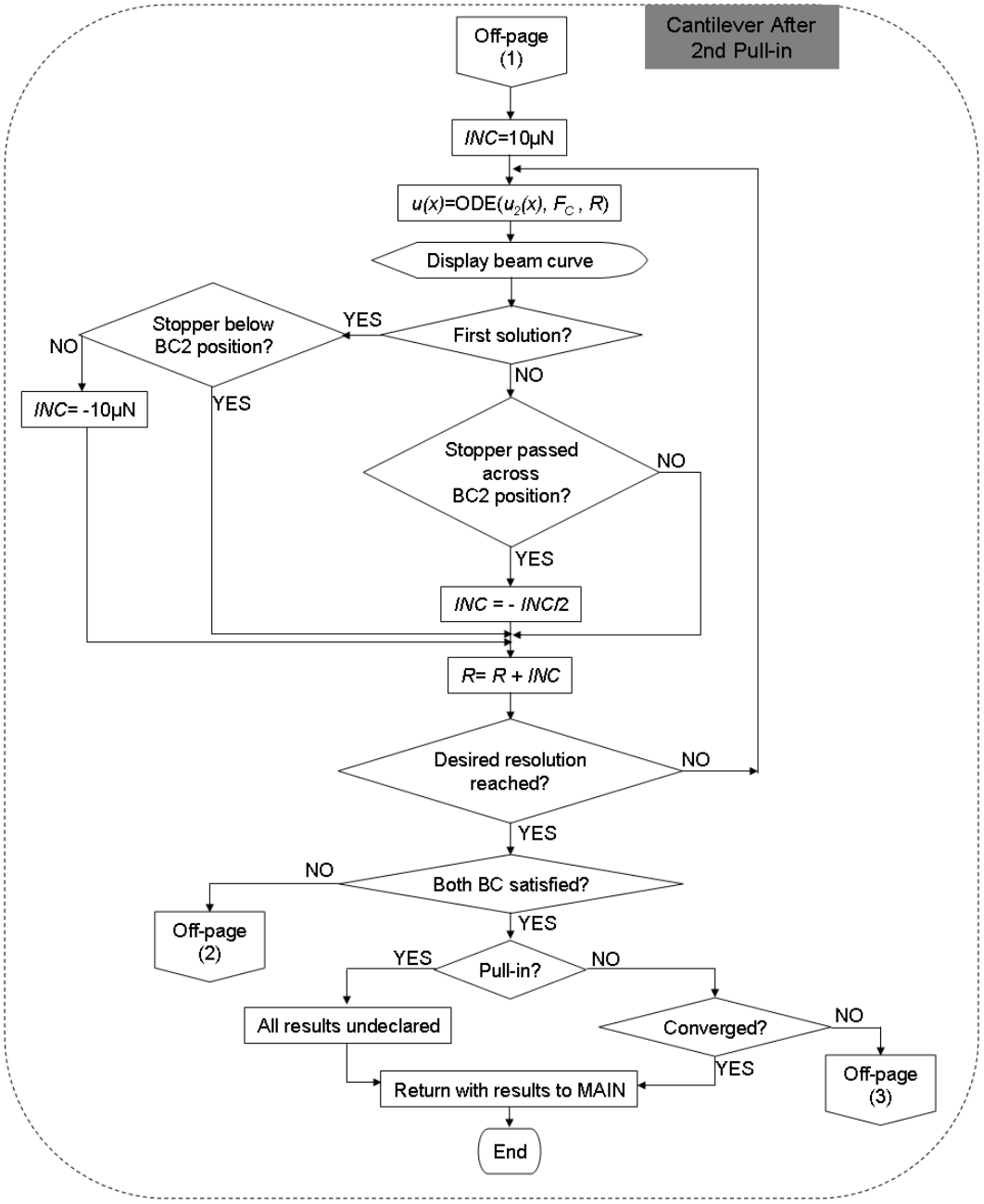

Figure 3.20. A flowchart developed to implement the semi-analytical model solution after second pull-in. The flowchart is divided into two pages for size limitations.

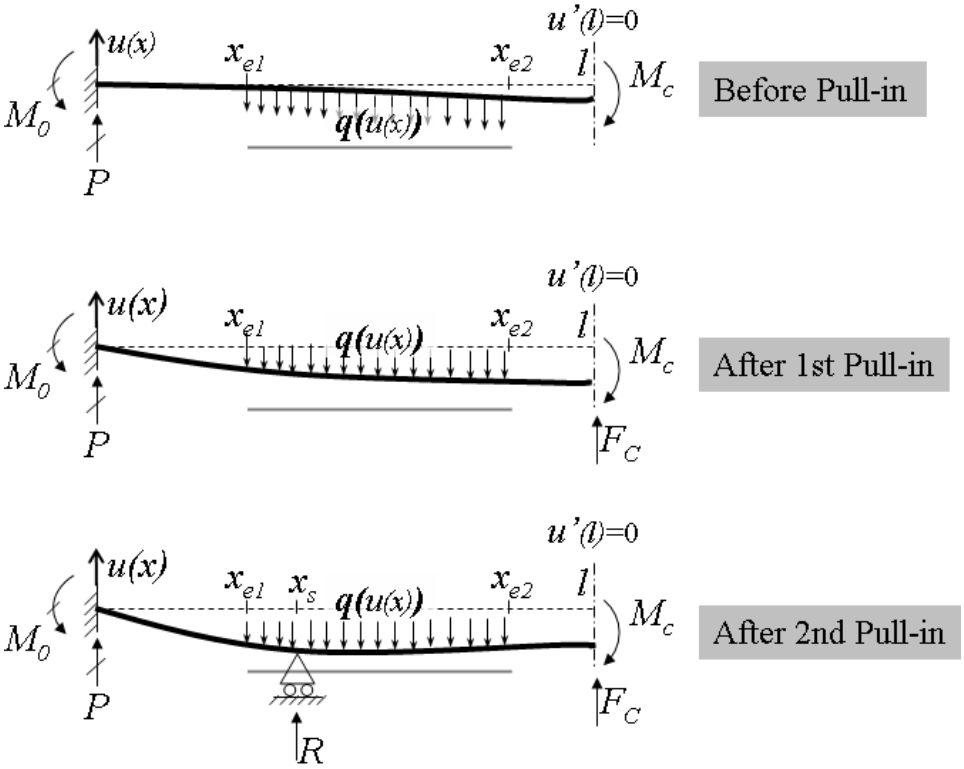

Figure 3.21. Free body diagrams for the bridge problem. An unknown moment M_c is introduced. Symmetry boundary condition is expressed by a null deflection curve slope at the symmetry plane.

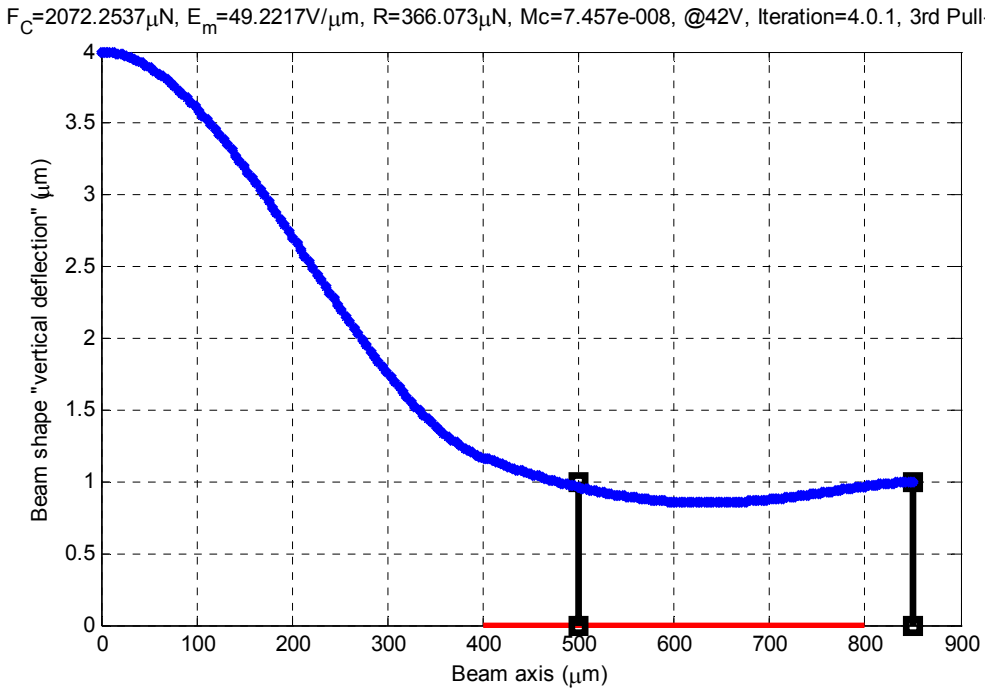

(a)

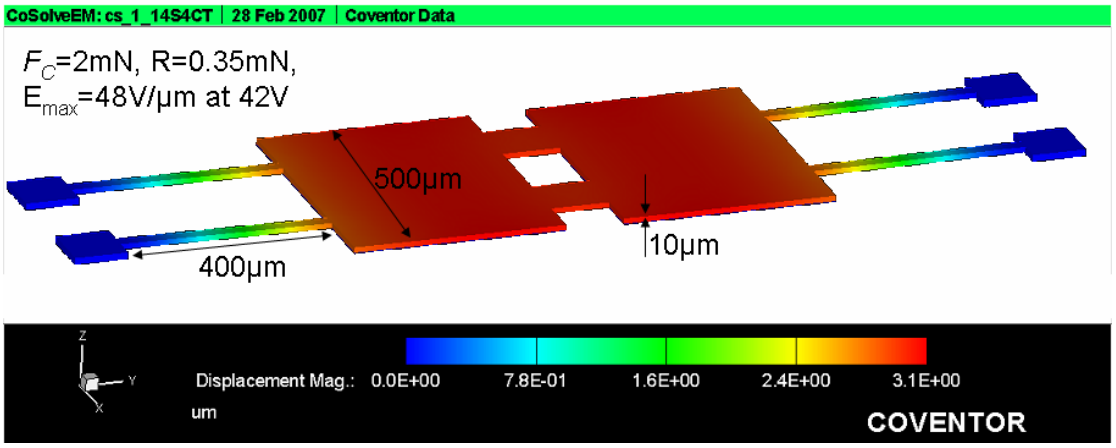

(b)

Figure 3.22. The bridge model results (a) and CoventorWare simulation of the bridge version of sample structure number (3).

Parameter	Description	Value	Unit
A	Actuator area	500x800	$(\mu m)^2$
E	Metal elasticity modulus	180	GPa
t	Spring thickness	10	µm
w_s	Spring width	25	µm
L_s	Spring length	400	µm
d_0	Initial gap height	4	µm
$d_{\min}$	Minimum gap height	1	µm

Table 3.1. Parameters of sample structure number (1) for the simplified analytical model. Parameters are visualized in Fig. (3.1).

Parameter	Description	Value	Unit
x_{e1}	Length of spring	50	µm
L_e	Length of electrodes	100	µm
L_p	Length of passive extension	0	µm
w_1	Spring width	20	µm
w_2	Electrodes width	80	µm
w_3	Passive extension width	80	µm
t_1	Spring thickness	2	µm
t_2	Plate thickness	3	µm
d_0	Initial gap height	2	µm
h_t	Contact bump height	0.2	µm
E	Beam material elasticity	220.5	GPa

Table 3.2. Parameters of sample structure number (2) for the semi-analytical model of a cantilever structure. Parameters are visualized in Fig. (3.3).

Parameter	Description	Value	Unit
x_{e1}	Length of spring	400	µm
L_e	Length of electrodes	400	µm
L_p	Length of passive extension	50	µm
w_1	Spring width	50	µm
w_2	Electrodes width	500	µm
w_3	Passive extension width	200	µm
t_1	Spring thickness	10	µm
t_2	Plate thickness	10	µm
d_0	Initial gap height	4	µm
h_t	Contact bump height	1	µm
E	Beam material elasticity	180	GPa

Table 3.3. Parameters of sample structure number (3) for the semi-analytical model of a cantilever structure. Parameters are visualized in Fig. (3.3).

	CoventorWare	Model	Error
Contact force	0.85 mN	0.85 mN	0 %
Stopper reaction	0.62 mN	0.61 mN	-1.6 %
Peak electric field	53.3 V/µm	50.6 V/µm	-5 %
PC simulation time	40-60 seconds	2-3 hours	-----

Table 3.4. Comparing the semi-analytical model results to CoventorWare results for sample structure number (3) at 40V.

		CoventorWare	Semi-analytical model	Simplified model
Contact force	Value	2 mN	2.07 mN	0.76 mN
	Error	0 %	3.5 %	-62 %
Stopper reaction	Value	0.35 mN	0.37 mN	0.76 mN
	Error	0 %	5.7 %	117 %
Peak electric field	Value	48 V/μm	49.2 V/μm	42 V/μm
	Error	0 %	2.5 %	-12.5 %
PC simulation time		3-4 hours	2-3 minutes	0.1 sec

Table 3.5. Comparing the semi-analytical model and simplified model results to CoventorWare results for the bridge version of sample structure number (3) at 42V.

CHAPTER 4

DESIGN AND TECHNOLOGY OF HIGH FORCE RFMEMS CONTACT SWITCHES

The development of the relatively fast and accurate model presented in Chapter 3 is of significant value to the design process of high force RFMEMS switches. The model quickly provides the results of sweeping any of the design parameters, and thus promotes making quick and optimal design decisions. The model also predicts the optimum operating voltage for a specific design, which produces the highest contact force, given that the peak electric field is below the breakdown field. Furthermore, the model enables investigating the effect of possible deviations in the technological process outcomes or operating conditions.

In this chapter, design issues will be discussed based on the model results. Moreover, full 3D finite element simulations for the final designs will be presented. The overall performance of the final designs will also be discussed. Finally, the fabrication technology for the presented designs will be explained together with test structures designed to determine the technology-dependent characteristics of the fabricated devices.

4.1. DESIGN CONSIDERATIONS

The design parameters of the problem in hand are the geometrical dimensions presented in Fig. (3.16), in addition to the beam material which determines the modulus of elasticity needed for the model calculations.

The geometrical parameters in Fig. (3.16) are, however, not totally independent in their effect on the obtained contact force. For instance, the flexural rigidity of the

suspension spring is proportional to the product of its width (w_1) and the cube of its thickness (t_1^3), which means that increasing the spring thickness and decreasing its width by certain amounts can yield the same behavior. An efficient design procedure for a high force device should make use of such relations among the switch structural parameters.

Moreover, the effect of certain parameters on the obtained contact force is roughly predetermined, like the direct effect of the electrostatic actuator area ($A = w_2 \times L_e$), which is the area of the middle section of the beam, on the contact force as predicted by Eq. (2.1).

Another consideration for the design process is the simplicity of the fabrication process of the obtained design. Presenting a high force device which requires the least complicated fabrication process is an important aspect of this work. The simplicity of the fabrication processes is achieved when the vertical variations in the structure are limited. For instance, giving the same thickness to the two sections of the beam ($t_1 = t_2$) eliminates an extra mask and extra processing steps that would have been needed to differentiate between the lower and higher thickness regions. This constraint does not reduce the design flexibility of the structure, because of the redundancy of some of the parameters as discussed before. From another point of view, increasing the thickness of the beam is preferred to enhance its rigidity against any collapse due to the high electrostatic attraction to the bottom electrode.

Further technology simplification can be achieved by assigning the same value to the heights of the contact and stopper bumps. This enables defining both features in a single fabrication process rather than two. It may be argued that this new constraint limits the design flexibility of the structure. However, Fig. (4.1) shows the model results for different stopper bump heights and positions for sample structure number

(3) illustrated in Table (3.3). The results show that there is a different stopper position which provides approximately the same peak contact force for different stopper heights. It is worth mentioning that lower stopper position values would yield higher contact force values, but only at peak electric field values which are significantly higher that the recommended upper limit of 50V/μm.

The initial gap height (d_0) has limited effect on the obtained contact force. However, it is a significant performance and robustness enhancement factor. Increasing the initial gap height provides higher isolation between the contact surfaces in the Off state. Moreover, increasing the initial gap height lessens the effect of any undesirable technology-induced deflections in the implemented cantilever or bridge beams. The only drawback of increasing the initial gap height is the increase in the required voltage for the first and second pull-ins, causing a higher peak electric field in the structure after the pull-in events. The peak electric field has to be kept below the recommended upper limit of 50V/μm.

The rightmost section of the beam in Fig. (3.16) is a passive beam section which undergoes no electrostatic attraction, but provides the lateral space needed to isolate the bottom electrode from the signal line. The width (w_3) and length (L_p) of this section are chosen to provide the necessary isolation and keep the overall rigidity of the beam high enough to transfer the electrostatic attraction at the contact tip. The effect of varying the passive section length and width for sample structure number (3) is shown in Fig. (4.2). The curves of the contact force versus the peak electric field are obtained by sweeping the applied voltage on the beam with steps of 2V in the semi-analytical model. The large transitions in the values of the contact force and peak electric field on the curves in Fig. (4.2) represent the occurrence of the second

pull-in. The effect of the width on the obtained results is very small because of the high beam thickness which dominates the rigidity of this section.

On the other hand, the leftmost section of the beam represents the suspension spring. The model treats this section as a single beam of width (w_1), however it is implemented as two narrow beams of width ($w_1/2$) for better mechanical stability of the structure. The width and length of the spring determine the stiffness of the beam suspension. For each combination of the rest of the design parameters, there is an optimum spring stiffness which provides the maximum contact force at the upper limit of the peak electric field. The optimization curves for the spring stiffness for sample structure number (3) are shown in Fig. (4.3). The optimum curve is one with second pull-in occurring shortly before reaching the peak electric field limit of 50V/μm. Shorter spring lengths yield higher spring stiffness causing the second pull-in to occur at higher peak electric field values, and larger spring lengths yield lower spring stiffness causing a lower gain in the contact force during the second pull-in transition.

Finally, the choice of the beam material determines the modulus of elasticity part of the flexural rigidity needed for the model calculations. The beam material chosen in this work is nickel, deposited by electroplating. The main reason for this choice is the availability of a relatively mature technology to deposit thick layers of nickel up to 10μm. The nominal Young's modulus for nickel is 207GPa [30]. However, the actual hardness of the plated layer may deviate from this value. Furthermore, the presence of the release holes in the beam tends to reduce the effective rigidity of the beam. However, the beam thickness can be adjusted to correct the flexural rigidity value despite any deviations in the modulus of elasticity. The effect of varying Young's modulus for sample structure number (3) is shown in Fig. (4.4). A 27% reduction in

Young's modulus caused approximately 10% reduction in the obtained contact force at 50V/μm peak electric field. The large thickness of the beam is the reason of the relative stability of the contact force against elasticity modulus variations.

4.2. COVENTORWARE SIMULATIONS

High force switch structures have been designed using the semi-analytical model presented in Chapter 3, based on the design considerations discussed in the previous section. Further validation and enhancement for the obtained designs has been carried out using the 3D finite element electrostatic/mechanical coupled solver of CoventorWare.

4.2.1. Contact Switch Simulation Procedure

The steps to simulate an electrostatically actuated contact switch and obtain the contact force and peak electric field at a given applied voltage using CoventorWare are summarized in the following list: [34]

1. Simulation project initialization and material properties database setup: The custom material properties needed for the device are defined in this step using the easy-to-use material editor interface of CoventorWare
2. Process definition: In this step, a sequence of virtual fabrication processes is defined to create the 3D model from a 2D layout. The processing steps are mainly layer growth steps with defined materials and thicknesses, as well as patterning steps using the layout masks.
3. Layout editing: A mask is needed for each of the etch steps defined in the process sequence. These masks can be edited in any standard layout editor or using the layout editor available in CoventorWare.

4. Building the 3D model: In this step, CoventorWare builds a 3D model for the structure, based on the information in the 2D layout and the processing sequence. A 3D model for a 10μm thick cantilever with 400μm long folded-springs, obtained by performing the previous steps, is shown in Fig. (4.5).
5. Naming entities: In this step, the solid bodies and surfaces of interest are assigned distinct and expressive names. These names will be used later to assign boundary conditions and other simulation constraints to each specific entity.
6. Meshing: In this step, the volumes and surfaces of the 3D model are divided into a mesh of small elements. The shape and size of the mesh elements are chosen to accurately represent the volume or surface geometry. The type of the mesh elements is chosen based on the function of the entity they represent. For instance, a metallic fixed electrode is represented by surface elements rather than volume elements as its only role in the simulation is the presence of a surface charge distribution, with no mechanical deflections. Contact surfaces are also assigned surface mesh elements if they encounter no mechanical deflections. The meshed model of the structure in Fig. (4.5) is shown in Fig. (4.6). The edge length of the mesh elements of the beam is in the order of 10-12μm. It is worth stressing that choosing the suitable meshing options and mesh element sizes is important for the accuracy of the solution and influences the simulation time [34].
7. Defining simulation type and boundary conditions: For the problem in hand, a coupled electrostatic/mechanical simulation is needed. Electrostatic boundary conditions are defined in this step by assigning a zero voltage to the bottom electrode and the desired voltage is applied to the beam. Mechanical boundary

conditions are also defined by defining a contact constraint between the beam and the contact and stopper bumps, as well as total mechanical fixing for the bottom sides of the anchors.

8. Simulation: This coupled field problem is solved in CoventorWare in an iterative fashion similar to the method used for the semi-analytical model in Chapter 3. The solver first solves the electrostatic problem to determine the attraction pressure on the beam, and then this pressure is delivered to the mechanical domain solver to determine the corresponding beam deflection profile. After that, the new beam profile is iterated back to the electrostatic solver to find the new capacitance of the structure and the corresponding electrostatic pressure, and so on until the solution converges in both the electrostatic and mechanical domains.
9. Extracting the results: The contact force is directly obtained after simulating the problem for the contact surfaces defined earlier in the mechanical boundary conditions. The maximum beam deflection is also provided which allows for calculating the peak electric field in the structure. CoventorWare allows for a wide variety of simulation results to be visualized as contours on the model geometry in an advanced 3D result viewer. The obtained results for the cantilever switch in Fig. (4.5, 4.6) are shown in Fig. (4.7).

4.2.2. High Force Contact Switch Structures

A high force bridge-type switch structure has been introduced in Chapter 3. The results shown in Fig. (3.22) indicate that the switch produces 2mN contact force at 48V/μm peak electric field. Moreover, changing the spring shape to a folded style has been investigated. The performance of the folded-spring version of the switch is

illustrated in Fig. (4.8). The folded-spring switch produces 1.8mN contact force at 50V/μm peak electric field.

4.2.3. Stress Gradient Deflections

The effect of stress gradients can be simulated using CoventorWare by introducing a vertically varying stress function to the elements of the beam mesh. The effect of introducing 2MPa/μm and 5MPa/μm vertical stress gradients to the folded-spring bridge structure is shown in Fig. (4.9) before applying any actuation bias. Max downward deflections of 0.8μm and 2μm are caused by these values of stress gradient, respectively. By actuating these initially non-uniform structures, the 0.8μm deflected structure gave approximately the same contact force as the initially uniform structure, but the 2μm deflected structure gave a 25% reduced contact force because of the large nonuniformity of the beam profile. Based on these results, the acceptable range for stress-gradient deflections is roughly estimated as ±1μm for such structures with 4μm initial gap height.

For cantilever structures, the effect of stress gradients is more pronounced causing larger initial deflections. A cantilever of exactly half the shape of the bridge structures described above encounters an approximately 4 times the magnitude of the deflection of the corresponding bridge structure at the same stress gradient. This is the reason of preferring bridge structures for their relative immunity against stress gradient effects

4.2.4. Mechanical Resonant Frequency

The modal mechanical analysis available in CoventorWare allows for calculating the mechanical resonant frequency of switch structures. The largest size bridge structures presented in this work encounter a fundamental resonant frequency of more than

11KHz. This value is relatively low, but remains within the acceptable range for MEMS switches as discussed earlier. Smaller size structures which produce lower contact force are expected to encounter higher resonant frequency, due to the lower beam mass.

4.3. RF PERFORMANCE

The main function of the RFMEMS contact switch is to switch signals in the DC and relatively low RF range; a distinction for contact switches over capacitive switches which can only switch high frequency signals. Increasing the RF band of operation for a contact switch allows for a wider range of applications in the RF and wireless communication systems.

The RF performance of an RFMEMS contact switch design is best validated by 3D finite element electromagnetic simulator such as Ansoft HFSS^{TM}. This widely used electromagnetic simulator uses an adaptive meshing technique. The solver keeps decreasing the sizes of the mesh elements for several iterations until the electromagnetic solution converges among two or more successive iterations. RF signal excitation ports are defined in the 3D model created for the problem, and the S-parameters can be directly obtained after the electromagnetic field solution is performed for the specified frequency range.

Fig. (4.10) shows a 3D model prepared for electromagnetic simulation of a high force bridge structure. Most of the model dimensions are declared as simulation parameters to enable the simulation of all switch structures with different actuator and spring dimensions by simple assignment of different values to the geometrical parameters. A sample small area switch structure is shown in Fig. (4.11). Furthermore, the vertical gap between the switch beam and the bottom metal layer is a variable dimension to

allow simulating the switch performance in both the On and Off states. A vertical cross-section of the model at one of the contact bumps is shown in both states in Fig. (4.12). The excitation ports in this model are defined to have 50Ω source or matching impedance. The CPW feed lines are also designed for 50Ω line impedance.

The performance of an RFMEMS contact switch is basically measured by the variation of two RF parameters versus frequency; these are the isolation and insertion loss. The isolation is the ratio between the signal power leaking at the drain port and the power delivered at the source port when the switch is Off. Ideal isolation value is zero, or $-\infty$ dB. Non-ideal isolation is mainly caused by the capacitive coupling of the signal through the switch structure. The isolation undesirably increases with frequency increase because of the decreasing impedance of the capacitances in the structure. On the other hand, the insertion loss is the ratio between the signal power received at the drain port and the power delivered at the source port when the switch is On. Ideal conditions yield an insertion loss value of 1, or 0dB. Non-ideality of the insertion loss is mainly caused by the losses in the signal line and switch structure, as well as signal reflection due to the disturbance of the switch structure to the CPW line geometry. The insertion loss decreases with frequency increase due to the growing effect of the discontinuities in the structure as well as the increased resistive losses due to the reduction of the skin depth. Several RF matching techniques can be used to enhance the RF performance of RFMEMS switches [1].

The isolation and insertion loss variations versus frequency for the high force bridge-type switch structure of Fig. (4.10) are shown in Fig. (4.13). Table (4.1) compares the simulated RF performance of this high force switch structure with experimental measurements reported on one of the most recent commercial RFMEMS contact switch projects [18].

Another configuration for the signal conduction style of the switch is shown in Fig. (4.14). In this series switch configuration, the switch structure serves as part of the signal line. The simulated RF performance of this structure is shown in Fig. (4.15). The insertion loss is much enhanced compared to the previous case because the two contact bumps are now functional in a parallel, rather than a series, manner. The drawback of this inline configuration is the degraded isolation. However, the obtained isolation can be enhanced by reducing the overlap area between the beam and the RF line near the contact tips.

4.4. TECHNOLOGY CHARACTERIZATION

A special surface micromachining technology based on thick electroplated nickel for the beam is proposed for the prototyping of the contact switch designs presented in this work. This technology is developed by the RFMEMS team at IMEC vzw, Leuven, Belgium. A vertical cross-section describing the proposed technology and the associated 5 masks is given in Fig. (4.16).

4.4.1. Technology Features

The technology provides a 0.5μm ground metal layer for the routing of the RF and DC signals and to implement the fixed bottom electrode. This layer is optionally a stack of two metal layers, the top of which is the contact metal. Mask no.1 is used to pattern this layer.

A polyimide sacrificial layer is then used to define the required air gap between the beam and the bottom metal layer. Two values for the air gap height are investigated in the first set of prototype devices; these are 2μm and 4μm. Mask no.2 is used to pattern the sacrificial layer to define the suspended and anchored regions of the Ni beam.

Contact and stopper bumps are then defined by controlled etching for small cylindrical dimples in the sacrificial layer of 1μm depth. The contact and stopper bumps are defined by mask no.3.

Since the contact metal has to be present on the two contact surfaces, another thin layer of the contact metal is deposited and patterned to cover the contact dimple in the sacrificial layer, using mask no.4.

Finally, thin electroplating seed layers are deposited by sputtering all over the wafer and a masked growth of nickel is performed. Then the mask material is removed and the seed layers are etched from the regions where no nickel has been plated. Mask no.5 is used to define the nickel structures. Two values for the nickel thickness are investigated in the first set of prototype devices; these are 7μm and 10μm.

For all suspended nickel structures of dimensions greater than 40μm x 40μm, release holes are added to the nickel plating mask to allow for uniform and fast etching for the sacrificial layer. A hexagonal mesh distribution is mainly adopted to provide the most uniform area coverage. Two release hole-diameters of 10μm and 16μm are investigated, with pitches of 40μm and 45μm respectively.

4.4.2. Characterization Test Structures

Being a custom developed technology, some characteristic parameters need to be determined by measurements on test structures implemented with its specific process flow. These technology-sensitive parameters include: the contact resistance/force characteristics of the employed contact material, the electrostatic breakdown field of the air gap between the beam and the bottom electrode, the effective elasticity of the beam material including the release holes, and the RF losses encountered per unit length of the fabricated CPW lines.

To characterize the contact resistance/force behavior of the contacts implemented using the proposed technology, the test structure layout in Fig. (4.17) has been designed. The structure includes a nickel disk with four contact bumps, suspended by low stiffness springs. The force is applied to the disk by an external needle, and the resistance is measured by means of four-point Kelvin setup, in which a current is biased in a specific metal route through any two of the contact bumps and the voltage across the contacts is measured using another metal route to exclude the resistance of these metal routes from the measured resistance.

The electrostatic breakdown of air between the beam and bottom electrode is determined using the structures in Fig. (4.18, 4.19). The first structure is a stiffly anchored square beam that does not encounter pull-in before the breakdown electric field is reached, and thus allows determining the breakdown field at gap heights of 2 and 4μm according to the sacrificial layer height used. On the other hand, the second structure employs much less stiffer springs which allow the beam to be attracted down until the many bumps of 1μm height reach their respective landing islands. And then by increasing the applied voltage, the breakdown field can be detected at 1μm air gap height between the two electrodes.

The mechanical properties of the fabricated nickel beams including the effect of the release holes can be determined by means of tip displacement versus force characterization of simple cantilever structures implemented using the proposed technology.

Finally, the RF signal losses caused by the implemented CPW lines can be simply determined by fabricating specific lengths of the CPW structures and measuring the ratio between the drain and source signal power. These losses are expected to be relatively high in the proposed process flow because of the relatively low thickness of

the RF bottom metal layer. Further technology enhancements are expected to include a thicker and higher conductivity bottom metal layer.

4.5. SAMPLE DEVICE DESIGNS

Even with the relative simplicity of the available technology, it provides a wide range of design variations to practically test different device structures and configurations. Allowed variables include: nickel beam thickness, air gap height, electrical test configuration, actuator size, beam shape, and spring shape. The design tree presented in Fig. (4.20) illustrates the different suggested variations to be investigated for implementation using the proposed technology. Each mechanical device configuration requires a different mechanical design for maximum contact force production. This mechanical design has been performed using the relatively fast and accurate semi-analytical model presented in Chapter 3. Two sample design curves are shown in Fig. (4.21, 4.22) for large area and small area actuators respectively. The different prepared designs cover a wide range of contact force between 0.1mN and 2.4mN.

It is worth mentioning that all the designs are prepared using 180GPa modulus of elasticity for the beam material, which is 13% lower than the 207GPa typical nickel modulus of elasticity [30]. This reduced value is used to lessen the effect of the release holes on the rigidity of the fabricated beams. The electroplating process can also result in a lower material hardness.

Finally, the semi-analytical model has been described as a 2.5D model because it includes the effect of some parameters in the third dimension like the width of each beam section which is included in the flexural rigidity terms. However, the model assumes that the contact and stopper bumps exist all along the third dimension of the device. This can be validated for the stopper by implementing it as a line of several

bumps as shown in the sample switch layout in Fig. (4.23). However, this is not desirable for the contact tips as we seek the highest pressure on these bumps. Only two contact bumps are present in each device, which is one of the main sources of error in the model results compared to 3D finite element simulation as in Table (3.5).

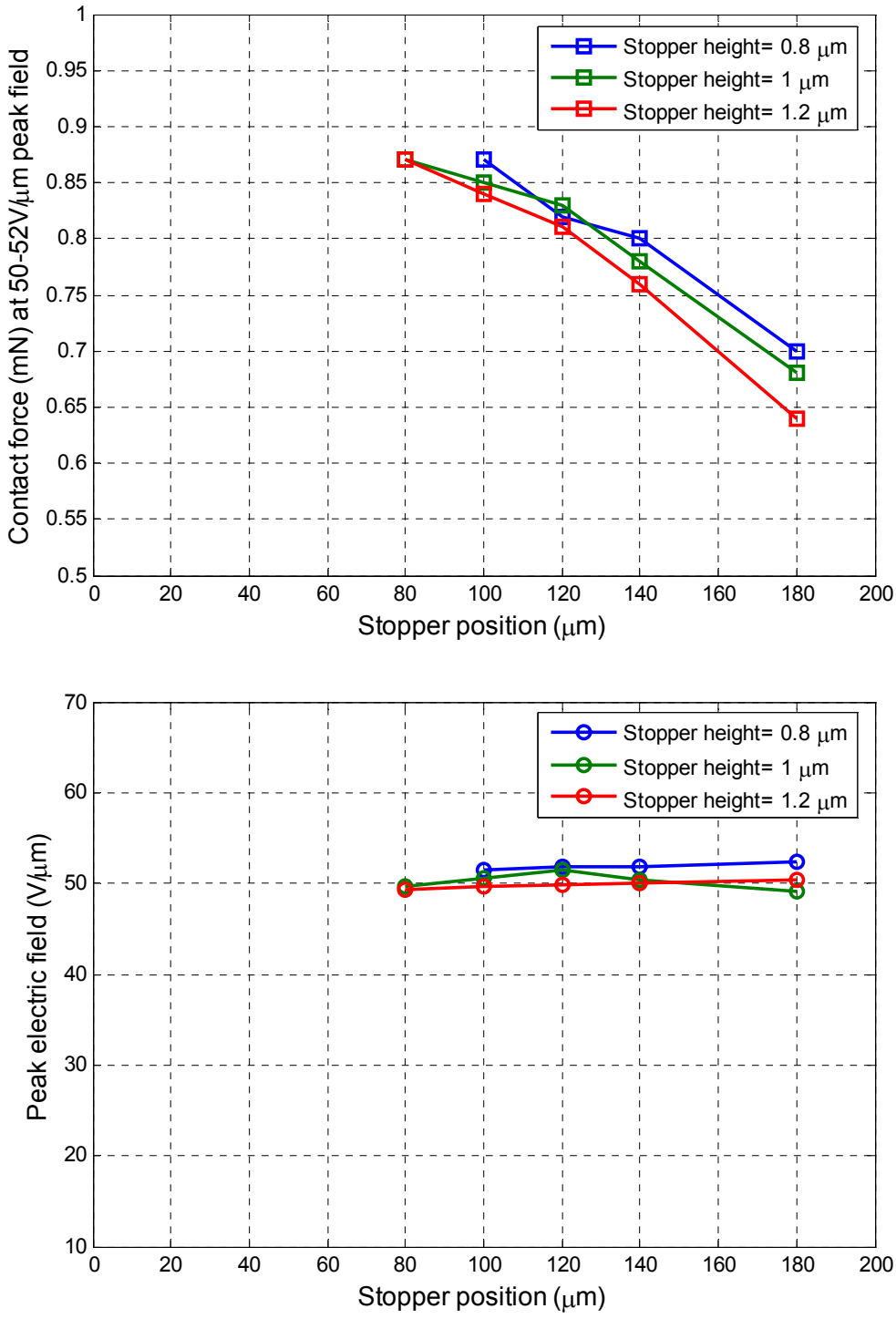

Figure 4.1. Contact force results for different stopper bump heights and positions (top). Peak electric field values for the same data points are shown (bottom). Other design parameters values are taken from Table (3.3).

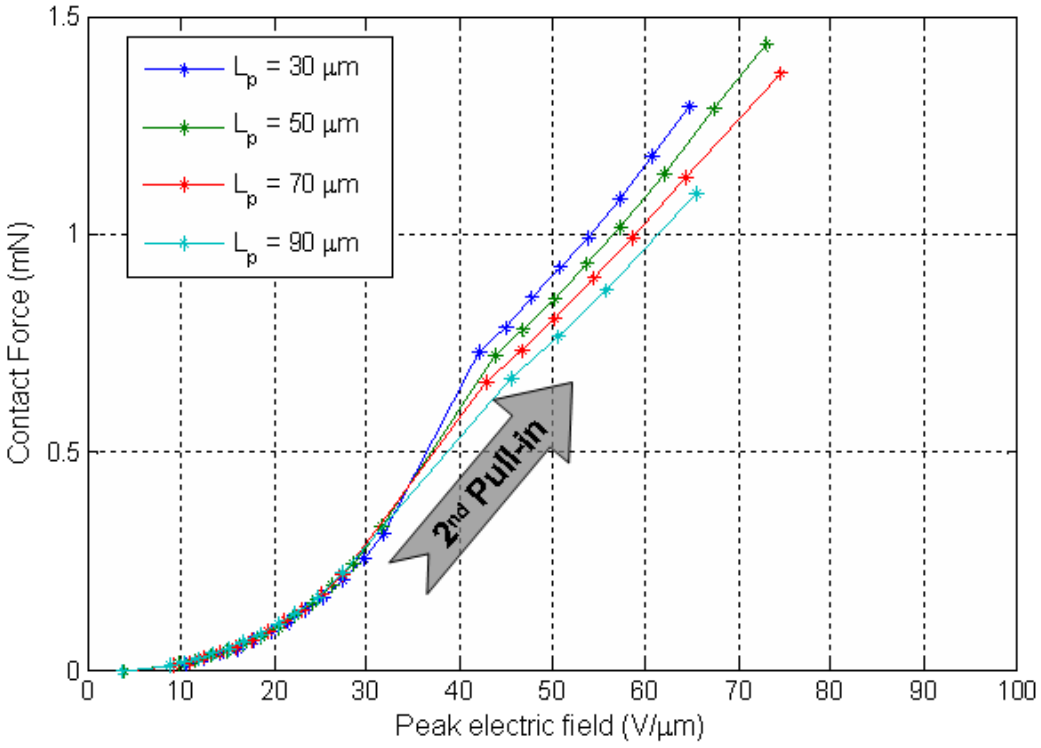

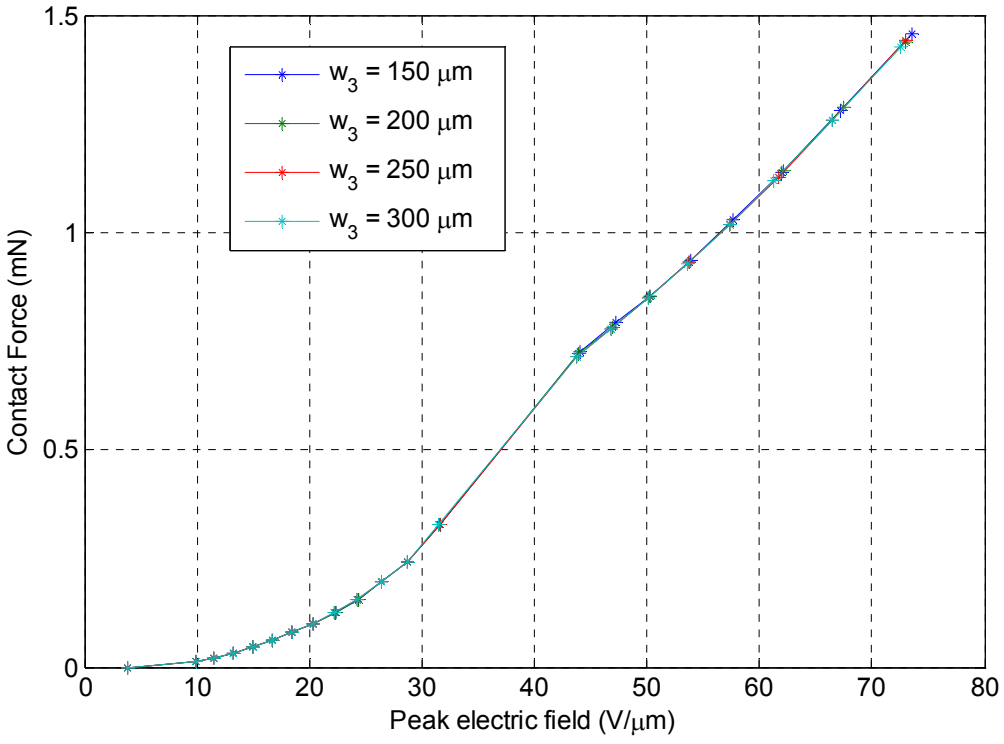

Figure 4.2. Effect of the passive section length and width on the obtained contact force. Other design parameters are given in Table (3.3).

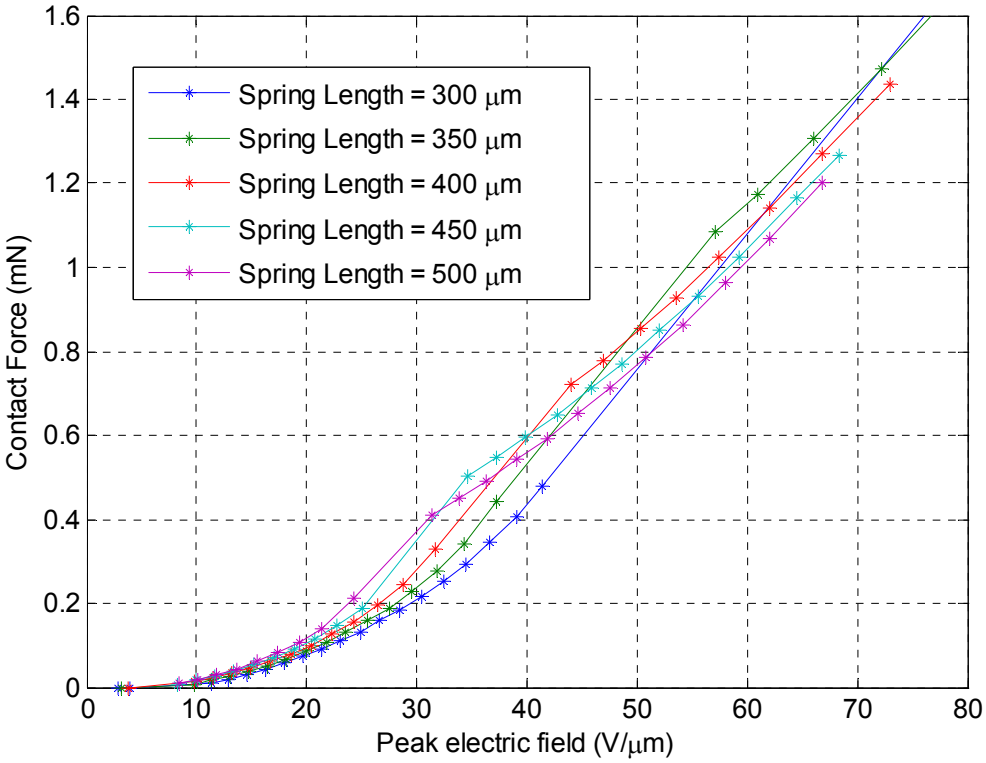

Figure 4.3. Effect of the spring stiffness on the obtained contact force. An optimum spring length of 400μm for sample structure number (3) gives the highest contact force at 50V/μm peak electric field.

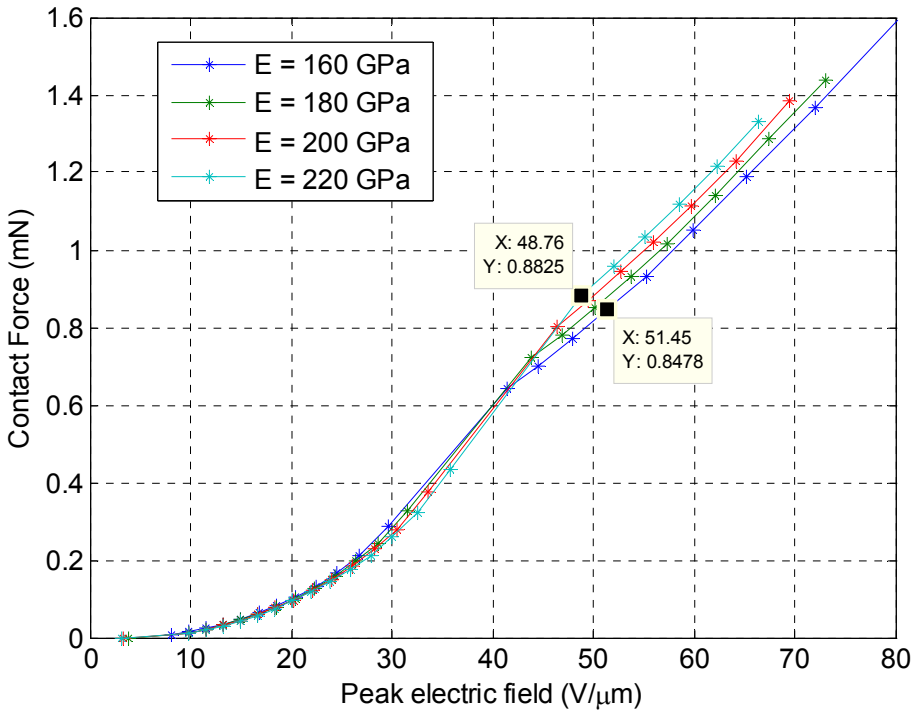

Figure 4.4. Effect of the beam material elasticity on the obtained contact force. Other design parameters are taken from Table (3.3).

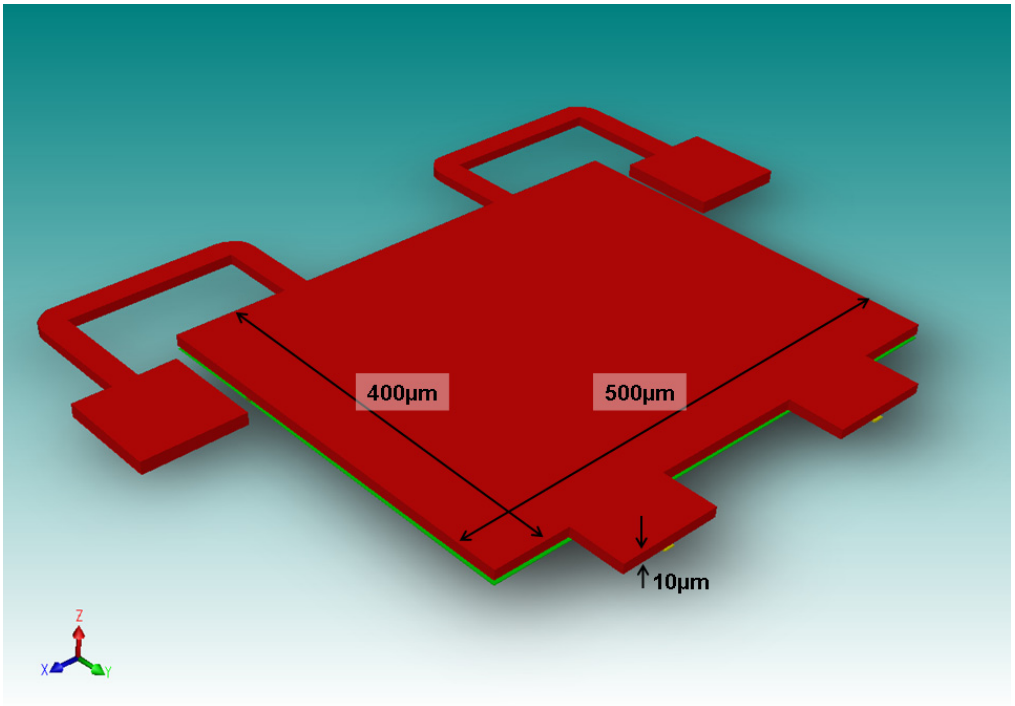

Figure 4.5. A 3D model developed using CoventorWare for a cantilever switch with folded springs. The view is to scale.

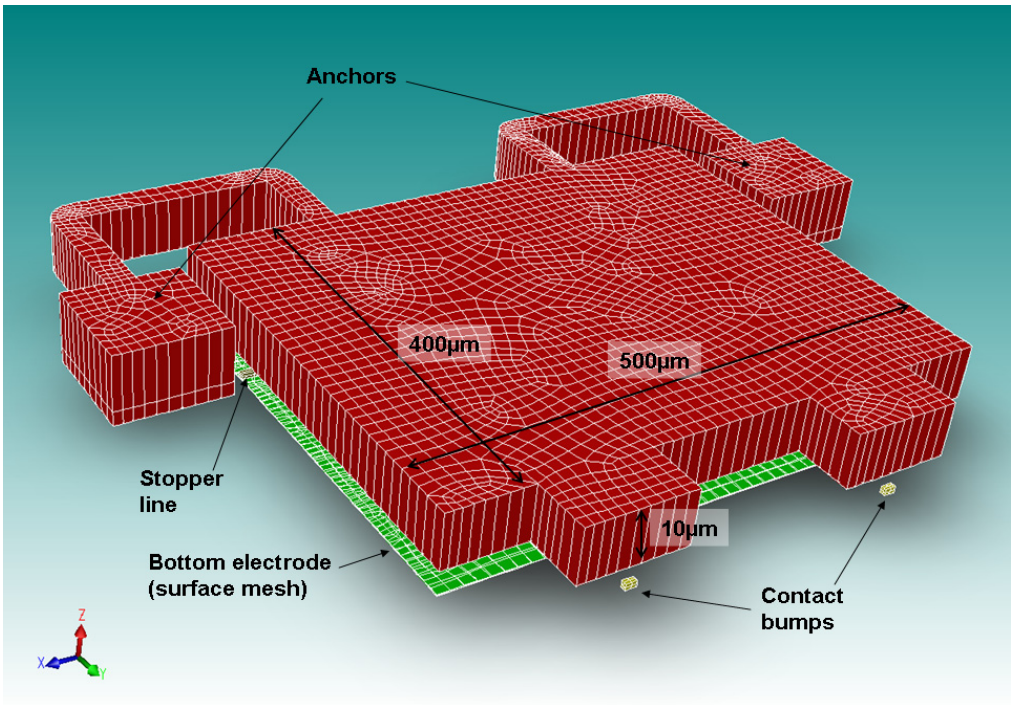

Figure 4.6. Meshed 3D model for a cantilever switch with folded springs. The view is exaggerated in the z-axis to show the small structural details.

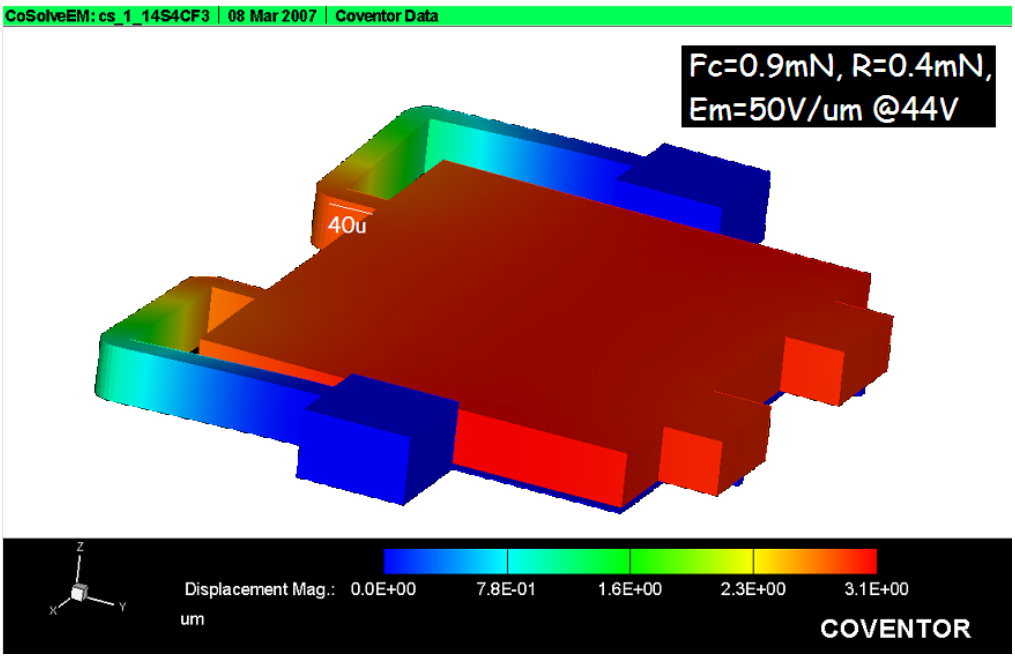

Figure 4.7. Deflected beam shape after simulating the structure in Fig. (4.6).

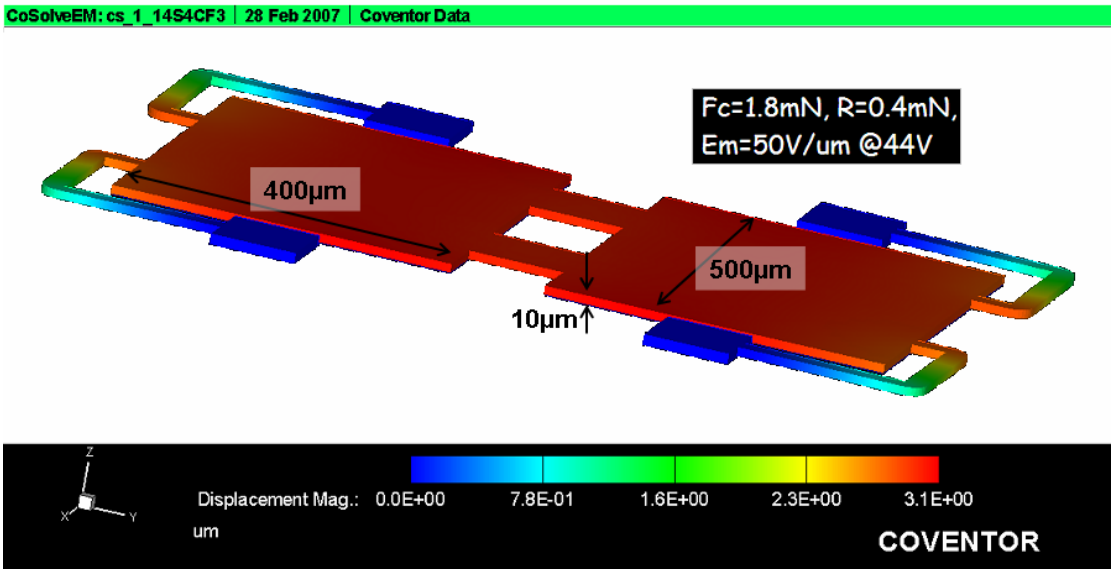

Figure 4.8. A folded-spring bridge-type switch structure.

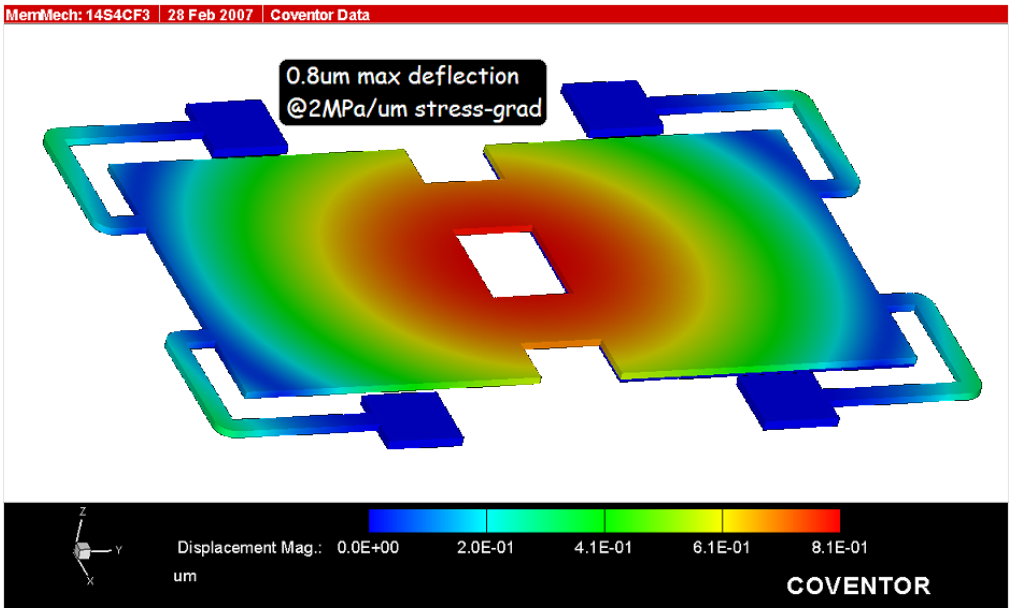

(a)

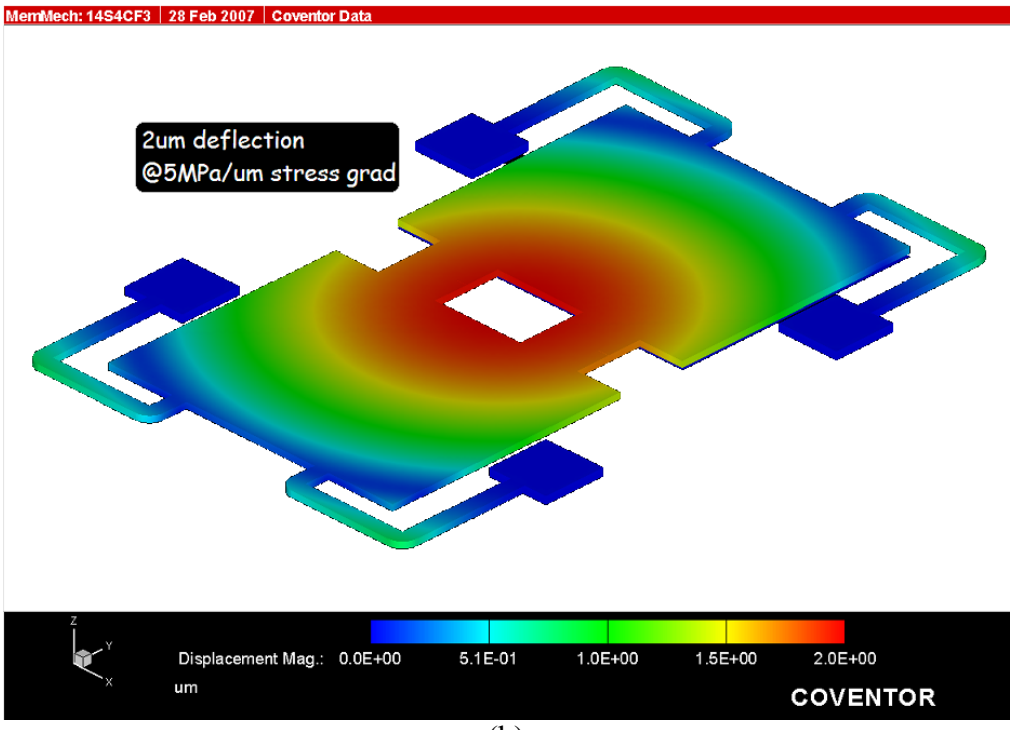

(b)

Figure 4.9. The effect of introducing stress gradients to the folded-spring bridge switch. The stress gradients cause the beam to bow downwards by different strengths for different stress gradient values.

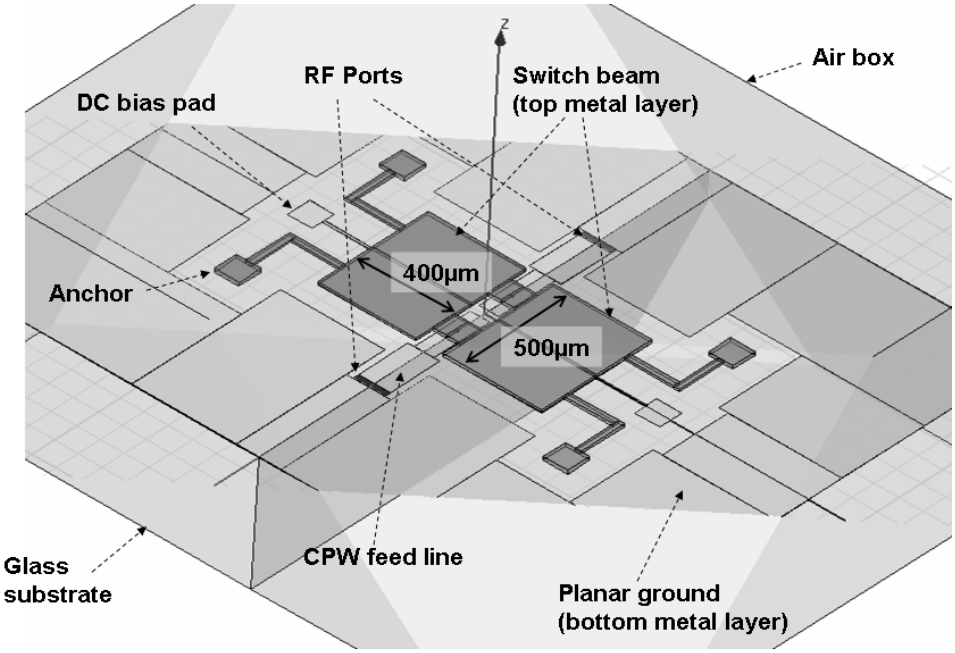

Figure 4.10. A parametric 3D model prepared for HFSS electromagnetic simulation of bridge switch structures.

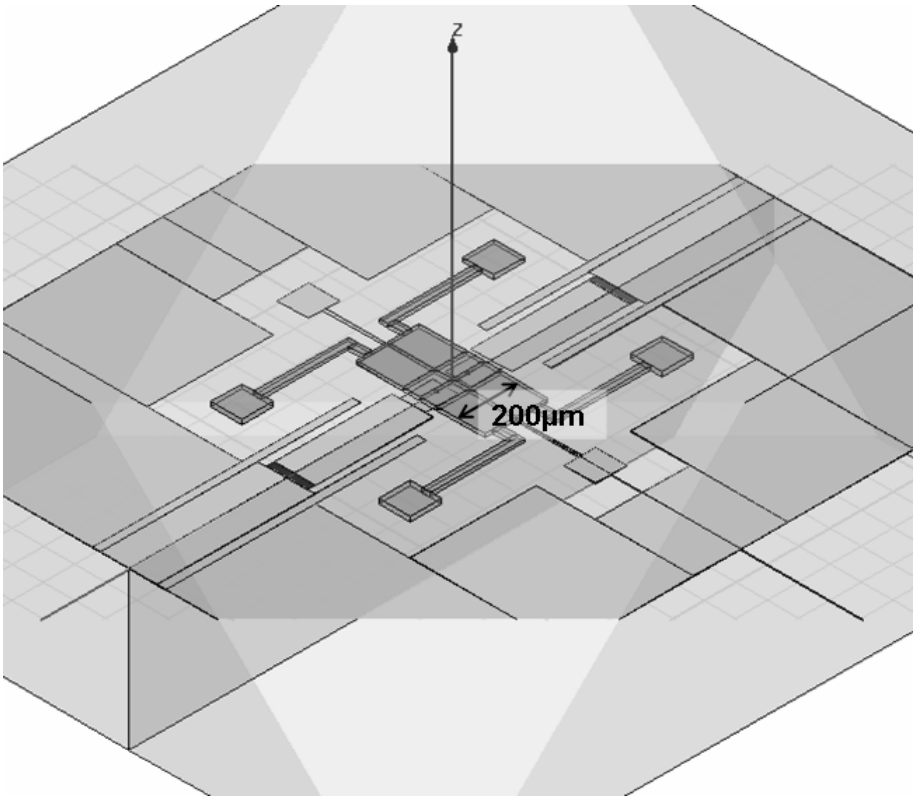

Figure 4.11. The 3D model for a small area device, obtained by reconfiguring the geometrical parameters of the model in Fig. (4.10).

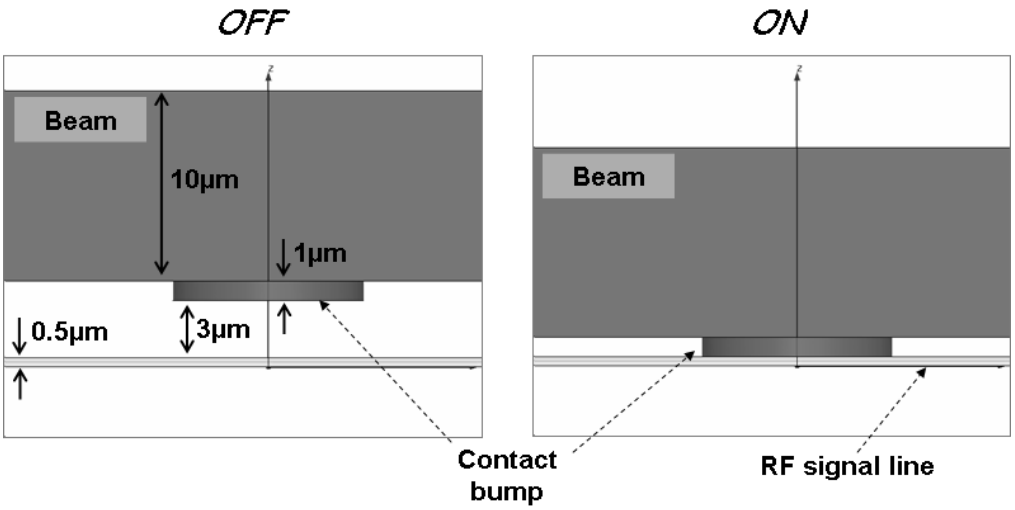

Figure 4.12. Varying the gap distance between the beam and the RF line to simulate the Off and On states.

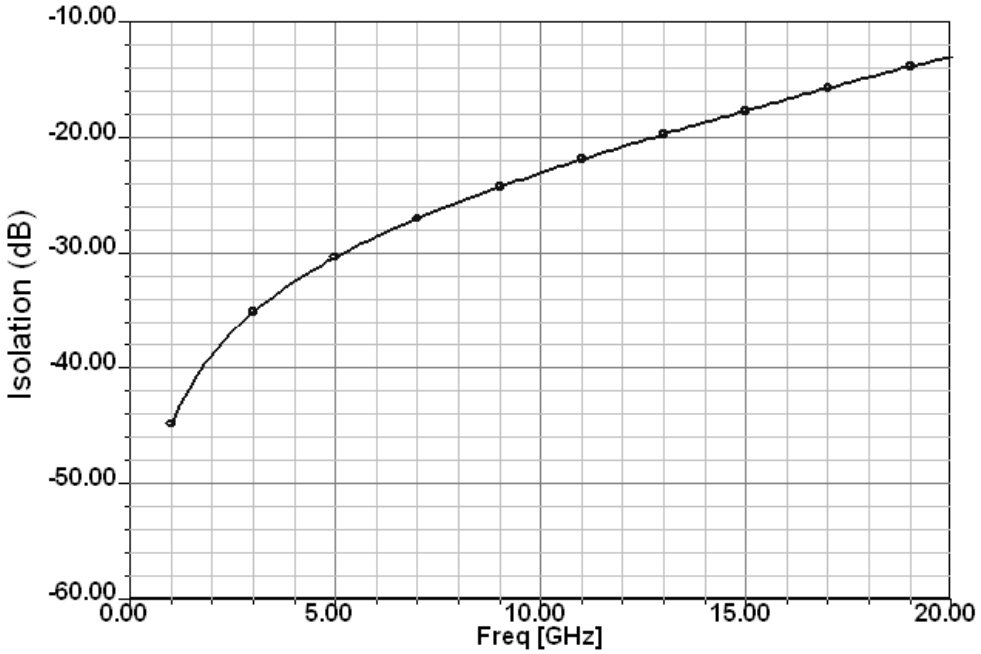

(a)

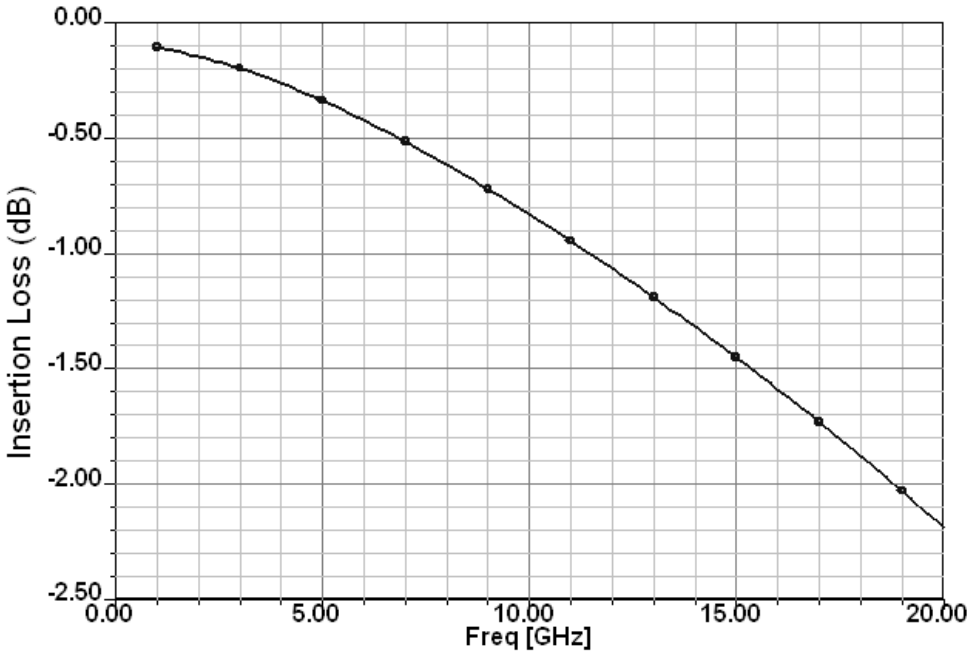

(b)

Figure 4.13. Simulated isolation (a) and insertion loss (b) variation versus frequency for the high force bridge structure of Fig. (4.10).

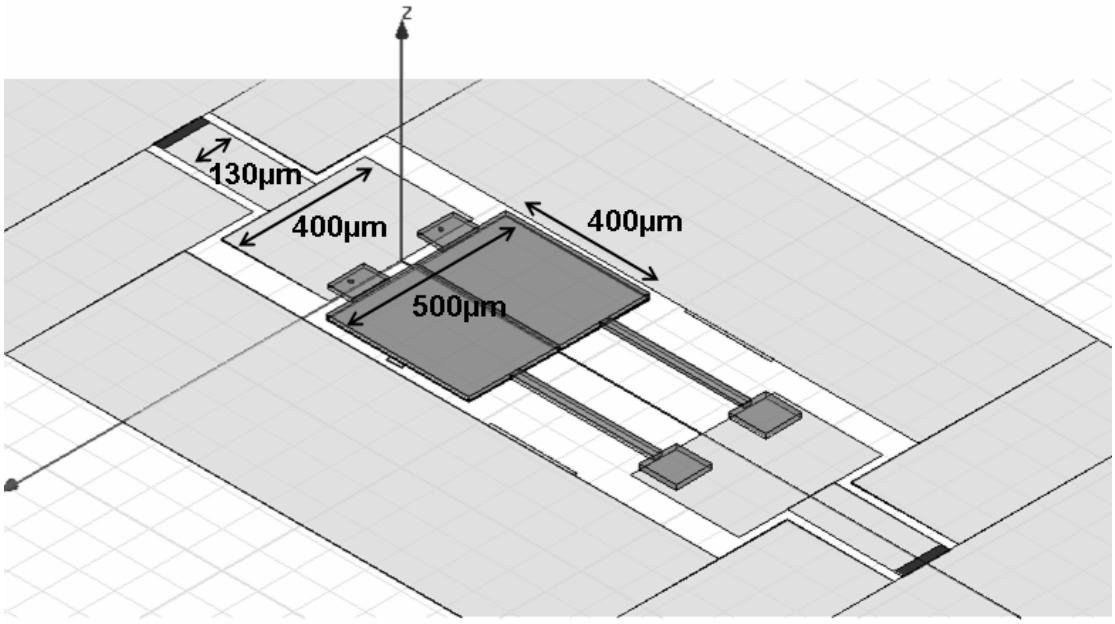

Figure 4.14. HFSS model for a cantilever inline series switch.

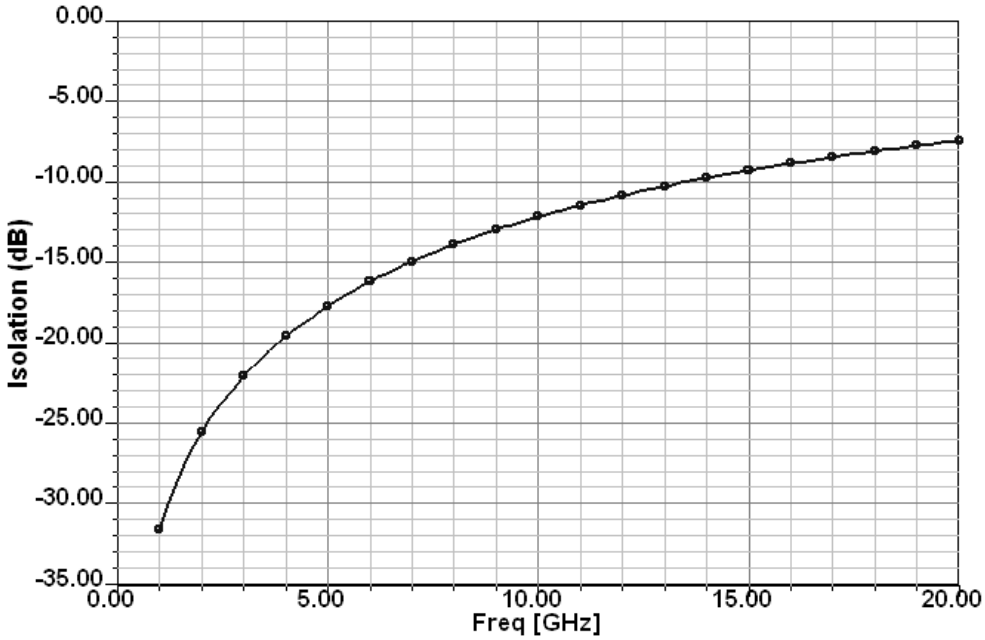

(a)

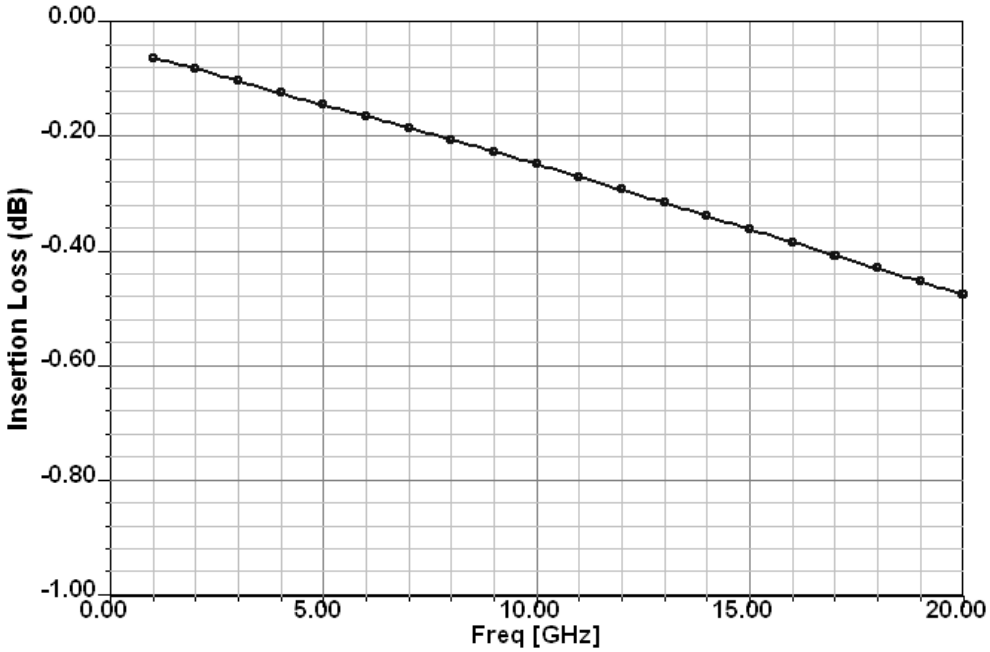

(b)

Figure 4.15. Simulated isolation (a) and insertion loss (b) variation versus frequency for the inline cantilever switch structure of Fig. (4.14).

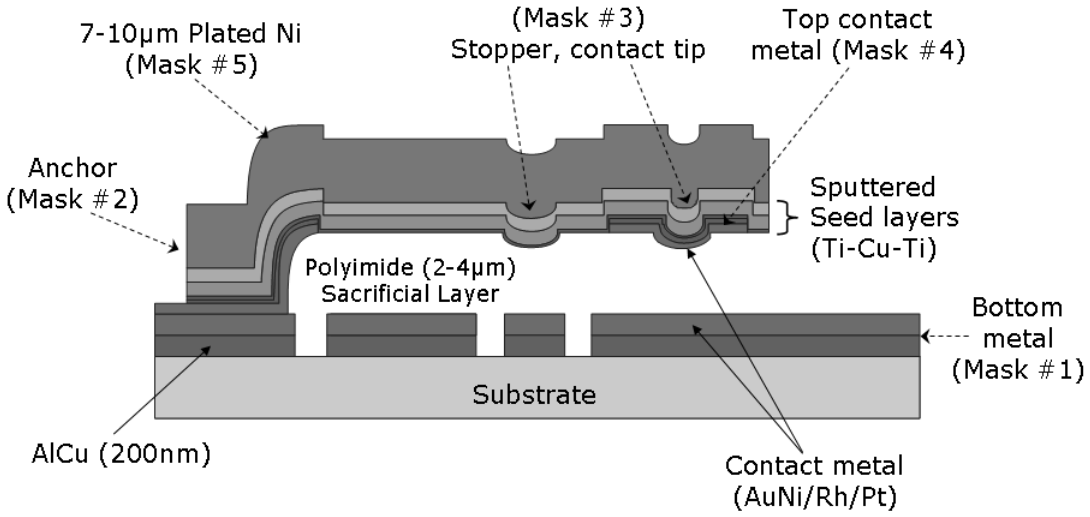

Figure 4.16. RFMEMS contact switch technology cross-section. A 5-masks processing flow is involved. This cross-section is provided by P. Ekkels, IMEC vzw, Leuven, Belgium. The dimensions are not to scale.

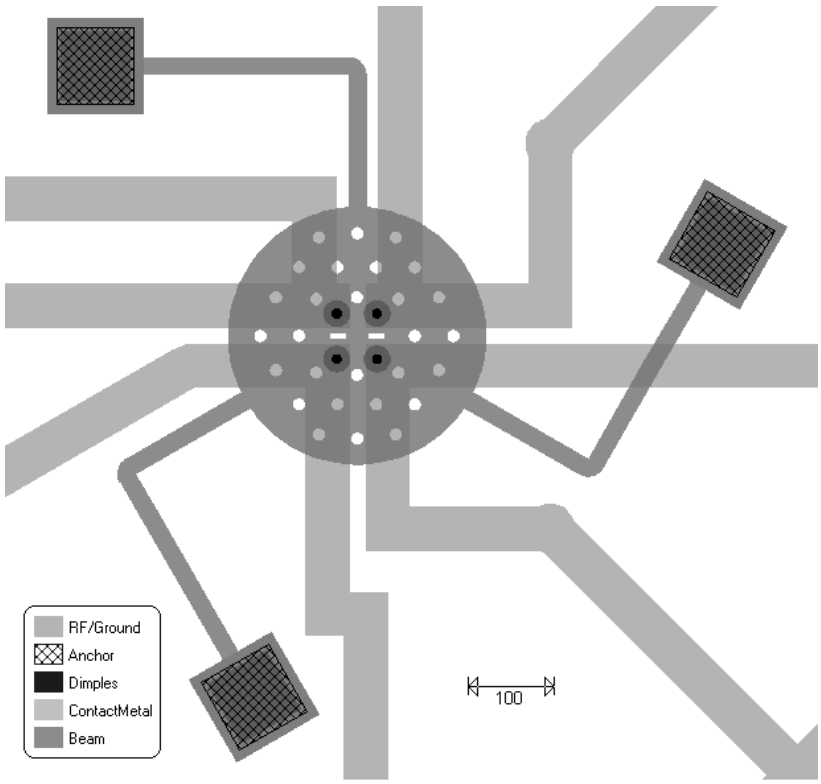

Figure 4.17. Layout of the contact resistance/force characterization structure.

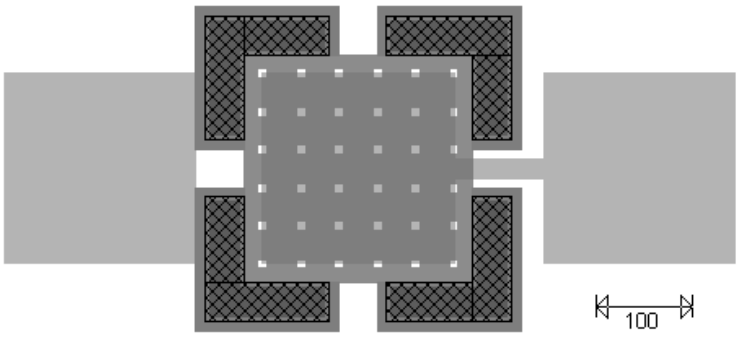

Figure 4.18. Layout of test structure to determine the electrostatic breakdown for 2/4µm air gaps.

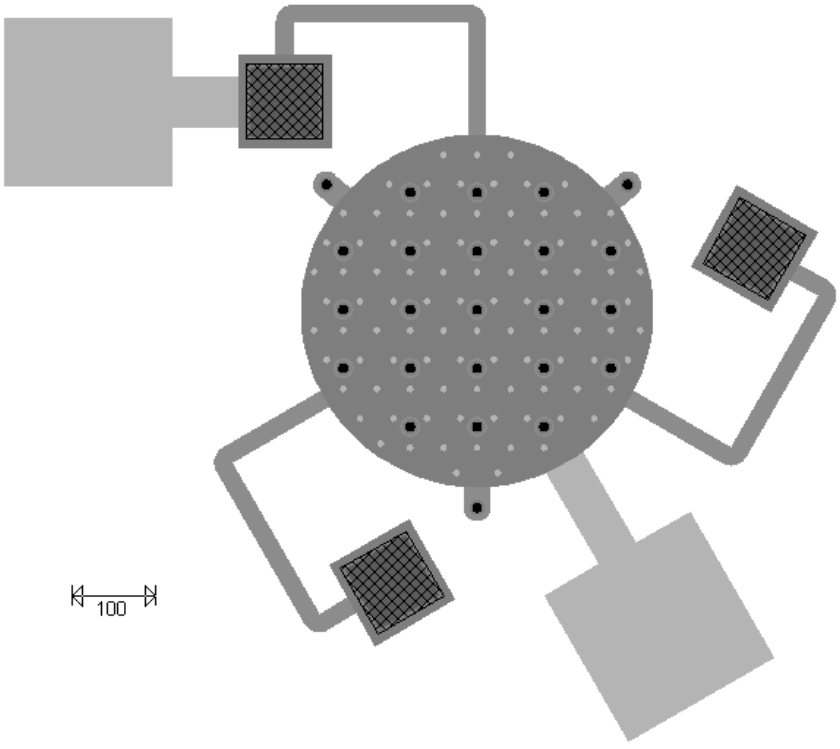

Figure 4.19. Layout of test structure to determine the electrostatic breakdown for 1µm air gaps.

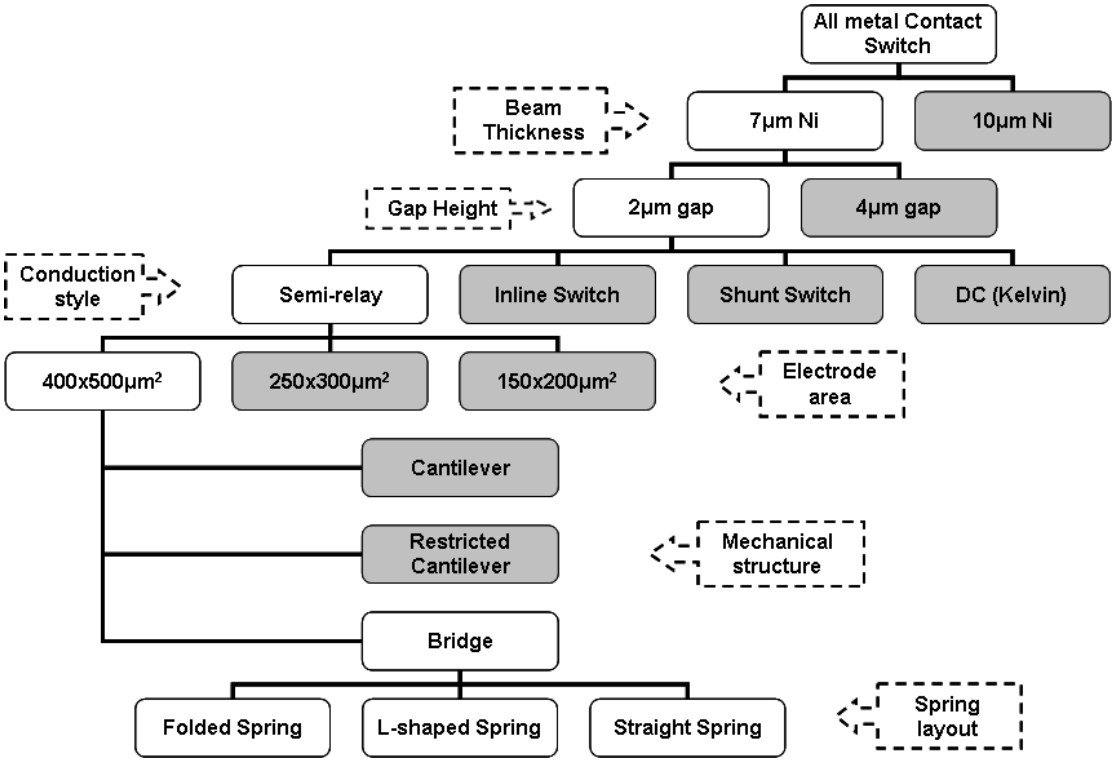

Figure 4.20. Design tree for the different suggested contact switch designs. Entries with gray background invisibly bear the same sub-tree as their white coworker entries.

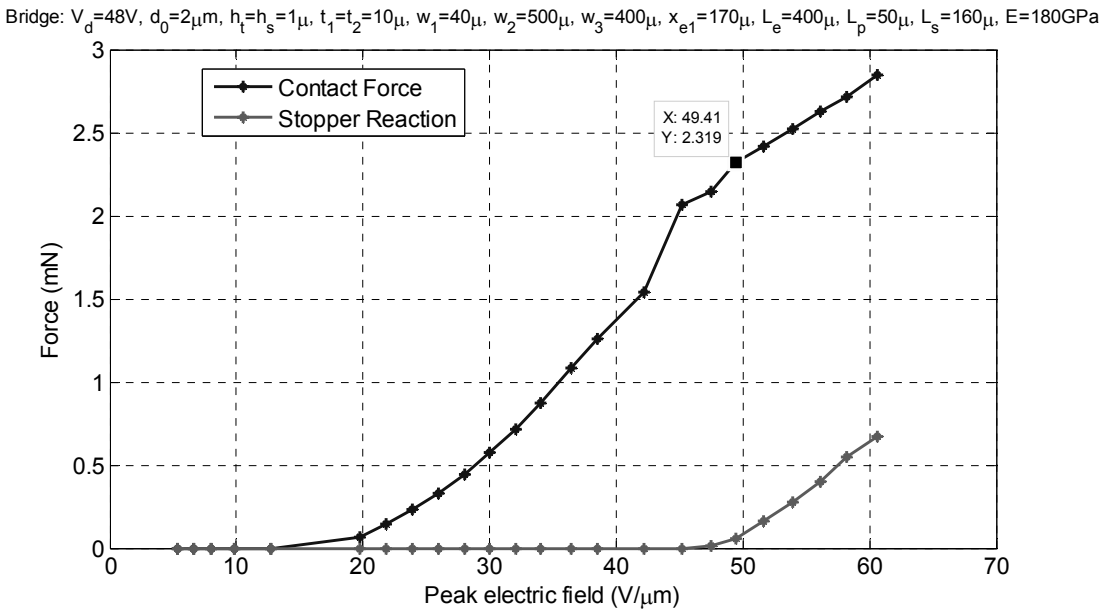

Figure 4.21. A high force bridge design producing more than 2.3mN contact force before breakdown. Design parameters are visualized in Fig. (3.16)

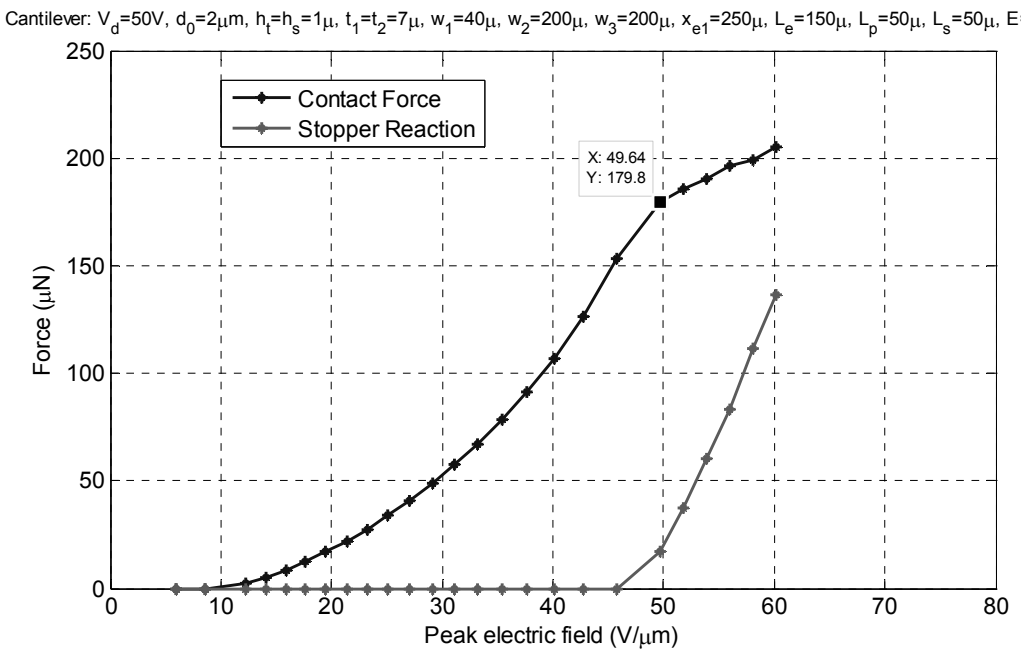

Figure 4.22. A low force cantilever design producing around 180μN contact force before breakdown. Design parameters are visualized in Fig. (3.16)

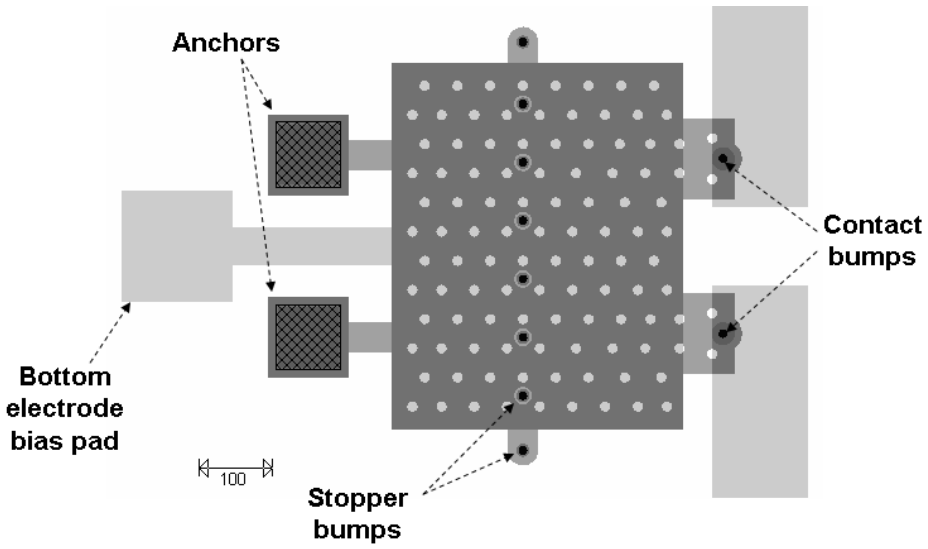

Figure 4.23. Sample cantilever switch layout.

Frequency	Parameter	TeraVicta switch experimental results [18]	High force bridge simulation results
1 GHz	Isolation	-30 dB	-45 dB
	Insertion loss	-0.1 dB	-0.1 dB
7 GHz	Isolation	-25 dB	-27 dB
	Insertion loss	-0.4 dB	-0.5 dB

Table 4.1. Comparing the simulated RF performance of the presented high force bridge structure with the recently reported TeraVicta commercial switch measurements.

CHAPTER 5

CONCLUSIONS AND FUTURE WORK

5.1. CONCLUSIONS

The main achievements of this work are the development of the relatively fast and accurate semi-analytical model for electrostatically actuated beams, and using this model to design high force RFMEMS contact switches with acceptable RF performance to be implemented in a simple all-metal surface micromachining technology based on thick electroplated nickel beams.

Several basic and advanced design considerations and reliability challenges for RFMEMS contact switches have been discussed in this work, including: reliability of microcontacts, air gap breakdown, mechanical stability, and the effect of stress gradients and release holes.

A simplified analytical model for electrostatically actuated beams has also been presented for the sake of comparison with the developed semi-analytical model. For a typical high force structure, the contact force calculated using the semi-analytical model deviated by 3.5% from the 3D finite element simulation, compared to -62% error in the value obtained by the simplified analytical model.

Many RFMEMS contact switches producing contact force in the range between 0.1mN and 2.4mN have been designed using the semi-analytical model. The numerical solutions of the model equations have been performed using MATLAB®. The results of the model have been verified for different cases using CoventorWare which is a 3D finite element simulator optimized for MEMS devices. The RF performance of the designed structures has been simulated using Ansoft HFSS. An

isolation of -27dB and insertion loss of -0.5dB at 7GHz are predicted for a typical high force structure producing more than 2mN contact force, which is principally sufficient to reduce the contact resistance of the switch, and hence reduce the RF losses at the contact interface.

5.2. FUTURE WORK

Several RFMEMS contact switch designs will be realized using the special technology described in Chapter 4, which is provided by the RFMEMS team at IMEC vzw, Belgium. Subsequently, measuring the DC and RF performance of the fabricated devices will be carried out, with emphasis on the role of the contact force on the device behavior.

The technology characterization test structures described in Chapter 4 will also be implemented and tested. The results obtained from these measurements will allow for better understanding of the effect of the fabrication technology and other conditions on the performance of the RFMEMS contact switches. Obtaining the exact values of certain interesting parameters, like the breakdown electric field of the air gap between the beam and the bottom metal, will allow for further optimization of the contact force in future designs. The micromachined contact resistance/force characterization structures will contribute to faster and more accurate characterization of the different contact material options.

Investigating other applications for the developed modeling technique is another aspect of the future work. With simple modifications, the model can be used to design relay structures which encounter a dielectric section in the beam to electrically isolate the top electrostatic actuator electrode from the contact tips and the signal path. This

modification increases the number of practical applications of the devices, but requires a more advanced technology for its implementation.

Another application of the developed model and the proposed technology is to design air-gap capacitive switches. Traditionally, a capacitive switch employs a dielectric layer which isolates the bottom RF line from the beam. The presence of the dielectric necessitates dealing with complicated dielectric charging issues [1]. However, using a rigid beam with side stoppers as shown in Fig. (5.1) can permit the device operation without an isolation dielectric layer. The beam profile can be easily obtained using the semi-analytical model, and hence both the up and down state capacitances can be accurately calculated. With high accuracy, the model can predict the suitable actuation voltage which allows for beam pull-in without exceeding the breakdown field.

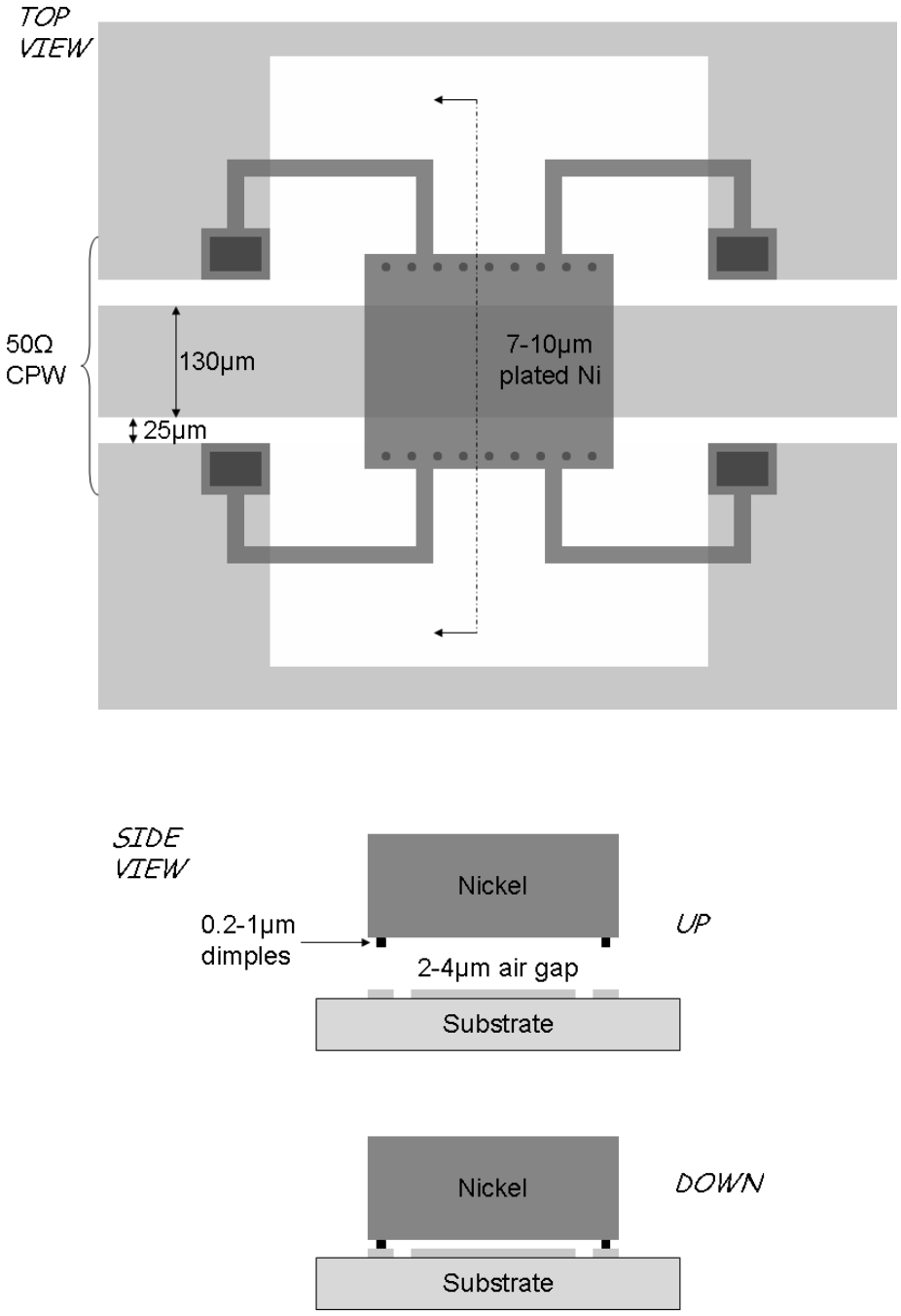

Figure 5.1. A proposed all-metal capacitive switch structure, to be implemented using the available technology and to be designed using the developed semi-analytical model.

REFERENCES

1. G. M. Rebeiz, *RF MEMS: Theory, Design, and Techniques*, (John Wiley and Sons, New Jersey, 2003).
2. Datasheet: "Miniature Relay 1-Pole (High Frequency Signal Switching), UM1 Series," (Fujitsu Components America, Inc., 2004).
3. H. Tilmans *et al.*, "MEMS for Wireless Communications: From RF-MEMS Components to RF-MEMS-SiP," J. Micromech. Microeng. **13**, S139–S163 (2003).
4. W. Johler, "RF Performance of Ultra-miniature High Frequency Relays," Electrical Contacts − Proceedings of the 49th IEEE Holm Conference on, 179-189 (2003).
5. S. Majumder *et al.*, "MEMS Switches," IEEE Instrumentation and Measurement Magazine **6**, 12-15 (2003).
6. Internet article: (http://www.wtc-consult.de) "The RF MEMS market II, 2005-2009," (Wicht Technologie Consulting, Germany, 2005).
7. K. Petersen, "Micromechanical Membrane Switches on Silicon," IBM J. Res. Develop. **23** (no. 4), 376-385 (1979).
8. H. De Los Santos *et al.*, "RF MEMS for Ubiquitous Wireless Connectivity: Part 2− Application," IEEE Microware Magazine **5** (no. 4), 50-65 (2004).
9. H. De Los Santos *et al.*, "RF MEMS for Ubiquitous Wireless Connectivity: Part 1− Fabrication," IEEE Microware Magazine **5** (no. 4), 36-49 (2004).
10. E. Thielicke and E. Obermeier, "A Fast Switching Surface Micromachined Electrostatic Rela y," Transducers, Solid-State Sensors, Actuators and Microsystems − 12th International Conference on, 899-902 (2003).

11. A. Morris *et al.*, "High-Performance Integrated RF-MEMS: Part 2− Switches," (wiSpry Inc., California, online article: www.wispry.com, 2003).

12. H. Lee *et al.*, "Micro-Electro-Mechanical Relays – Design Concepts and Process Demonstrations," Electrical Contacts – Proceedings of the 50th IEEE Holm Conference on, 242 – 247 (2004).

13. N. Nishijima *et al.*, "A Low-Voltage High Contact Force RF-MEMS Switch," IEEE MTT-S Digest **2**, 577-580 (2004).

14. J. Oberhammer and G. Stemme, " Design and Fabrication Aspects of an S-Shaped Film Actuator Based DC to RF MEMS Switch," IEEE J. MEMS **13** (no. 3), 421-428 (2004).

15. J. Qiu *et al.*, "A Bulk-Micromachined Bistable Relay With U-Shaped Thermal Actuators," IEEE J. Microelectromech. Sys. **14** (no. 5), 1099-1109 (2005).

16. J. Silvestre and L. Castaner, "Novel Low Voltage Electrostatic Micro-Relay," Abstract submitted to Eurosensors XIX Conference, Barcelona (2005).

17. J. McKillop, "Advanced Packaging: A Key Enabling Technology for RF MEMS," Presentation at Technology Roadshow for Advanced Packaging, MEMS and Nanotechnologies (2006).

18. J. McKillop *et al.*, "Design, Performance and Qualification of a Commercially Available MEMS Switch," Proceedings of the 36th European Microwave Conference, 1399-1401 (2006).

19. H. Kwon *et al.*, "Contact Materials and Reliability for High Power RF-MEMS Switches," MEMS – Proceedings of the 20th IEEE International Conference on, 231-234 (2007).
20. R. Coutu *et al.*, "Selecting Metal Alloy Electric Contact Materials For MEMS Switches," J. Micromech. Microeng. **14**, 1157-1164 (2004).
21. W. Johler, "Precious Metal-Reduced Contact Materials in Telecom- and Signal Relays," Electrical Contacts – Proceedings of the 47th IEEE Holm Conference on, 104-116 (2001).
22. D. Hyman and M. Mehregany, "Contact Physics of Gold Microcontacts for MEMS Switches," IEEE Transactions on Components and Packaging Technology **22** (no. 3), 357-364 (1999).
23. J. Schimkat, "Contact Materials for Microrelays," MEMS – Proceedings of the 11th Annual International Workshop on, 190-194 (1998).
24. H. Ziad *et al.*, "Design Considerations of the Electrical Contacts in (Micro)relays," Proc. SPIE **2882**, 222-229 (1996).
25. R. Peek and N. Wagar, *Switching Relay Design*, (Princeton, New Jersey, Van Nostrand, 1955).
26. N. Farghal *et al.*, "Investigation of $AuNi_5$ Films Deposited by Pulsed Laser Deposition for RF MEMS Switch Contacts," Mater. Res. Soc. Symp. – Proc. of, Vol. 980 (2007).
27. A. Wallash and L. Levit, "Electrical Breakdown and ESD Phenomena for Devices with Nanometer-to-Micron gaps," Proc. SPIE **4980**, 87-96 (2003).
28. P. Slade and E. Taylor, "Electrical Breakdown in Atmospheric Air Between Closely Spaced (0.2μm-40μm) Electrical Contacts," IEEE

Transactions on Components and Packaging Technologies **25** (no. 3), 390-396 (2002).

29. R. Dhariwal *et al.*, "Electric Field Breakdown at Micrometre Separations in Air and Nitrogen at Atmospheric Pressure," IEE Proc.-Sci. Meas. Technol. **147** (no. 5), 261-265 (2000).
30. R. Ross, *Metallic Materials Specification Handbook*, 3rd Edition, (E. and F. N. Spon, London, 1980).
31. R. Lee *et al.*, "Arc Erosion Behaviour of Silver Electric Contacts in a Single Arc Discharge Across a Static Gap," IEE Proc.-Sci. Meas. Technol. **148** (no. 1), 8-14 (2001).
32. J. Gere and S. Timoshenko, *Mechanics of Materials*, 4th Edition, (PWS Publishing, Boston, 1997).
33. H. Sadeghian, "Some Design Considerations on the Electrostatically Actuated Fixed-Fixed End Type MEMS Switches," Journal of Physics: Conference Series **34**, 174-179 (2006).
34. CoventorWare™ v2006 Documentations: "MEMS Design and Analysis Tutorials, Volume 1: Physical and System-Level Design," (Coventor, Inc., 2006).
35. S. Tan *et al.*, "Electromechanical Modelling Of High Power RF-MEMS Switches With Ohmic Contact," 2005 European Microwave Conference.